THE UNIVERSITY OF CHICAGO

SEEKING SOLUTIONS FOR THE HUBBLE TENSION

A DISSERTATION SUBMITTED TO
THE FACULTY OF THE DIVISION OF THE PHYSICAL SCIENCES
IN CANDIDACY FOR THE DEGREE OF
DOCTOR OF PHILOSOPHY

DEPARTMENT OF ASTRONOMY AND ASTROPHYSICS

BY

MENG-XIANG LIN

CHICAGO, ILLINOIS

AUGUST 2022

Committee in charge

Professor Wayne Hu, Chair

Professor Nickolay Y. Gnedin

Professor Chihway Chang

Professor Thomas Crawford

To my parents

Dunye Lin and Huiqin Zeng.

CONTENTS

LIST OF FIGURES

LIST OF TABLES

ACKNOWLEDGMENTS

First and foremost I would like to thank my advisor Wayne Hu for his kind support and patience during my entire Ph.D., especially in the beginning of my cosmology journey. Discussing science with him is always a stimulating and inspiring activity thanks to his great insight. I enjoyed the days in front of the blackboard in his office. Wayne's philosophy that *"it is better to be correct than fast"* has shaped my academic standard.

I would also like to thank my collaborators, Marco Raveri, Giampaolo Benevento, Colin Hill, Evan McDonough, Shengjia Zhou, Jose Maria Ezquiaga, and Macarena Lagos, for their effort and thoughtful discussions. I am especially grateful for Marco Raveri, who guided me as I started my journey in cosmology research, taught me how to handle the code efficiently and shared with me his knowledge about CAMB.

I thank the thesis committee members, Nickolay Gnedin, Chihway Chang, and Tom Crawford for their support and feedback. Laticia Rebeles and Jennifer Smith ensured that I didn't miss any important deadlines. Valeri Galtsev provided his professional skill to support my computer. Thank you.

I thank Wayne's group meeting members during my Ph.D., Jose Maria Ezquiaga, Chen Heinrich, Keisuke Inomata, Austin Joyce, Macarena Lagos, Hayden Lee, Rayne Liu, Andrew Long, Pavel Motloch, Marco Raveri, Lian-tao Wayng, David Zegeye, Yiming Zhong, and especially Samuel Passaglia, for their patience with my weekly updates and under-prepared presentations and the useful feedback.

When I was an undergraduate, Renxin Xu and Bing Zhang led me to astrophysics research, and Subo Dong broadened my horizon. Without them I wouldn't even have the chance to start my Ph.D. study.

Faculty members in the Department of Astronomy and Astrophysics have created a supportive environment and I truly enjoyed my time here. I would especially like to thank Daniel Fabrycky and Rich Kron for their encouragement when I was in my low energy mode

and friendship.

My Office mates Ian Remming and Cameron Liang put up with my weird work schedule.

I also thank my other friends in Chicago and my fellow colleagues, Huanqing Chen, Siyao Jia, Andrew Neil, Zhijie Qu, Amy Tang, Ross Cawthon, Mandy Chen, Clarke Esmerian, Maya Fishbach, Taylor Hoyt, Gourav Khullar, James Lasker, Phil Mansfield, Rostom Mbarek, Jason Poh, Nora Shipp, Dimitrios Tangolidis, Fei Xu, Georgios Zacharegkas, and Zhuowen Zhang. They decorate my life with laughter and smiles.

I thank Hanjue Zhu for her companionship and her attempts to save me from procrastinating, although most of the times they didn't work – because everything has inertia and I am no exception.

Finally, I would like to thank my family, my parents Dunye Lin and Huiqin Zeng and my sister Yi Lin – the reason is not needed this time.

PREFACE

When I started my research in cosmology, the ΛCDM model was the standard paradigm of cosmology. Now as I am writing this thesis, despite it still being the only standard one, the ΛCDM model is challenged by the ever more precise modern observations. One of the most significant challenges is called the Hubble tension, the discrepancy between the locally measured Hubble constant H_0 and its value inferred from the early universe Cosmic Microwave Background (CMB) measurements assuming the ΛCDM model. During my Ph.D., Hubble tension increased from $\sim 3\sigma$ to $\sim 5\sigma$ thanks to the increasing measurement precision. The possible new physics behind this tension is attractive, making it one of the focuses of modern cosmology.

In this thesis I provide some thoughts and examples as the possible solutions for the Hubble tension based on my work with collaborators during my Ph.D. Unfortunately, so far we are still not sure if this tension is real or is due to systematic measurement errors, neither do we have the perfect physical solutions. I hope this work will at least provide some useful intuitions towards the true solutions for the Hubble tension if it is real.

Chapter 1 is provided as an overview of this thesis.

In Chapter 2 [3], I propose the Acoustic Dark Energy (ADE) model as a possible solution for the Hubble tension. As an extension to ΛCDM, ADE model introduces an additional simple scalar field whose energy density is only important near matter radiation equality. It can simultaneously reduce the Hubble tension and fit the CMB data better than ΛCDM. Planck 2015 CMB data are used in the analysis.

In Chapter 3 [4], I test the ADE model with the latest CMB data from Planck 2018 and the Atacama Cosmology Telescope. ADE passes the test to retain the ability to reduce the Hubble tension.

In Chapter 4 [5], I consider the interaction between Early Dark Energy and dark matter. It is naively expected that this interaction could suppress the matter density growth and

reduce the S_8 tension that is generically worsened in Early Dark Energy-like models including ADE. However, I find the dark energy - dark matter interaction induces a matter-philic fifth-force, hence limiting its ability to reduce the S_8 tension.

In Chapter 5 [6], I study the phenomenological imprints of modified gravity before recombination with a parameterized approach. I explore its impacts on various cosmological observables including the CMB, weak lensing and matter power spectrum. As an application, I found this early time modified gravity can also help to reduce the Hubble tension in the perturbation level.

I conclude and talk about possible future directions to solving the Hubble tension in Chapter 6.

Meng-Xiang Lin

Chicago, Illinois

July 2022

CHAPTER 1

INTRODUCTION

1.1 The Hubble Tension

As the standard paradigm of cosmology, the ΛCDM model has achieved a remarkable success in fitting different cosmological observations with only six free physical parameters. Despite its success, ΛCDM seems to fail in reconciling distance-redshift measurements when anchored at high redshift by CMB anisotropies to the same measurements anchored at low redshift by the local distance ladder. This discrepancy is commonly quantified as tension between the inferred value for the Hubble constant H_0, and its statistical significance has been steadily increased with the increasing experimental precision. The latest local measurements from SH0ES team places $H_0 = 73.30 \pm 1.04\ \mathrm{km\,s^{-1}\,Mpc^{-1}}$[7], showing a 5σ tension with the value inferred by the Planck 2018 CMB data assuming ΛCDM $H_0 = 67.4 \pm 0.5\ \mathrm{km\,s^{-1}\,Mpc^{-1}}$[8].

1.2 Why it is a hard problem?

The difficulty of solving Hubble tension mainly comes from the powerful constraints of modern cosmological observations, especially the precise CMB measurements. Here I briefly introduce some unsuccessful ideas in the literature to illustrate the physical reasons for this difficulty.

Based on when the new physics is introduced, we can divide the Hubble tension solutions into late time solutions and early time solutions. The late time solutions only change the expansion history after recombination while the early time solutions change the physics before recombination.

The late time solutions are usually introduced by changing the equation of state of dark energy, e.g., some dynamical dark energy models. Although it is easy to increase the H_0 value itself, it is generically very hard for the late time solutions to fit the whole Hubble flow

constructed from the local distance ladder, Baryon Acoustic Oscillations (BAO) and CMB measurements [9, 10].

As for early time solutions, a naive thought is to add more radiation-like energy components before recombination so that the sound horizon at recombination r_s is reduced. Given the precise measurements of CMB peaks that reflect angular size of the sound horizon, we will infer a higher H_0 solution from CMB. This kind of models is well studied in the literature. It is equivalent to changing the effective number of neutrino species $N_{\rm eff}$, and can be realized by various physical models such as sterile neutrinos. However, adding radiation-like components all the time will change the ratio of sound horizon to CMB damping scale, as the damping scale $\lambda_D \propto r_s^{1/2}$. Since CMB observations measure both sound horizon and damping scale precisely, this kind of models will fail to fit the CMB observational data. Hence, we need more complex new physics before recombination.

For more details, I would like to kindly refer the reader to reviews about the Hubble tension solutions [11, 12].

1.3 Early Dark Energy-like models

In 2019, Early Dark Energy (EDE) model was proposed [13] to solve the Hubble tension. In this model, EDE is a new component additional to ΛCDM that is only important near matter radiation equality, and redshifts away faster than radiation after the peak. The ratio of its energy density to the total is $\sim 10\%$ near the peak. As a result, it can reduce the sound horizon to infer a higher H_0 value, and keep the ratio of sound horizon to CMB damping scale unchanged so as to still fit CMB observational data well.

A class of Hubble tension solutions was proposed later sharing the same feature that contains a new energy component only important near matter radiation equality, including Acoustic Dark Energy model below, see 2. I call this class of models EDE-like models. Although EDE-like models can solve Hubble tension, they worsen another minor tension

within ΛCDM, the S_8 tension. S_8 tension quantified the discrepancy between the clustering amplitude S_8 inferred from CMB observation and its value measured from current Large Scale Structure surveys. Specifically, the latest Dark Energy Survey Year-3 results [14] indicate a 2.6σ tension with the Planck CMB prediction assuming ΛCDM. EDE-like models usually require a higher matter density to compensate the impact of the new radiation-like component to the amplitudes of CMB power spectra. As a consequence, they generically enhance the S_8 value which makes S_8 tension worse. In this sense, EDE-like models are not perfect solutions for Hubble tension, but they are the best we know so far.

1.3.1 Acoustic Dark Energy

Inspired by the EDE model, I proposed the Acoustic Dark Energy (ADE) model[3]. I point out that in order to realize the EDE-like feature with a scalar field, one needs to convert its potential energy to kinetic energy quickly enough near matter radiation equality. ADE realizes this in a simpler and more efficient way with a canonical scalar field. Besides indicating its ability to resolve Hubble tension with observational data (CMB data are from the Planck 2015 release), I also reveal the generic requirement between background and perturbation for fitting the data within EDE-like models. See more details in chapter 2.

I also test ADE with the latest Planck 2018 and Atacama Cosmology Telescope (ACT) CMB data[4]. I show that ADE passes new consistency tests in the CMB damping tail provided by the ACT data, and can still relieve the Hubble tension. Its ability to raise H_0 is now mainly constrained by the improved Planck acoustic polarization data, which also plays a crucial role in distinguishing ADE from other EDE-like models. Improved constrains on intermediate scale polarization approaching the cosmic variance limit in the future will be an incisive test of the acoustic dynamics of EDE-like models. See more details in chapter 3

1.3.2 Interaction of Early Dark Energy and Dark Matter

As predicted by the Swampland Distance Conjecture (SDC), it is natural for the dark matter mass to be exponentially coupled to the near-Planckian excursion of EDE field, $m \propto e^{-c|\Delta\phi|/M_{\rm Pl}}$ with the coupling constant $c \sim \mathcal{O}(1)$. One would naively expect that this interaction between EDE and dark matter might be able to suppress the matter density growth and hence resolve the S_8 tension within EDE-like models. Together with my collaborators, I introduce the Early Dark Sector (EDS) model to consider such an interaction[5]. I find that this interaction induces an EDE-mediated dark matter self-interaction which manifests as an enhanced gravitational constant on small scales. This dark matter-philic fifth-force enhances the dark matter density growth in the late universe, and hence limits the ability of the model to suppress S_8. I also provide the tightest observational constraints to date on a swampland parameter with the latest Planck and ACT data, suggesting that an EDE description of cosmological data is in tension with the SDC. See more details in chapter 4

1.4 Early Time Modified Gravity

Testing gravity theories on cosmological scales is always an interesting topic in modern physics. Most of the tests have targeted the late times during the epoch of cosmic acceleration. I explore modified gravity using a parameterized approach with a specific focus on the time of recombination and study its phenomenological impacts on the cosmological observables [6]. I find the early modified gravity provides another mechanism to relieve the Hubble tension in perturbation level, as it changes the physics of photon-baryon acoustic oscillations and hence opens new degrees of freedom to fit the CMB data. With a certain parameter choice, it can raise H_0 and decease S_8 at the same time which shows the potential to resolve the Hubble tension and S_8 tension simultaneously.

But notice that in this preliminary work I only study the perturbation effects of modified

gravity and leave the background unchanged to ΛCDM. As a consequence, the model considered in this work fails to reconcile BAO measurements. A more complete study of early modified gravity is left for the future. See more details in Chapter 5.

CHAPTER 2

ACOUSTIC DARK ENERGY: POTENTIAL CONVERSION OF THE HUBBLE TENSION

2.1 Introduction

The ΛCDM model of cosmology has been tested by an extensive number of independent probes, showing its general robustness and remarkable ability to explain a wide range of observational data with only six parameters. Despite its indubitable success, ΛCDM seems to fail in reconciling distance-redshift measurements when anchored at high redshift by cosmic microwave background (CMB) anisotropies to the same measurements anchored at low redshift by the local distance ladder.

This discrepancy is commonly quantified as tension between the inferences for the Hubble constant (H_0), and its statistical significance has been steadily increasing with increasing experimental precision. The most recent local estimate of the Hubble constant places its value at $H_0 = 74.03 \pm 1.42$ km s^{-1} Mpc^{-1} [15], showing a 4.4σ tension with the value inferred by the Planck 2018 CMB data, $H_0 = 67.4 \pm 0.5$ km s^{-1} Mpc^{-1}, assuming the ΛCDM model [8].

This tension is mainly a discrepancy between the anchors for the absolute distance scale rather than an indicator of missing physics between the anchors. Once anchored at one end, the same ladder of intermediate redshift measurements from baryon acoustic oscillations (BAOs) to supernovae Type IA (SN) predict the anchor at the other end, leaving little room for missing cosmological physics in between (for a recent assessment and discussion, see Refs. [16, 17] and references therein). On the high redshift side, the anchor is the CMB sound horizon r_s. Under ΛCDM, the shapes of the CMB acoustic peaks calibrate the sound speed and all of the energy densities of species relevant around recombination and thus determine the physical scale of r_s. Measurements of its angular scale in the CMB then

fix the remaining parameter, the cosmological constant or equivalently H_0. Even beyond ΛCDM, this measurement determines the distance to recombination and anchors the inverse distance ladder from which H_0 can again be inferred so that even the most general dark energy or modified gravity model can only moderately alter its value [18, 6, 9, 19].

Altering the high redshift anchor requires modifying cosmological physics at recombination. Adding extra energy density raises the expansion rate before recombination and lowers the sound horizon r_s. For example, an extra sterile neutrino or other dark radiation has long been considered as a possible solution [20, 21, 22, 23, 24, 25, 26, 27, 28, 29, 30, 31]. However such a component would also change the driving of the acoustic oscillations and damping scale [32], which is now disfavored by increasingly precise CMB data, leaving little ability to raise H_0 (see Refs. [33, 8] for recent assessments).

The problem with the damping scale arises because these additions affect the background expansion like radiation. As pointed out in Ref. [13], this problem can be avoided by making the dark component only important transiently near the epoch of recombination. Specifically, Ref. [13] introduces a component of so-called "early dark energy" (EDE) where a scalar field oscillates anharmonically around the minimum of a periodic potential and finds that the Hubble tension can be efficiently relieved. On the other hand, Ref. [34] finds that for a monomial EDE model, which coincides with the periodic potential [13] at the minimum, the Hubble tension is only partially relieved. Due to the behavior of its perturbations, these EDE scenarios change the amplitudes and phases of the CMB acoustic peaks in complex ways, leading to questions as to the robustness of this method for relieving the Hubble tension.

To build a more robust method to relieve the Hubble tension, we study the general phenomenology of perturbations in a dark fluid which similarly becomes transiently important, here around matter-radiation equality. Since its impact on the CMB comes through the gravitational effects of its own acoustic oscillations, we call this species acoustic dark energy (ADE) and in particular uncover the critical role its sound speed plays in relieving

the Hubble tension. We find that the sound speed must vary with the equation of state in the background in a manner consistent with the conversion of potential to kinetic energy for a minimally coupled scalar with a general kinetic term [35]. Unlike the oscillatory EDE models, once released from Hubble drag, the scalar remains kinetic energy dominated until it redshifts away. Indeed for a simple canonical kinetic term, this allows for $H_0 = 70.60 \pm 0.85$ with a better fit than ΛCDM even for the CMB alone and a better total χ^2 by 12.7 for 2 extra parameters. This method is also robust and can be exactly realized in a wide class of potentials. We provide both the required conditions on the potential and explicit examples.

This paper is organized as follows. In §2.2, we introduce the ADE fluid model, its parameters, and the data sets that we use in the analysis. In §2.3, we discuss the phenomenological impacts of ADE, especially its sound speed, on acoustic driving and CMB polarization. In §2.4, we show that ADE models that can relieve the Hubble tension correspond to scalars that convert potential to kinetic energy suddenly upon Hubble drag release and construct a canonical scalar model as proof of principle. In §2.5, we discuss the relation to the previous work and we conclude in §2.6.

2.2 Methodology

Acoustic dark energy is defined to be a perfect dark fluid and is specified by its background equation of state $w_{\rm ADE} = p_{\rm ADE}/\rho_{\rm ADE}$ and rest frame sound speed c_s^2 [36]. The latter is only equivalent to the adiabatic sound speed $\dot{p}_{\rm ADE}/\dot{\rho}_{\rm ADE}$ for a barotropic fluid so that in the general case the acoustic phenomenology of linear ADE sound waves, which we shall see is crucial for relieving the Hubble tension, is defined independently of the background.

In order to have a transiently important ADE contribution, we model the ADE equation of state as

$$1 + w_{\rm ADE}(a) = \frac{1 + w_{\rm f}}{[1 + (a_c/a)^{3(1+w_{\rm f})/p}]p} \,. \tag{2.1}$$

The ADE component therefore changes its equation of state around a scale factor $a = a_c$ from $w_{\rm ADE} = -1$ to $w_{\rm f}$. Additionally, p controls the rapidity of this transition, with small values corresponding to sharper transitions. Since this parameter does not qualitatively change our results, we use $p = 1/2$ unless otherwise specified. We shall see in §2.4 that this corresponds to a simple quadratic potential for scalar field ADE. This is a generalization of the background of the EDE model [13], discussed in §2.5, where $p = 1$ and the fluid description is approximate.

The ADE background energy density is fully specified once its normalization is fixed, since $w_{\rm ADE}$ determines its evolution. Defining the ADE fractional energy density contribution

$$f_{\rm ADE}(a) = \frac{\rho_{\rm ADE}(a)}{\rho_{\rm tot}(a)}\,, \tag{2.2}$$

we choose $f_c = f_{\rm ADE}(a_c)$ as the normalization parameter.

The behavior of ADE perturbations is determined by their rest frame sound speed $c_s^2(a, k)$ which is, for an effective fluid, a function of both time and scale [36]. In the context of a perfect fluid with a linear dispersion relation, it is scale independent. In particular this holds for K-essence scalar field models [35], when treated exactly instead of in a time-averaged approximation. We shall return to this point in §2.5.

The equations of motion for ADE acoustic oscillations depend only on the value of c_s^2, not its time derivative. Since the impact of ADE on cosmological observables is extremely localized in time due to the parametrization of $w_{\rm ADE}$, we fix c_s^2 to be a constant, effectively its value at a_c. In §2.4, we construct K-essence models where c_s^2 is strictly constant as a proof of principle, but our analysis holds more generally if we interpret the constant c_s^2 as matching a suitably averaged evolving one.

In our most general case, the ADE model is therefore characterized by four parameters $\{w_{\rm f}, a_c, f_c, c_s^2\}$ once p is fixed. When varying these parameters we impose flat, range bound priors: $-4.5 \leq \log_{10} a_c \leq -3.0$, $0 \leq f_c \leq 0.2$, $0 \leq w_{\rm f} \leq 3.6$ and $0 \leq c_s^2 \leq 1.5$. We shall later

see that the Hubble tension can be relieved by varying just two of these four parameters, fixing $c_s^2 = w_{\rm f} = 1$, corresponding to models where the ADE is a canonical scalar that converts its energy density from potential to kinetic around matter radiation equality (see §2.4.2). We refer to this particular ADE model as cADE.

The full cosmological model also includes the six ΛCDM parameters: the cold dark matter density is characterized by $\Omega_c h^2$, baryon density by $\Omega_b h^2$, the angular size of the sound horizon by θ_s, the optical depth to reionization by τ, and the initial curvature spectrum by its normalization at $k = 0.05$ (wavenumbers throughout are in units of Mpc^{-1}, which we drop when no confusion should arise), A_s and tilt n_s. These have the usual non-informative priors. We fix the sum of neutrino masses to the minimal value (e.g., Ref. [37]). We modify the CAMB [38] and CosmoMC [39] codes to include all the models that we discuss, following Ref. [36]. We sample the posterior parameter distribution until the Gelman-Rubin convergence statistic [40] satisfies $R - 1 < 0.02$ or better unless otherwise stated.

For the principal cosmological data sets, we use the publicly available Planck 2015 measurements of the CMB temperature and polarization power spectra at large and small angular scales and the CMB lensing potential power spectrum in the multipole range $40 \leq \ell \leq 400$ [41, 42, 43]. To expose the Hubble tension, we combine this with the latest measurement of the Hubble constant, $H_0 = 74.03 \pm 1.42$ (in units of $\mathrm{km\,s^{-1}\,Mpc^{-1}}$ here and throughout) [15]. To these data sets we add the Pantheon Supernovae sample [44] and BAO measurements from BOSS DR12 [45], SDSS Main Galaxy Sample [46], and 6dFGS [47]. These datasets prevent resolving the Hubble tension by modifying the dark sector only between recombination and the very low redshift universe [17].

Our baseline configuration thus contains: CMB temperature, polarization and lensing, BAO, SN and H_0 measurements. Unless otherwise specified all of our results will be for this combined data set. We include all the recommended parameters and priors describing systematic effects for these data sets.

As we shall see, the CMB polarization data provide an important limitation on the ability to raise H_0 and future polarization data can provide a definitive test of the ADE models that alleviate the Hubble tension. We therefore also consider the joint data set without CMB polarization data. We refer to this data set as -POL.

Model	ΛCDM	cADE	ADE
$100\theta_{\rm MC}$	1.04115 (1.04110±0.00028)	1.04062 (1.04064±0.00031)	1.04072 (1.04081±0.00035)
$\Omega_b h^2$	0.02246 (0.02241±0.00014)	0.02267 (0.02271±0.00022)	0.02270 (0.02263±0.00022)
$\Omega_c h^2$	0.1170 (0.1174±0.0009)	0.1268 (0.1268±0.0032)	0.1274 (0.1242±0.0032)
τ	0.082 (0.075±0.012)	0.064 (0.064±0.012)	0.064 (0.067±0.013)
$\log(10^{10}A_s)$	3.092 (3.079±0.022)	3.078 (3.078±0.023)	3.080 (3.081±0.023)
n_s	0.9726 (0.9701±0.0039)	0.9833 (0.9833±0.0065)	0.9873 (0.9832±0.0071)
f_c	-	0.082 (0.082±0.025)	0.086 (0.079±0.033)
$\log_{10}a_c$	-	-3.45 (-3.46±0.06)	-3.52 (-3.50±0.15)
$w_{\rm f}$	-	1 (fixed)	0.87 (1.89±0.86)
c_s^2	-	1 (fixed)	0.86 (1.07±0.25)
H_0	68.58 (68.35±0.42)	70.57 (70.60±0.85)	70.81 (70.20±0.88)
$\Delta\chi^2_{\rm tot}$	0	-12.7	-14.1

Table 2.1: Maximum likelihood (ML) parameters and constraints for the ΛCDM model, the canonical Acoustic Dark Energy (cADE) model, and the general ADE model. $\Delta\chi^2_{\rm tot} = -2\Delta\log\mathcal{L}$ reflects the ratio between the maximum likelihood value and that of ΛCDM for the joint data.

2.3 ADE Phenomenology

In this section we discuss the phenomenology and observational implications of ADE and their dependence on its parameters.

At the background level, the addition of ADE increases the total energy density before recombination that changes the expansion history lowering the sound horizon r_s. This changes the calibration of distance measures not only for the CMB but also the whole inverse distance ladder through BAO to SN. Given the precise angular measurements of the sound horizon θ_s, the inverse distance ladder scale is reduced and hence the inferred H_0 rises.

The prototypical example of this method for relieving the Hubble tension is an extra sterile neutrino that is at least mildly relativistic at recombination. Neutrinos, however, do

not provide a good global solution (e.g., Ref. [33]) since they behave as free-streaming radiation before recombination and therefore change the phase of the CMB acoustic oscillations as well as the CMB damping scale, the distance a photon random walks through the ionized plasma before recombination, approximately as $\lambda_D \propto r_s^{1/2}$ [32]. A more general dark fluid, on the other hand, can reduce the fraction of the dark component vs. normal radiation before matter radiation equality, allowing the two scales to change in a proportional way [13].

Beyond these background effects, ADE and other dark sector candidates for relieving the Hubble tension, gravitationally drive photon-baryon acoustic oscillations changing the amplitudes and phases of the CMB peaks (e.g., Ref. [33, 6]). ADE perturbations undergo their own acoustic oscillations under its sound horizon, leading to novel CMB driving phenomenology. As detailed in Table 2.1, this modified phenomenology leads to a maximum likelihood (ML) solution with $w_{\rm f} \approx c_s^2$ and $H_0 = 70.81$ which improves $\Delta\chi^2_{\rm tot} = -14.1$ over ML ΛCDM, and more generally a finite ADE fraction f_c is detected at 2.4σ. In the next section, we focus on the details of these physical effects. We then address the impact of Planck polarization data and the ability of future polarization data to test the ADE solutions to the Hubble tension.

Finally, note that although we do not consider measurements of the amplitude of local structure here, the ML and constraints for ADE are $\sigma_8\Omega_m^{1/2}$=0.4623 (0.4573±0.0073), whereas for ΛCDM with CMB TT only has nearly the same ML but larger errors 0.466 (0.466±0.013). For our combined data set, ΛCDM gives the value 0.4488 (0.4486±0.0056), where the ML is lower since raising H_0 in ΛCDM lowers $\sigma_8\Omega_m^{1/2}$ unlike in ADE. If the tension with weak lensing measurements of the amplitude increases in ΛCDM in the future, it will disfavor not only ΛCDM but these ADE models as well.

2.3.1 *Acoustic Driving*

Under the sound horizon or Jeans scale of the ADE, its density perturbations acoustically oscillate rather than grow, leading to changes in the decay of the Weyl potential $(\Psi + \Phi)/2$. This decay drives CMB acoustic oscillations, and the ADE impact is especially important for modes that enter the CMB sound horizon near a_c, roughly $k = 0.04$ in the ML ADE model from Table 2.1. The excess decay is countered by raising the cold dark matter through $\Omega_c h^2$ since it remains gravitationally unstable on the relevant scales.

For ADE, at the parameter level, this effect is controlled by the sound speed c_s in conjunction with the equation of state $w_{\rm ADE}(a)$ through $w_{\rm f}$. These two parameters are hence strongly correlated, as shown in Fig. 2.1, reflecting degenerate effects on the CMB when they are raised or lowered together. Near the ML solution, this requires $w_{\rm f} \approx c_s^2$.

We explore this degeneracy in Fig. 2.2 by showing the evolution of the Weyl potential for this mode in the ML model (red) from Table 2.1 relative to the same model with no ADE (ML, $f_c = 0$) as a baseline (black). The Weyl potential is relatively suppressed at $a < a_c$, enhanced at $a \sim a_c$ and suppressed again at $a \gg a_c$ due to ADE. The enhancement and subsequent suppression correspond to the first acoustic compression extremum in the ADE density perturbation and the subsequent Jeans stabilization of the perturbations. The net impact is a reduction in the Weyl potential. This reduction is compensated by raising $\Omega_c h^2$. For comparison we also show the difference in reverting the value of $\Omega_c h^2$ in the baseline model to the ML ΛCDM value (cyan dashed). Since $a_c \sim a_{\rm eq}$, ADE becomes important around the same epoch when radiation driving has the maximal impact on the shape of the CMB acoustic peaks. Along with other adjustments in ΛCDM parameters, in particular n_s and $\Omega_b h^2$, these effects compensate for each other.

This compensation leaves the CMB acoustic peaks nearly unchanged despite raising H_0 from 68.58 to 70.81. In Fig. 2.3, we show the data and model residuals relative to the ΛCDM ML in Table 2.1. As we can see, this effect does not exacerbate the oscillatory residuals in

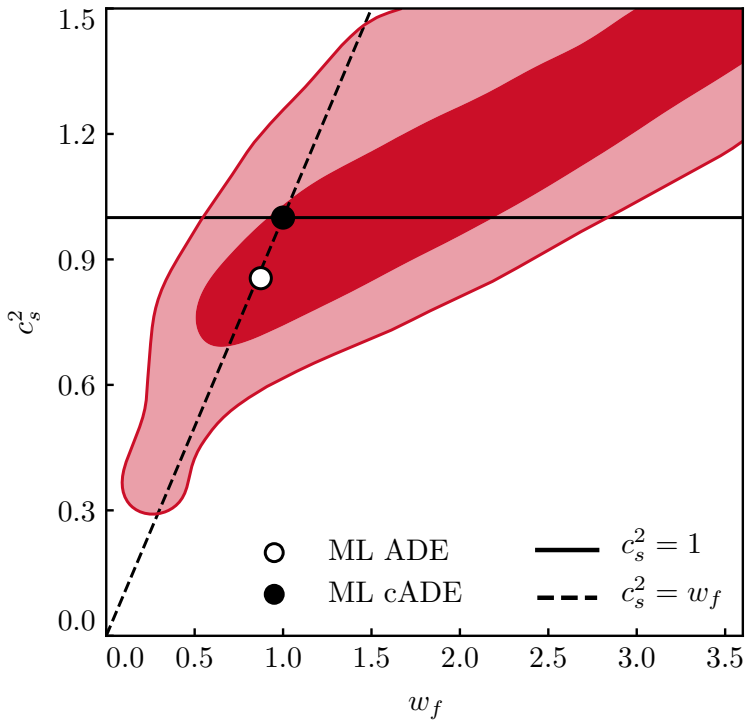

Figure 2.1: The joint marginalized distribution of the ADE parameters c_s^2 and $w_{\rm f}$, obtained using our combined datasets. The darker and lighter shades correspond respectively to the 68% C.L. and the 95% C.L. The markers indicate the maximum likelihood values for ADE (solid circle) from Tab. 2.1 and the intersection between canonical models $c_s^2 = 1$ (solid line) and models which convert potential to kinetic energy at the transition $c_s^2 = w_{\rm f}$ (dashed line), i.e. $c_s^2 = w_{\rm f} = 1$ (open circle) as in cADE.

the data, where the acoustic peaks (vertical lines) are suppressed relative to troughs, which would occur if H_0 were raised in ΛCDM. Note that the residuals are scaled to the cosmic variance per ℓ-mode for the ML ΛCDM model as:

$$\sigma_{\rm CV} = \begin{cases} \sqrt{\frac{2}{2\ell+1}} C_\ell^{TT}, & TT\,; \\ \sqrt{\frac{1}{2\ell+1}} \sqrt{C_\ell^{TT} C_\ell^{EE} + (C_\ell^{TE})^2}, & TE\,; \\ \sqrt{\frac{2}{2\ell+1}} C_\ell^{EE}, & EE\,. \end{cases} \tag{2.3}$$

We can better understand the origin of the ADE effects and their impact on the CMB by varying $w_{\rm f}$ and c_s^2 independently. Fig 2.2 (upper) also shows a +0.4 variation in each

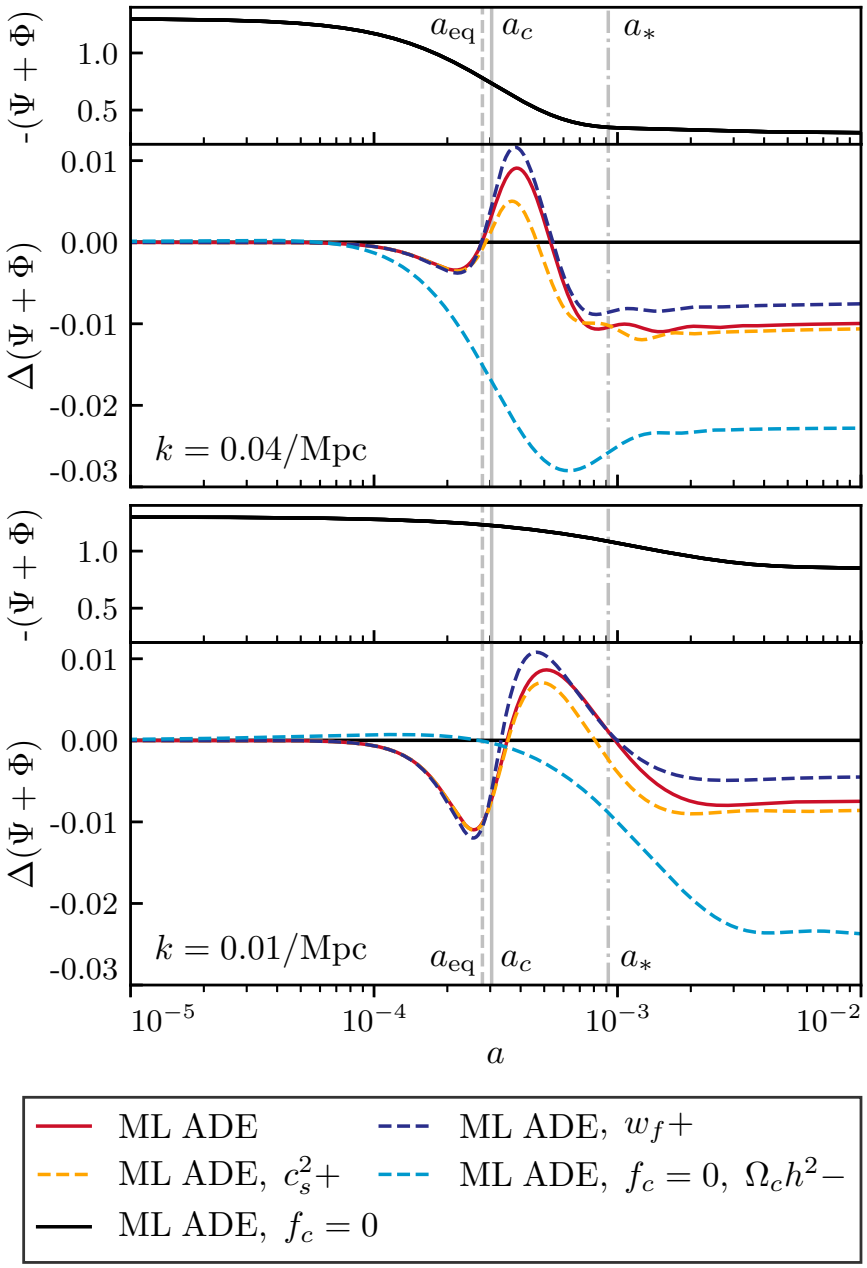

Figure 2.2: The Weyl potential evolution of the ML ADE model from Table 2.1 for two modes: $k = 0.01$ and 0.04 Mpc^{-1}. Lower subpanels show differences with respect to the baseline value of Weyl potential for the ΛCDM parameters of ML ADE but with no ADE ($f_c = 0$), as displayed in the upper subpanels. Shown are ML ADE (red solid) and parameter variations around it: c_s^2+ (orange dashed) and w_f+ (dark blue dashed) mean +0.4 variations, while $\Omega_c h^2-$ (cyan dashed) means lowering it to the ML ΛCDM value in Table 2.1. Relevant temporal scales (matter-radiation equality $a_{\rm eq}$, ADE transition a_c and recombination a_*) are shown with vertical lines.

with other parameters held fixed. Increasing c_s^2 makes the ADE acoustic oscillations and Jeans stability occur earlier and as a consequence also cuts into the enhancement. Raising $w_{\rm f}$ has two effects. Before the first compression peak and above the CMB sound horizon, the comoving ADE density perturbation grows adiabatically so that its amplitude grows relative to the photons approximately as $\delta_{\rm ADE} \propto (1+w_{\rm ADE})\delta_\gamma$. For $w_{\rm f} > 1/3$ this first causes a dip at $a \lesssim a_c$ and then an enhancement in the Weyl potential for $a \gtrsim a_c$, especially approaching the first compression. A larger $w_{\rm f}$ then suppresses $f(a > a_c)$ which also causes a relative enhancement at $a > a_c$. Combined, these effects imply that for a fixed amount of driving of acoustic oscillations through the decay of the Weyl potential, raising c_s^2 should be compensated by raising $w_{\rm f}$. This is the leading order degeneracy that we see in Fig. 2.1.

In terms of the residuals, shown in Fig. 2.3, a positive variation in c_s^2, when *not* compensated by $w_{\rm f}$, leads to a sharp TT feature around $\ell \sim 500$ near the second TT peak whereas along the degeneracy line the ML model TT residuals remain small. The modes responsible for higher multipoles are not sensitive to ADE perturbation parameters since the Weyl decay that drives them occurred before the ADE became important $a \ll a_c$.

The degeneracy is truncated at low $w_{\rm f}$ in Fig. 2.1. If $w_{\rm f} < 1/3$, the ADE redshifts slower than the radiation and thus has a large impact on the driving of CMB acoustic oscillations between a_c and recombination which cannot be balanced by the same variations in c_s^2.

2.3.2 CMB Polarization

Even for the ML ADE model, the compensation between $\Omega_c h^2, c_s^2$, and $w_{\rm f}$ is imperfect for modes that enter the CMB sound horizon between a_c and recombination. These modifications leave distinct imprints on the polarization spectra that already limit the ability of ADE to raise H_0 using the Planck data and, in the future, can definitively test this scenario. Polarization provides the cleanest signatures of driving on these scales given that it isolates the acoustic oscillations at recombination from the early integrated Sachs-Wolfe that smooths

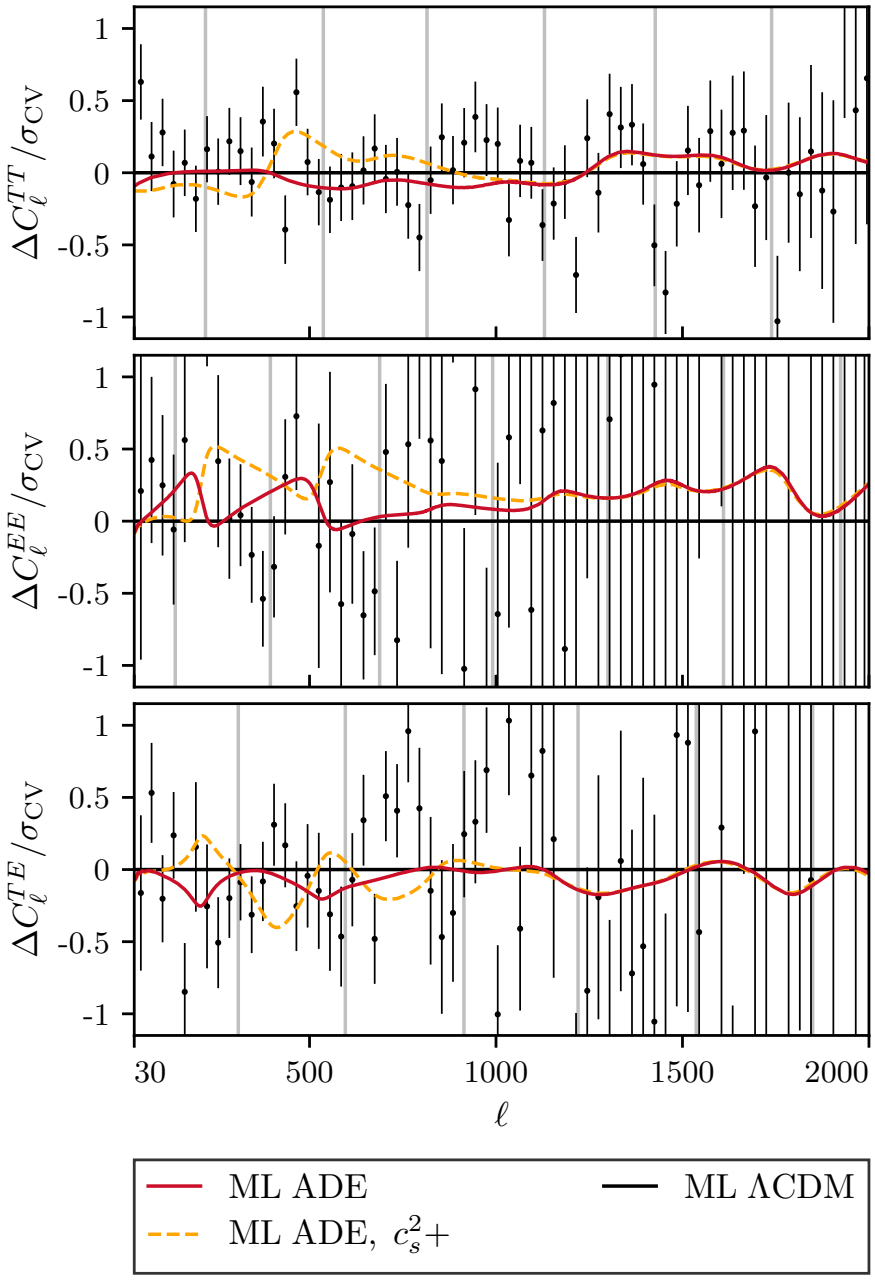

Figure 2.3: The CMB model and Planck data residuals with respect to the ML ΛCDM model. Shown are the ML ADE model (red solid) and a $\Delta c_s^2 = +0.4$ variation on it (orange dashed, see Fig. 2.2). The upper, middle, and bottom panels correspond to TT, EE, and TE residuals respectively and vertical lines denote their peaks in the ML ΛCDM model.

out its signatures in the TT spectrum.

In Fig. 2.2 (lower), we show the Weyl potential evolution for such a mode, $k = 0.01$ in

the ML model. While the qualitative behavior is similar to the higher k mode, the balance between $w_{\rm f}$, c_s^2 and $\Omega_c h^2$ changes. First, the impact of the change in $\Omega_c h^2$ is relatively higher since the ADE redshifts faster than radiation. Second, the impact of $w_{\rm f}$ is also somewhat higher relative to c_s^2. These changes lead to uncompensated sharp features in the polarization residuals.

For the Planck data, where measurements of the EE spectrum are still noisy, this makes the TE spectrum the most informative for these features (see Fig. 2.3). In the ΛCDM model, this sensitivity provides an important constraint on $\Omega_c h^2$ and hence supporting evidence for a low H_0 from multipoles $\ell < 1000$. The region around $\ell \sim 165$ (between the first EE and TT peaks) is particularly important due to the 2σ low point compared to the best fit ΛCDM model shown in Fig. 2.3 [48]. Note that in ΛCDM raising H_0 requires lowering $\Omega_c h^2$ which raises TE there, making the fit even worse.

In the ADE ML model, the impact of raising $\Omega_c h^2$ lowers TE in this region providing a better fit to the data. Even without direct H_0 data, the CMB data favor the ADE model (see Table 2.2). However raising H_0 further than the ADE ML would make TE too low at $\ell \lesssim 500$ for the data. Indeed for the -POL dataset, the ML model allows for a larger Hubble constant $H_0 = 72.27$ compared with 70.81 for our joint dataset.

Raising c_s^2 has the impact of making the ADE more important for Weyl decay and counters the effect of raising $\Omega_c h^2$. As we can see from Fig. 2.3, this has the effect of raising TE in this region and degrading the fit. Thus the TE data are also important for disfavoring a canonical scalar field with $c_s^2 = 1$ if $w_{\rm f}$ is too low. We shall see in §2.5 that this explains why previously considered models where a canonical scalar field oscillates in its potential must have its initial conditions set to avoid this region.

Finally, given the sharp features in the EE model residuals with up to $\sim 0.3 - 0.4$ amplitudes relative to cosmic variance *per multipole*, all of these cases where H_0 is raised by dark components that also change the driving of the acoustic peaks can be tested to high

significance once EE measurements approach the precision of TT measurements today.

2.4 Potential-Kinetic Conversion

The ADE phenomenology favored by the Hubble tension can be concretely and exactly realized in the K-essence class of dark energy models, where the dark component is a perfect fluid represented by a minimally coupled scalar field ϕ with a general kinetic term [35]. More specifically, the class of constant sound speed c_s models introduced in §2.2 is given by the Lagrangian density [49]

$$P(X,\phi) = \left(\frac{X}{A}\right)^{\frac{1-c_s^2}{2c_s^2}} X - V(\phi), \tag{2.4}$$

where the kinetic term involves $X = -\nabla^\mu\phi\nabla_\mu\phi/2$ and A is a constant density scale. For a scalar with a canonical kinetic term $c_s^2 = 1$, and more generally $w_{\rm ADE} \to c_s^2$ if the kinetic term dominates, whereas $w_{\rm ADE} \to -1$ if the potential $V(\phi)$ dominates. The fluid correspondence holds when $\nabla^\mu\phi$ remains always timelike; then $c_s^2 = \delta p/\delta\rho$ in constant field gauge or rest frame, where the momentum density of the field vanishes and the potential energy is spatially constant.

The correlation shown in Fig. 2.1 implies that around the ML ADE model from Table 2.1, setting $w_{\rm f} = c_s^2$ provides a good fit to the combined data. Since $w_{\rm ADE} \to -1$ for $a \ll a_c$ and $w_{\rm ADE} \to w_{\rm f}$ for $a \gg a_c$, this suggests that the best fitting $P(X,\phi)$ models are those that suddenly convert nearly all of their energy density from potential to kinetic at a_c. If we focus on a model that has such a potential to kinetic energy conversion feature, we have $c_s^2 = w_{\rm f}$ and the number of parameters of ADE reduces to three. The ML of this model gives $c_s^2 = 0.84$, $H_0 = 70.84$ and $\Delta\chi^2_{\rm tot} = -14.1$ which is nearly identical to ML ADE with one fewer free parameter.

Indeed the preferred region includes $w_{\rm f} = c_s^2 = 1$ which corresponds to the case of a canonical field, cADE. From Table 2.1, we see that the ML cADE model has only a

marginally smaller $H_0 = 70.57$ for a $\Delta\chi^2_{\rm tot} = -12.7$ and more generally a higher significance to the detection of a finite ADE fraction f_c of 3.3σ given the smaller set of parameters. We shall now consider how to construct a corresponding potential $V(\phi)$.

2.4.1 Canonical Conditions

A canonical scalar which converts its potential to kinetic energy around a_c provides a simple, concrete example of ADE that alleviates the Hubble tension. To explicitly construct such a model that matches requirements on the two remaining quantities a_c and f_c we can determine the equivalent requirements for the potential $V(\phi)$.

At $a \ll a_c$, the ϕ field is stuck on its potential due to Hubble friction and rolls according to

$$\frac{d\phi}{dN} \sim -\frac{V'}{H^2}, \tag{2.5}$$

where $N = \log a$ denotes e-folds. For the purposes of this qualitative discussion we drop factors of order unity. After a_c, we want the field to be released from Hubble drag and convert its potential energy to kinetic energy on the e-fold timescale $\Delta N \sim 1$. Defining $\phi_c = \phi(a_c)$ and linearizing the change

$$V(\phi) \approx V(\phi_c) + V'(\phi_c)\Delta\phi. \tag{2.6}$$

Therefore, around ϕ_c, we want

$$\left(\frac{V'}{H}\right)^2 \gtrsim V, \tag{2.7}$$

or in terms of $f_c \sim V/\rho_{\rm tot}$,

$$\epsilon_V f_c \gtrsim 1, \qquad \epsilon_V \equiv \frac{M_{\rm Pl}^2}{2}\left(\frac{V'}{V}\right)^2. \tag{2.8}$$

This is the main condition for the potential to kinetic conversion.

For the linearization in Eq. (2.6) to be valid in the sense of the second order term $\frac{1}{2}(\Delta\phi)^2V''$ not preventing the conversion, we also want

$$V''(\phi_c) < -\frac{V'(\phi_c)}{\Delta\phi} \tag{2.9}$$

so

$$V'' \lesssim H^2. \tag{2.10}$$

Putting these two criteria together,

$$\eta_V \lesssim 2\epsilon_V, \qquad \eta_V \equiv M_{\rm pl}^2\frac{V''}{V}, \tag{2.11}$$

where we have restored a factor of 2 so as to match the well-known condition for no tracking solution to exist [50]. Tracking potentials do not work since the scalar field follows an equation of state that is determined by the dominant component of the total energy density rather than the kinetic energy dominated limit. A similar derivation applies to the $c_s^2 \neq 1$ case with a modification to the Hubble drag evolution (2.5) [49].

Finally we want the field to maintain kinetic energy domination until its energy density has largely redshifted away. This excludes models where the field oscillates around a minimum and so is different from those in Refs. [13, 34] as we shall discuss in the next section. Furthermore, the fluid description is exact for our models whereas it is only approximate for oscillatory models.

Thus our requirements on the potential are fairly generic and correspond to setting the amplitude and slope of the potential at the desired point of Hubble drag release, along with the condition that the field remains kinetic energy dominated until most of the energy density has redshifted away. A wide class of potentials can satisfy these requirements and we shall give concrete examples next.

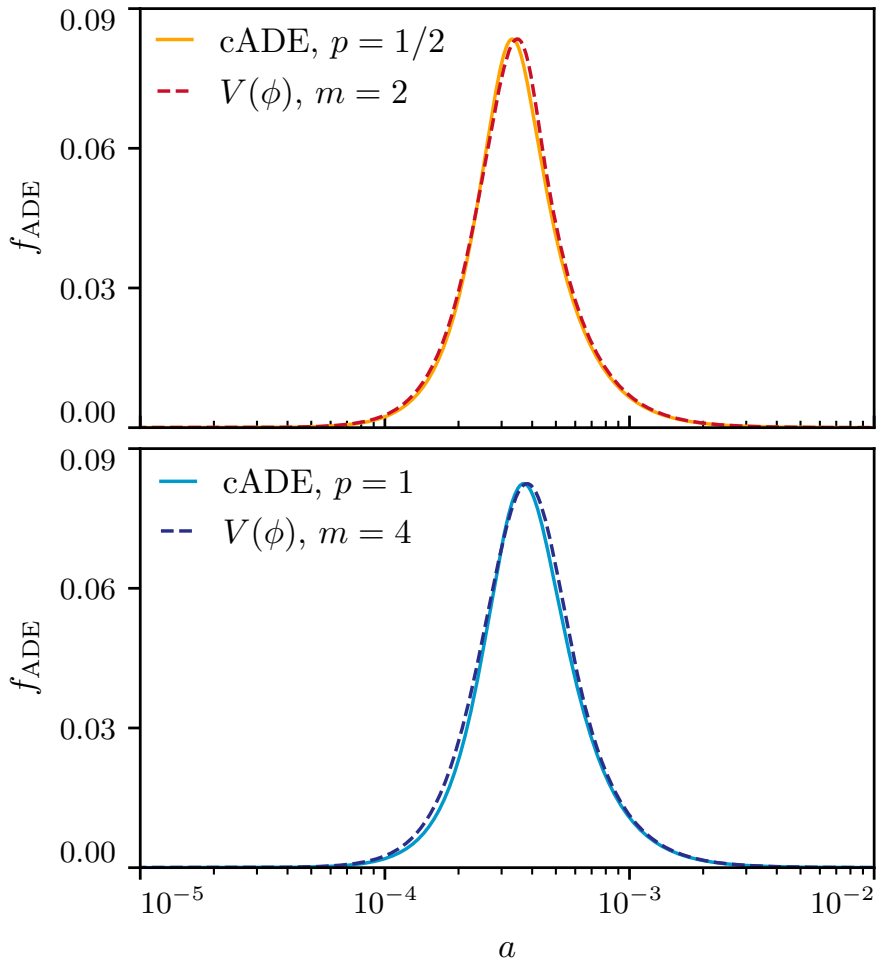

Figure 2.4: Scalar field potential $V(\phi)$ match to the fractional ADE energy density $f_{\rm ADE}$ of the ML cADE parameters in Table 2.1. Top: a locally quadratic potential with Eq. (2.12) compared with $p = 1/2$ in Eq. (3.1); bottom: a locally quartic potential vs $p = 1$.

2.4.2 Canonical Solution

To make these considerations concrete, consider the class of potentials:

$$V(\phi) = \begin{cases} A\,\phi^m, & \phi > 0\,, \\ 0, & \phi \leq 0\,. \end{cases} \tag{2.12}$$

Then for $\phi > 0$

$$2\epsilon_V = \left(\frac{m}{\phi}\right)^2, \qquad \eta_V = \frac{m(m-1)}{\phi^2}\,, \tag{2.13}$$

and any $m > 0$ satisfies $\eta_V < 2\epsilon_V$. The flat potential at $\phi \leq 0$ prevents the kinetic energy from converting back to potential energy. We choose A and $\phi_{\rm initial}$ to give the desired f_c and a_c.

In Fig. 2.4 (upper), we show a worked example of this matching. We fix cosmological parameters to the ML ADE model in Table 2.1 and take a quadratic potential with $m = 2$. We find a good match to the form of Eq. (3.1) with $p = 1/2$. This motivates our fixed fiducial choice in §2.2.

To showcase the robustness of the potential to kinetic conversion mechanism for relieving the Hubble tension, we also consider a quartic potential $m = 4$ (Fig. 2.4, lower). The change in $f_{\rm ADE}(a)$ is itself small and, once a shift in a_c is absorbed, corresponds to a slight broadening of the transition. Even this small change can be matched to the general ADE form of Eq. (3.1) by adopting $p = 1$. For the linear $m = 1$ case, $p \approx 0.1$ corresponding to a sharper transition. We have also tested that various values of p in this range provide comparable ML solutions to our fiducial $p = 1/2$ case. Finally we have tested that the correspondence between p and m holds for non-canonical values of c_s^2 with the Lagrangian (2.4).

These simple canonical or cADE models still provide good fits to the data as illustrated in Fig. 2.5 for the ML cADE model of Table 2.1. The main difference compared with ML ADE is

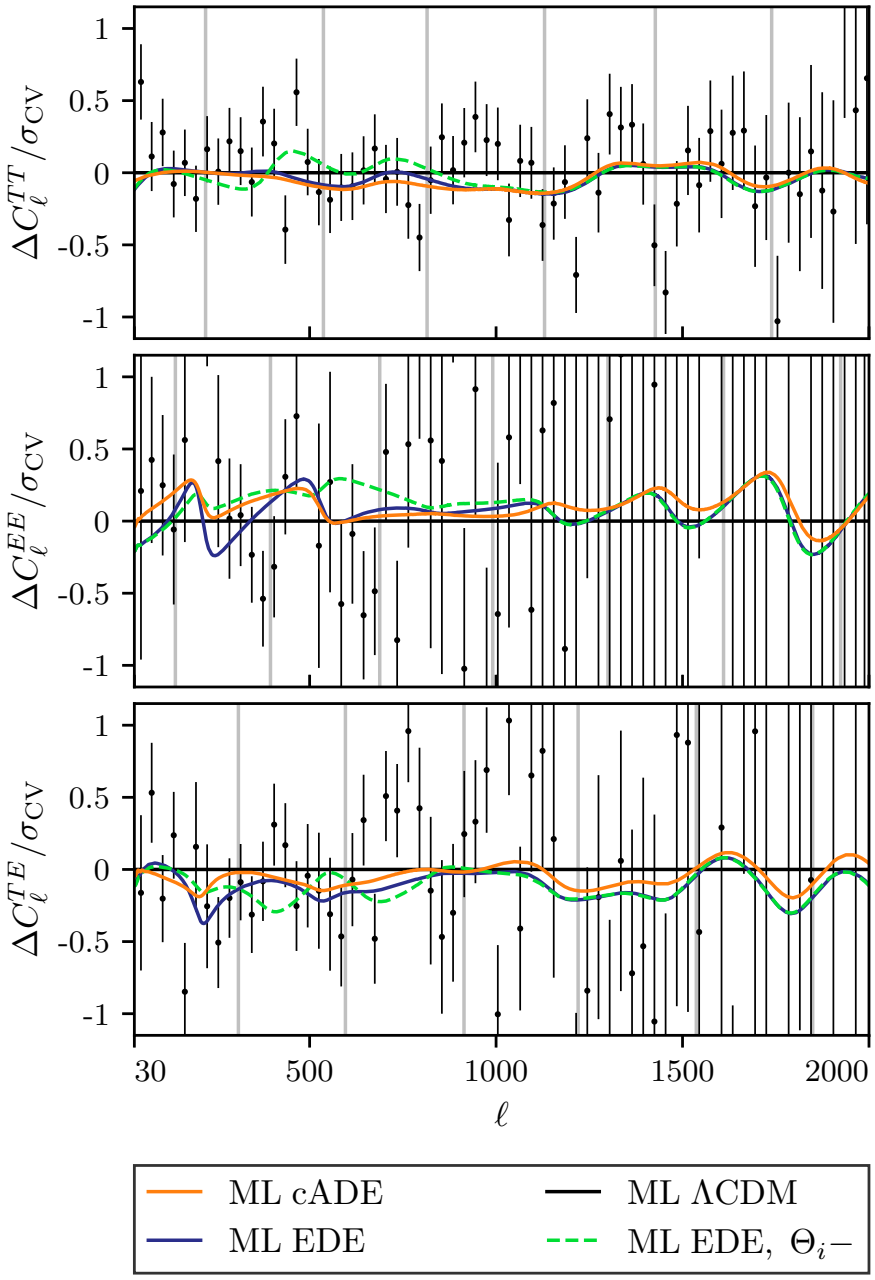

Figure 2.5: Canonical scalar field model and data residuals of ML cADE (orange solid) and ML EDE (dark blue solid) models with respect to the ML ΛCDM model as in Fig. 2.3. The model with $\Delta\Theta_i = -0.5$ from ML EDE (green dashed) is also shown.

the slight lowering of H_0 from 70.81 to 70.57. The total improvement over ΛCDM for 2 extra parameters is $\Delta\chi^2_{\rm tot} = -12.7$ with -3.6 actually coming from the improved fit to the CMB as shown in Table 2.2. More concretely, ML cADE makes CMB lensing a little bit worse by

$\Delta\chi^2_{\rm lens} = +1.1$ but fits the TT and polarization spectrum better by $\Delta(\chi^2_{\rm plik} + \chi^2_{\rm lowTEB}) = -4.7$. If compared to ML ΛCDM fit to CMB only, the ML cADE fits CMB lensing as well and fits the TT and polarization spectrum better by $\Delta(\chi^2_{\rm plik} + \chi^2_{\rm lowTEB}) = -1.6$. [1]

Fig. 2.6 shows the parameter covariances and posteriors in the cADE model. The centered values for the ML parameters is indicative of the nearly Gaussian posteriors and reflects the fact that the parameters are constrained mainly by the data rather than the priors. The one exception is a_c since if $a_c \to 0$ any f_c is equivalent to ΛCDM so that the prior volume begins to matter. Even in this case, ΛCDM is sufficiently disfavored so that constraints on a_c are data not prior driven. Correspondingly the ADE fraction is significantly detected with $f_c = 0.082 \pm 0.025$.

This model also illustrates the main compensation between raising the ADE fraction f_c and raising the CDM density $\Omega_c h^2$ as well as adjusting $\Omega_b h^2$ and n_s slightly higher to minimize the data residuals (see Fig. 2.6). The change in θ_* to lower values is also notable. The modifications in driving make a small change in the phasing of the CMB acoustic peaks relative to its sound horizon. Note that in ΛCDM, θ_* drifts lower once the high multipoles $\ell > 800$ are included [51].

Finally under the -POL data set, the ADE canonical model allows a higher $H_0 = 71.55 \pm 1.05$ and ML value of 71.93. This is because of the limitations the TE spectrum around $\ell \lesssim 500$ places on these solutions as discussed in §2.3.2.

1. We have also explicitly checked that a direct solution for the scalar field Klein Gordon equation is nearly indistinguishable from a cADE model with the best matching parameters, e.g. $\Delta\chi^2 = 1.4$ for a cosmic variance limited TT, TE, EE measurement to $\ell \leq 2000$. This holds for these gravitationally sourced, or adiabatic, field perturbations whereas modeling isocurvature fluctuations from initial field perturbations from inflation would require matching the radiation dominated evolution in the equation of state $(1 + w) \propto a^4$ implied by Hubble friction through Eq. (2.5) [49], which Eq. (3.1) does not do.

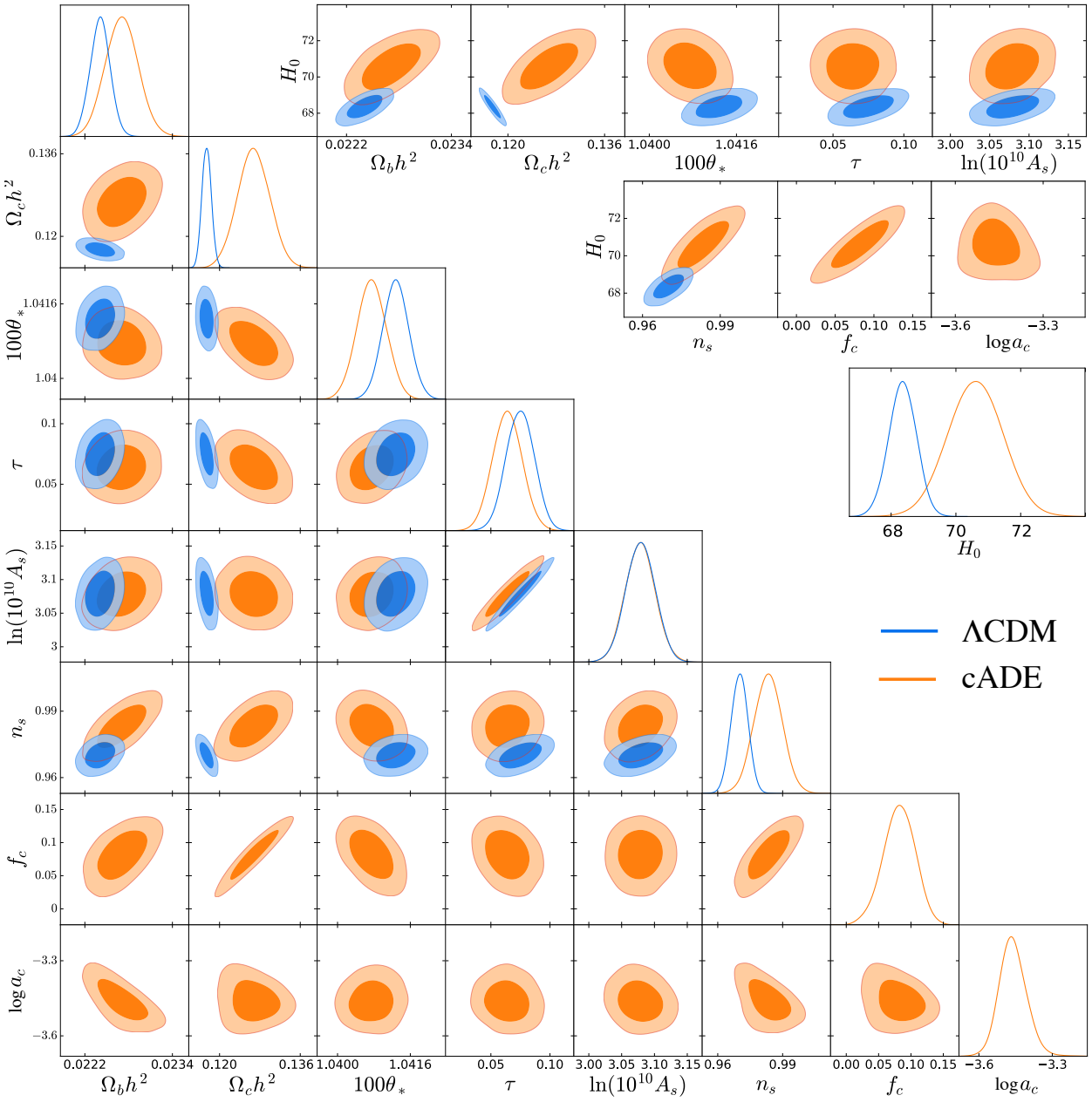

Figure 2.6: The marginalized joint posterior of the parameters of the cADE model, obtained using our combined datasets. ΛCDM results are also added for comparison. The 8 fundamental parameters are shown in the lower triangle whereas the implications for H_0 are shown in the upper triangle. The darker and lighter shades correspond respectively to the 68% C.L. and the 95% C.L.

2.5 Relation to Prior Work

In Ref. [13], a canonical scalar field component, referred to as early dark energy, with a potential

$$V(\phi) \propto [1 - \cos(\phi/f)]^n, \tag{2.14}$$

plays a similar role as our ADE. Unlike ADE, EDE oscillates after being released from Hubble drag and Ref. [1] finds that the time averaged background equation of state can be modeled by Eq. (3.1) with $p = 1$ and

$$w_{\rm f} = \frac{n-1}{n+1}\,. \tag{2.15}$$

As we have discussed in the previous sections, $w_{\rm f}$ is a relevant parameter for the resolution of Hubble tension, so its adjustment should be considered a parameter variation in the EDE model in spite of n taking discrete integer values.

The time-averaged behavior of perturbations is described by a fluid approximation with a rest frame sound speed [1]:

$$c_s^2(a,k) = \begin{cases} 1, & a \le a_c, \\ \dfrac{2a^2(n-1)\varpi^2 + k^2}{2a^2(n+1)\varpi^2 + k^2}\,, & a > a_c\,. \end{cases} \tag{2.16}$$

Unlike in our case, this fluid description is approximate, especially at a_c. The time dependence of ϖ is fixed by the parameters $a_c, w_{\rm f}$ and the initial field position $\Theta_i = \phi_i/f$ [1]:

$$\varpi(a) = \frac{\mathcal{G}}{\mathcal{P}}\sqrt{\frac{6\mathcal{P}+2}{8n}\frac{\Theta_i}{\sin\Theta_i}}H(a_c)a^{-3w_{\rm f}}\,. \tag{2.17}$$

Here $\mathcal{P} = H(a_c)t$ and we approximate it as:

$$\mathcal{P}(x = a_c/a_{\rm eq}) = \frac{2}{3}\frac{x^2 - x + 2\sqrt{1+x} - 2}{x^2}\,, \tag{2.18}$$

while

$$\mathcal{G}(a_c, n) = \frac{\sqrt{\pi}\Gamma(\frac{n+1}{2n})}{\Gamma(1+\frac{1}{2n})} 2^{-\frac{n^2+1}{2n}} 3^{\frac{1}{2}(\frac{1}{n}-1)} a_c^{3-\frac{6}{n+1}} \times \left[a_c^{\frac{6n}{n+1}} + 1\right]^{\frac{1}{2}(\frac{1}{n}-1)} . \quad (2.19)$$

Note that for $w_{\rm f} > 0$, ϖ decreases with a, and so the sound speed evolves from 1 at $a \leq a_c$ back to 1 at late times, with higher k exhibiting smaller amplitude deviations, and a k-dependent minimum $c_s^2(a_c, k)$.

The EDE model therefore has four parameters a_c, f_c, Θ_i and n. Following Ref. [1], we choose the best value $n = 3$, which corresponds to $w_{\rm f} = 1/2$, and conduct an MCMC likelihood analysis on the remaining parameters. We treat a_c and f_c as in the ADE model and impose a flat prior on $0 \leq \Theta_i/\pi \leq 1$. Because of the large parameter volume of degenerate models around ΛCDM, we only sample the posterior until $R - 1 < 0.05$ which should give an adequate, but not perfect, estimate of parameter constraints out to 95% C.L. The results are compared with our ADE model in Table 2.2. The EDE ML model allows a slightly higher $H_0 = 71.92$ and hence a better fit to the data $\Delta\chi^2_{\rm tot} = -2.5$ for one extra parameter over ML ADE with $c_s^2 = w_{\rm f}$ or $\Delta\chi^2_{\rm tot} = -3.9$ for two extra parameters compared with the cADE ML. Note that with the -POL dataset, the EDE and ADE models have comparable performances.

The main phenomenological difference between the ADE and EDE models is the parametrization of the sound speed. The sound speed was indeed also varied in Ref. [1] but its impact was not discussed. As we have seen in our ADE model a low $w_{\rm f}$ generally requires a low c_s^2. In the EDE model, this translates into specific requirements for the initial phase Θ_i. In Fig. 2.7, we show the relationship between constraints on Θ_i, H_0 and the minimum sound speed at $k = 0.01, 0.04$. As we can see, achieving a higher value of H_0 requires a large initial phase and its ML value is $\Theta_i/\pi = 0.90$. The 68% confidence region is $0.72 \leq \Theta_i/\pi \leq 0.94$

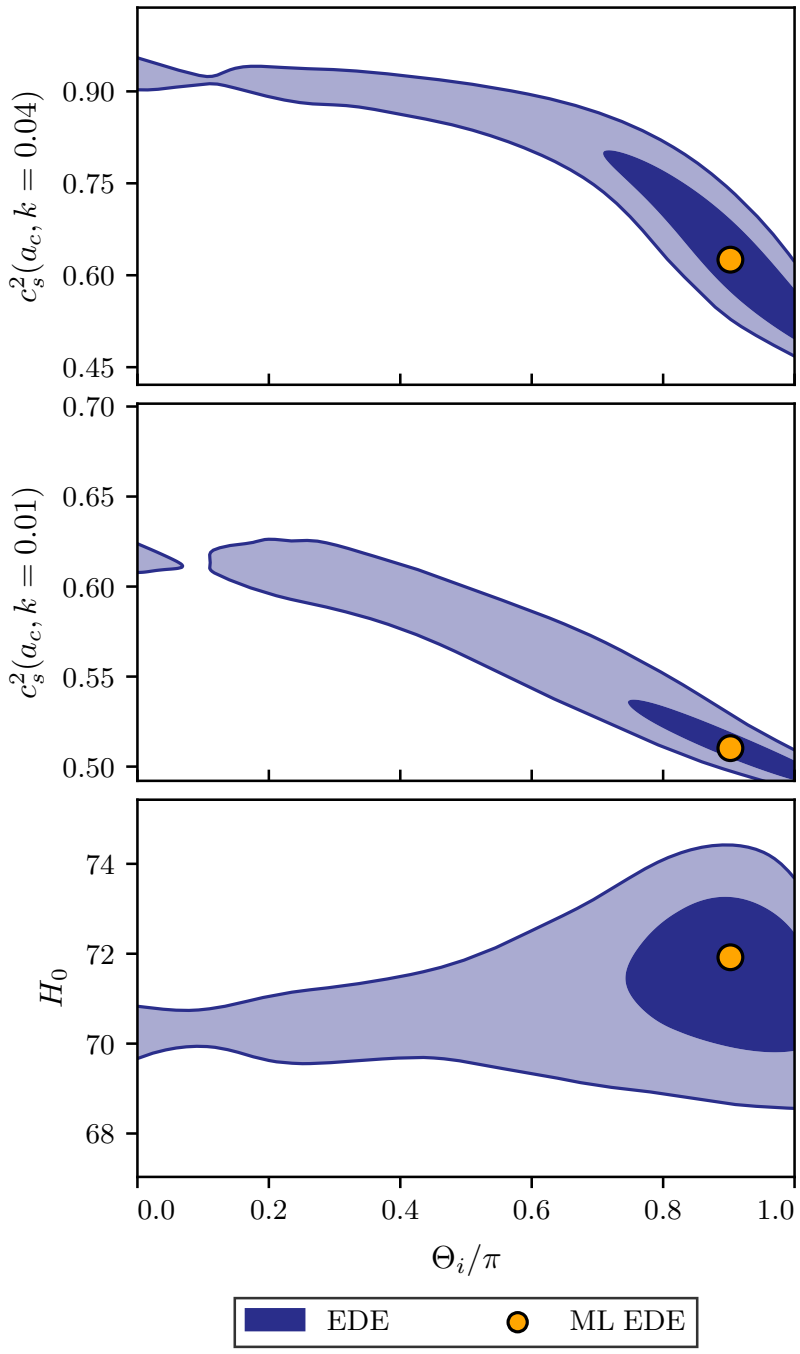

Figure 2.7: The marginalized distribution of the EDE initial phase Θ_i and some other parameters, obtained using our combined data set. The darker and lighter shades correspond respectively to the 68% C.L. and the 95% C.L. The orange circle indicates the maximum likelihood values for EDE.

and $\Theta_i/\pi < 1/2$ is excluded at 93% C.L. Note that the upper range exceeds the value required for the validity of the fluid mapping approximation, $\Theta/\pi \sim 0.96$ [1].

The reason for this preference is that Θ_i controls the minimum sound speed. Following the degeneracy line in Fig. 2.1 to $w_n = 1/2$, we would expect that for a constant sound speed $c_s^2 \approx 0.77$. Given the effective EDE sound speed of Eq. (2.16), this represents an average over the relevant timescales and wavemodes. For the ML EDE model $c_s^2(a_c, 0.01) = 0.51$ and $c_s^2(a_c, 0.04) = 0.63$ as the minimum value for each k-mode.

The scale dependence of the sound speed also explains the slightly better fit to CMB data, specifically the TE data. In Fig. 2.5, we compare the EDE and cADE residuals for their respective ML models. Notice that the TT residuals are very similar. However, in TE, by allowing the sound speed to decrease in the k range associated with $\ell < 500$, the EDE model exposes more of the driving reduction at $\ell \sim 200$ from raising $\Omega_c h^2$ as discussed above but now without adverse consequences elsewhere. This in turn better fits the low TE residuals and allows H_0 to increase further relative to the ADE model. We also show the impact of reducing Θ_i in the ML EDE model, making the sound speed closer to one at all times. The most significant effect is localized to $\ell < 500$ and in particular destroys the pattern of lower TE at $\ell \sim 200$ vs $\ell \sim 400$ compared with cADE.

We conclude that the small improvement of the EDE over ADE fit requires a specific range in the initial phase that lowers the sound speed in a scale-dependent way. Comparing to the canonical ADE mode, this improvement gives $\Delta\chi^2_{\rm tot} = -3.9$ for two extra parameters w_n, Θ_i and is therefore marginal. In the future, polarization measurements that approach the cosmic variance limit can distinguish between the EDE and ADE classes. For example, we forecast that with cosmic variance TT,TE,EE measurements to $\ell \leq 2000$, the current best fit EDE model differs from the closest ADE model by $\Delta\chi^2 = 22.4$. Furthermore the ADE model provides a general class of exact solutions where the potential energy is converted quickly to kinetic, whereas the EDE model requires a specific set of initial conditions to

achieve a similar phenomenology with an approximation to an oscillating field.

Relatedly, Ref. [34] considers a model where the scalar field oscillates in a monomial potential

$$V(\phi) \propto \phi^{2n}\,, \tag{2.20}$$

with parameters adjusted to reproduce the EDE phenomenology. This coincides with Eq. (2.14) only near the bottom of the potential, $\Theta_i \ll \pi/2$ where the potential is convex rather than concave. As pointed out in Ref. [34] the model has significantly worse performances than the EDE model. We identify here that this is related to the initial field being in the concave rather than the convex part of the potential which raises the sound speed.

Finally, while this work was nearing completion, Ref. [52] proposed that a fast-roll or kinetic energy dominated period in a two-field model might relieve the Hubble tension.

Model (Data)	ΔN	H_0	$\Delta\chi^2_{\rm tot}$	$\Delta\chi^2_{\rm CMB}$	$\Delta\chi^2_{\rm H0}$
cADE	2	70.57(70.60±0.85)	-12.7	-3.6	-8.8
ADE	3*,4	70.81(70.20±0.88)	-14.1	-3.7	-9.6
EDE	4	71.92(71.40±1.09)	-16.6	-3.7	-12.5
cADE(-POL)	2	71.93(71.55±1.05)	-12.8	-0.4	-11.2
ADE(-POL)	3*,4	72.27(71.30±1.03)	-15.1	-2.4	-11.8
EDE(-POL)	4	72.40(72.35±1.25)	-15.9	-2.9	-12.1

Table 2.2: H_0 results for the ML cADE, ADE and EDE models and posterior constraints with the joint data set and with CMB polarization data removed (-POL). ΔN is the number of additional parameters in addition to the ΛCDM ones. *Note that ML ADE in the potential conversion case where $c_s^2 = w_{\rm f}$, is essentially the same as the general case but with $\Delta N = 3$. The total $\Delta\chi^2_{\rm tot}$ relative to the ΛCDM model is broken down into contributions from the Planck CMB data sets and the local H_0 measurement.

2.6 Discussion

Acoustic dark energy, appearing around the epoch of matter radiation equality, can substantially relieve the tension between CMB inference of H_0 and local measurements, exhibited in the ΛCDM model. The presence of extra energy density lowers the CMB sound horizon

that anchors the inverse distance ladder for BAO and SN, while its disappearance before and after equality allows for a good fit to CMB data in the damping tail. Furthermore by introducing ADE at equality, the gravitational effects of raising the cold dark matter density can be balanced by the acoustic oscillations in the ADE itself.

Our main findings regarding the Hubble tension are summarized in Table 2.2 and Fig. 2.8. In all cases relieving the Hubble tension requires ADE to be a $\sim 8\%$ contribution to the total energy density around matter radiation equality, leading to at least a two parameter extension to ΛCDM.

In the general ADE class of models, the acoustic phenomenology is controlled by two additional parameters, the asymptotic equation of state $w_{\rm f}$ at late times, and the sound speed c_s^2. The sound speed plays a crucial role in the gravitational driving of CMB acoustic oscillations through its impact on the Weyl potential, leading to a strong correlation between the two, consistent with $w_{\rm f} = c_s^2 \approx 1$ around the maximum likelihood model.

Fixing these two parameters to the canonical model, cADE, leads to only a minor degradation in the ability of ADE to relax the Hubble tension in the ML model, $H_0 = 70.57$ vs. $H_0 = 70.81$. In fact, the two parameter model has the advantage of providing a more significant detection of the ADE fraction $f_c = 0.082 \pm 0.025$ and thus allows less parameter volume around the ΛCDM limit, producing a posterior centered around the ML: $H_0 = 70.60 \pm 0.85$ in cADE vs. the lower $H_0 = 70.20 \pm 0.88$ shift in ADE.

Note that the fit to the CMB data themselves improves and combined with the higher H_0 provided for an improvement of $\Delta\chi^2_{\rm tot} = -14.1$ for 3 parameters ($w_{\rm f} = c_s^2$) and $\Delta\chi^2_{\rm tot} = -12.8$ for 2 parameters ($w_{\rm f} = c_s^2 = 1$) respectively.

This class of $w_{\rm f} = c_s^2 \sim 1$ ADE models corresponds to scalar fields which convert their potential to kinetic energy efficiently around their release from Hubble drag. By setting this epoch to be around matter radiation equality, we obtain a robust mechanism for relieving the Hubble tension in a wide class of potentials.

For canonical scalar fields, we explicitly determine the requirements on the potential: that its slope allows for Hubble drag release around equality where its amplitude is set to the $\sim 8\%$ fraction required by the data. Any potential that obeys this property and efficiently converts potential to kinetic energy until the latter redshifts away will satisfy these requirements. As a proof of principle, we explicitly construct an example where the potential is locally quadratic around its release. In this model, the timing of the release to equality is not explained but the identification of this coincidence may lead to more sophisticated models where it is.

The robustness and generality of this potential-kinetic conversion mechanism for relieving the Hubble tension separates it from similar models in the literature. In Refs. [13, 34], the EDE scalar field oscillates after Hubble drag release leading to an effective fluid described by time-averaged values of $w_{\rm f}$ and c_s^2. Converting our requirements on the relationship between the two, we find that in Ref. [13], where the potential is periodic, the initial field must be on the concave part of the potential, and near the maximum to best relieve the Hubble tension. This also explains the poorer fits in Ref. [34], where the potential is convex and matches the periodic potential only near the minimum.

The periodic EDE model [13, 34] allows for a slightly higher $H_0 = 71.40 \pm 1.09$ and better $\Delta\chi^2_{\rm tot} = -16.6$ for four parameters as compared with ADE. Most of this improvement comes from the fit to the Planck polarization data. As shown in Fig. 2.8, without these data, EDE and ADE perform similarly at ML with $H_0 = 72.27$ vs 72.40 respectively. The reason is that between equality and recombination, changes in acoustic driving between raising the CDM density and adding the dark component no longer cancel. This is in fact a beneficial feature of both models since the Planck TE data show low residuals with respect to the ML ΛCDM model around $\ell \sim 200$. By allowing the effective sound speed to depend on wavenumber, the EDE model fits this region better without violating constraints elsewhere. However, when compared with our cADE model this extra improvement of $\Delta\chi^2_{\rm tot} \approx 3.9$ comes at the cost of two extra parameters and a less robust mechanism for relieving Hubble tension.

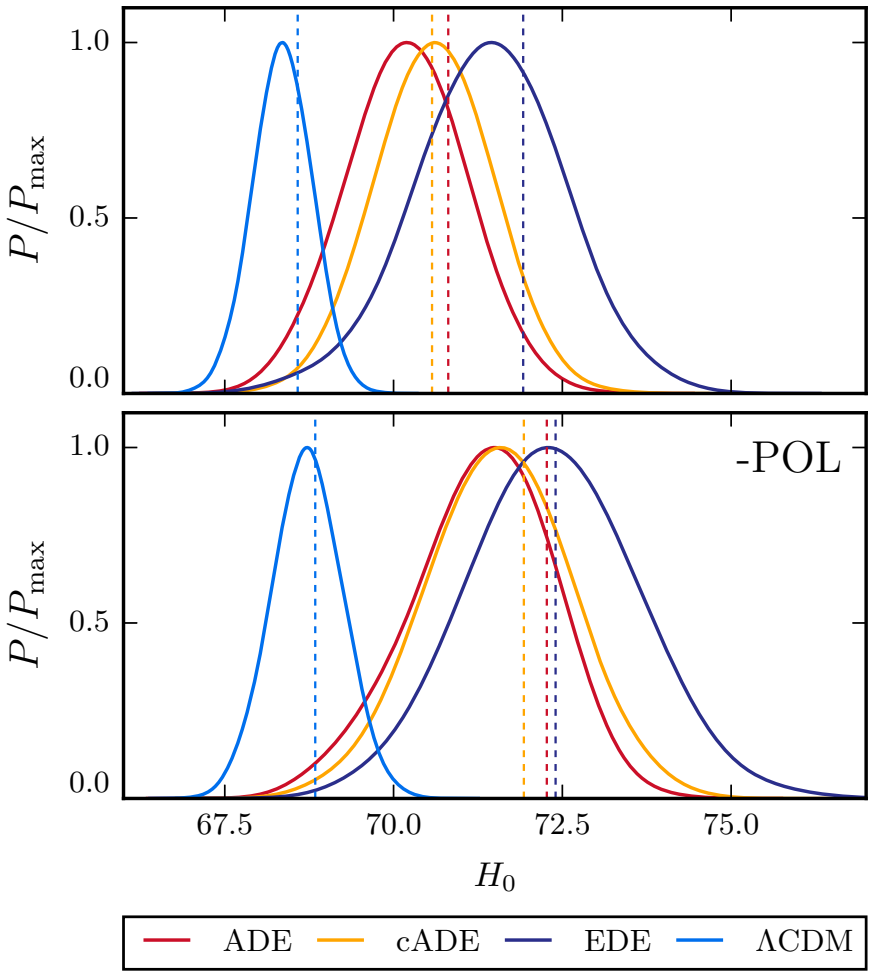

Figure 2.8: The marginalized posterior distribution of the H_0 parameter in the four models considered in Table 2.2 for two different datasets: our combined data set (upper panel) and the same with CMB polarization data removed, -POL (lower panel). The dashed vertical lines indicate the ML values for different models.

Finally, in all cases, the predicted deviations in the EE power spectrum, while not at a level testable by Planck data, are highly significant compared with cosmic variance. Future polarization data can provide key tests for these and other dark component explanations of the Hubble tension.

CHAPTER 3

TESTING H_0 IN ACOUSTIC DARK ENERGY MODELS WITH PLANCK AND ACT POLARIZATION

3.1 Introduction

While the ΛCDM model of cosmology is remarkably successful at explaining a wide range of cosmological observations, it currently fails to reconcile distance-redshift measurements when anchored at low redshift through the distance ladder and high redshift by cosmic microwave background (CMB) anisotropies. Specifically under ΛCDM, the Planck 2018 measurement of $H_0 = 67.4 \pm 0.5$ (in units of km s^{-1} Mpc^{-1} from here on) [8] is in 4.4σ tension with the latest SH0ES estimate $H_0 = 74.03 \pm 1.42$ [15].

The significance of this discrepancy makes it unlikely to be a statistical fluctuation and hence requires an explanation. A resolution of this tension may lie in unknown systematic effects in the local distance ladder and an array of alternative measurement methods are being pursued to address this possibility. For example, calibrations based on the tip of the red giant branch [53, 54], Mira variables [55], megamasers [56], lensing time delays [57, 58] all give broadly consistent results but differ in the significance of the discrepancy.

On the other hand, different CMB measurements from Planck [8], the South Pole Telescope (SPT) [59] and the Atacama Cosmology Telescope (ACT) [60, 61] give compatible distance calibrations under ΛCDM. While Planck and previous measurements weight the calibration to mainly the sound horizon, recent ground based experiments such as SPT and ACT provide precise measurements of the damping scale as well [60].

Cosmological solutions now generally require a consistent change in the calibration of both the CMB sound horizon and damping scale as standard rulers which anchor the high redshift end of the distance scale, preventing high redshift solutions that substantially change their ratio [20, 21, 22, 23, 24, 25, 26, 27, 28, 29, 30, 31, 62]. Once anchored there, the rungs

on the distance ladder through baryon acoustic oscillations (BAOs) to supernovae Type IA (SN) leave little room for missing cosmological physics in between (see e.g. [16, 17, 9, 11, 10, 18, 6, 19, 63, 64, 65, 66, 67, 68, 69, 70, 71, 72, 73, 74, 75]).

For this reason a class of models which posit a new form of energy density whose relative contribution peaks near matter radiation equality [13, 3] have received much interest [34, 52, 76, 77, 78, 79, 80, 81, 82, 83]. In these models, adding extra energy density changes the expansion rate before recombination and so the sound horizon while simultaneously tuning the timing of these contributions adjusts the damping scale as well. These models can therefore successfully raise H_0 by changing the distance ladder calibration and are limited mainly by the compensating changes to parameters in order to offset the driving of the acoustic oscillations from the Jeans-stable additional component.

These changes cause testable effects on CMB polarization, for modes that cross the horizon near matter-radiation equality [3], and on the clustering of cosmological structure, changing the amplitude and shape of the power spectrum [84, 2, 85, 86]. Differences between models in this class can also be distinguished by these effects.

Given the recent improvements in their measurement, we focus on the CMB polarization effects here and their implications for the canonical acoustic dark energy (cADE) model [3], where a scalar field with a canonical kinetic term suddenly converts its potential energy to kinetic energy by being released from Hubble drag on a sufficiently steep potential. With only two additional parameters, this model provides the most efficient and generic realization of the extra energy density scenarios.

This paper is organized as follows. In § 3.2 we briefly review the cADE model and its relationship to other models in the literature. In § 3.3 we introduce the data sets that we use to obtain the constraints presented in § 3.4. We highlight the role of ACT in § 3.4.2, Planck polarization in § 3.4.3, SH0ES in § 3.4.4 and discuss differences with other models where extra dark energy alleviates the Hubble tension in § 3.4.5. We conclude in § 3.5.

3.2 Acoustic Dark Energy

In this section we review the model parameterization of acoustic dark energy (ADE) and its relationship to early dark energy (EDE) [1] following Ref. [3]. For the purposes of this work, acoustic dark energy can be viewed either as a dark fluid component described by an equation of state $w_{\rm ADE}$ and rest frame sound speed c_s^2 [36] that becomes transiently important around matter radiation equality or as a scalar field that suddenly converts its potential energy to kinetic energy by being released from Hubble drag at that time. Adopting the former description, we model the ADE equation of state as

$$1 + w_{\rm ADE}(a) = \frac{1 + w_{\rm f}}{[1 + (a_c/a)^{3(1+w_{\rm f})/p}]^p}\,, \tag{3.1}$$

which defines its energy density

$$\rho_{\rm ADE}(a) = \rho_{\rm ADE}(a = a_c) e^{-3\int_{a_c}^{a}[1+w_{\rm ADE}(\tilde{a})]d\log\tilde{a}} \tag{3.2}$$

once normalized to its fractional energy density contribution at a_c

$$f_c = \frac{\rho_{\rm ADE}(a_c)}{\rho_{\rm tot}(a_c)}\,. \tag{3.3}$$

The ADE component therefore has a transition in its equation of state around a scale factor $a = a_c$ from $w_{\rm ADE} = -1$ to $w_{\rm f}$ which causes its fractional energy density to peak near a_c. The rapidity of the transition is determined by p, which we set $p = 1/2$ throughout as its specific value does not affect our qualitative results [3]. The connection to the scalar field picture comes from these asymptotic behaviors. Given a constant sound speed, $w_{\rm f} = c_s^2$ for a potential to kinetic conversion. We call the case of a canonical scalar field where $c_s^2 = 1$ "cADE". In §3.4.5, we widen the description to allow $w_{\rm f}$ and c_s^2 to be free parameters and call this superset "ADE". In summary, cADE is described by two parameters $\{a_c, f_c\}$ whereas

ADE is described by four parameters $\{w_{\rm f}, a_c, f_c, c_s^2\}$. When varying these parameters we impose flat, range bound priors: $-4.5 \leq \log_{10} a_c \leq -3.0$, $0 \leq f_c \leq 0.2$, $0 \leq w_{\rm f} \leq 3.6$ and $0 \leq c_s^2 \leq 1.5$.

These ADE models can be contrasted with the EDE model in its fluid description [1]. In the EDE case, the fluid behavior is modeled on a scalar field that oscillates around the minimum of its potential whose equation of state can likewise be parameterized by Eq. (3.1). In this case, $p = 1$ and $w_{\rm f} = (n-1)/(n+1)$ is a free parameter associated with raising an axion or cosine like potential to the nth power, where $w_{\rm f} \approx 1/2$ was found to best relieve the Hubble tension [13]. An additional parameter Θ_i models the initial position of the field in the potential and controls an effective, scale-dependent, sound speed (see [1, 3]). The EDE model is therefore parameterized by $\{w_{\rm f}, a_c, f_c, \Theta_i\}$. When varying these parameters we use the same priors as ADE for $\{a_c, f_c\}$ but fix $w_{\rm f} = 1/2$ and impose a flat prior on Θ_i in its range $0 \leq \Theta_i \leq \pi$.

In addition to these parameters, the full cosmological model that we fit to data also includes the six ΛCDM parameters: the angular size of the CMB sound horizon θ_s, the cold dark matter density $\Omega_c h^2$, baryon density $\Omega_b h^2$, the optical depth to reionization τ, the initial curvature spectrum normalization at $k = 0.05$ Mpc^{-1}, A_s and its tilt n_s. All these parameters have the usual non-informative priors [87]. We fix the sum of neutrino masses to the minimal value (e.g. [37]). We use the EDE and ADE implementation in CAMB [38] and CosmoMC [39] codes, following [3]. We sample the posterior parameter distribution until the Gelman-Rubin convergence statistic [40] satisfies $R - 1 < 0.01$ or better unless otherwise stated.

3.3 Datasets

In this paper, we combine several data sets relevant to the Hubble tension. We use the publicly available Planck 2018 likelihoods for the CMB temperature and polarization power

spectra at small (Planck 18 TTTEEE) and large angular scales (lowl+lowE) and the CMB lensing potential power spectrum in the multipole range $40 \leq \ell \leq 400$ [8, 87, 88]. We then compare the results to the 2015 version of the same data set [41, 42, 43] and examine the impact of the improved high-ℓ polarization data, which we sometimes refer to as "acoustic polarization" to distinguish it from the low-ℓ reionization signature.

We combine Planck data with ACT data which measures CMB temperature and polarization spectra out to higher multipoles [60]. We exclude the lowest temperature multipoles for ACT that would otherwise be correlated with Planck, following [60].

To expose the Hubble tension, we consider the SH0ES measurement of the Hubble constant, $H_0 = 74.03 \pm 1.42$ (in units of $\mathrm{km\,s^{-1}\,Mpc^{-1}}$ here and throughout) [15]. To these data sets we add BAO measurements from BOSS DR12 [45], SDSS Main Galaxy Sample [46] and 6dFGS [47] and the Pantheon Supernovae (SN) sample [44]. These data sets prevent resolving the Hubble tension by modifying the dark sector only between recombination and the very low redshift universe [17].

Our baseline configuration which we call "All" contains: CMB temperature, polarization and lensing, BAO, SN and H_0 measurements. We then proceed to examine the impact of key pieces of this combination by removing or replacing various data sets. Specifically we consider the following cases:

- All = Planck+ACT+SH0ES+BAO+Pantheon
- -ACT = All−ACT
- -P18Pol = All, but Planck 18 TTTEEE → Planck 18 TT
- -H0 = All−SH0ES
- P18→15,-ACT = -ACT, but Planck 2018→2015. This is the default combination used in [3].

cADE	All	-ACT	-P18Pol	-H0	P18 $\rightarrow$ 15,-ACT
f_c	$0.072(0.068^{+0.025}_{-0.022})$	$0.081(0.070^{+0.027}_{-0.024})$	0.105(0.110±0.030)	$0.050(0.027^{+0.008}_{-0.027})$	$0.086(0.082^{+0.026}_{-0.023})$
$\log_{10}a_c$	$-3.42(-3.43^{+0.05}_{-0.07})$	$-3.50(-3.50^{+0.07}_{-0.06})$	$-3.41(-3.39^{+0.03}_{-0.10})$	$-3.42(-3.47^{+0.24}_{-0.11})$	$-3.45(-3.46^{+0.05}_{-0.06})$
H_0	70.25(70.14±0.82)	70.60(70.19±0.86)	71.38(71.54±1.07)	$69.19(68.50^{+0.55}_{-0.93})$	70.57(70.60±0.85)
S_8	0.841(0.839±0.013)	0.841(0.839±0.013)	$0.846(0.845^{+0.018}_{-0.015})$	$0.842(0.833^{+0.011}_{-0.012})$	0.843(0.842±0.013)
$\Delta\chi^2_{\rm P}$	-0.2	-1.5	-4.3	-1.7	-4.7
$\Delta\chi^2_{\rm ACT}$	-1.8	–	-4.3	-1.0	–
$\Delta\chi^2_{\rm tot}$	-11.5	-10.7	-19.4	-1.6	-12.7
$H_0^{\Lambda\rm CDM}$	68.23(68.17±0.38)	68.29(68.22±0.40)	68.30(68.32±0.42)	67.80(67.73±0.39)	68.58(68.35±0.42)
$S_8^{\Lambda\rm CDM}$	0.815(0.818±0.010)	0.812(0.814±0.010)	0.814(0.813±0.011)	0.826(0.827±0.010)	0.819(0.819±0.010)

Table 3.1: Maximum likelihood (ML) parameters and constraints (mean and the 68% C.L. lower and upper limits) for the cADE model with different data sets. $\Delta\chi^2$ values for ML cADE model are quoted relative to the ML ΛCDM model for the same data set. $\Delta\chi^2_P$ reflects the contribution of the Planck CMB datasets involved in each case: for the -P18Pol case this includes the TT, lowl, and lowE likelihoods while for P18 $\rightarrow$ 15 this employs the Planck 15 versions of all likelihoods (see 3.3). For comparison, the H_0 and $S_8 \equiv \sigma_8(\Omega_m/0.3)^{1/2}$ values for ΛCDM model are also presented.

When highlighting the impact of a specific data component i below, we quote $\Delta\chi^2_i \equiv -2\Delta\log\mathcal{L}_i$, relative to the appropriate maximum total likelihood ($\mathcal{L}$) model under ΛCDM. For example $\Delta\chi^2_{\rm P}$ denotes the contribution from Planck CMB power spectra and includes Planck TTTEEE+lowl+lowE, except for the -P18Pol configuration where it includes Planck TT+lowl+lowE. Since the prior on the additional ADE parameters is not physically motivated we do not consider evidence based comparison of model performances.

3.4 Results

In this section we discuss all results. In § 3.4.1, we present results for cADE and the All data combination. In § 3.4.2 and § 3.4.3 we explore the impact of the ACT and 2018 improvements to the Planck data, highlighting the crucial role of polarization. In § 3.4.4, we show that the ability to raise H_0 in cADE is not exclusively driven by the SH0ES measurement. We discuss how polarization measurements distinguish between cADE and the wider class of ADE and EDE models in § 3.4.5.

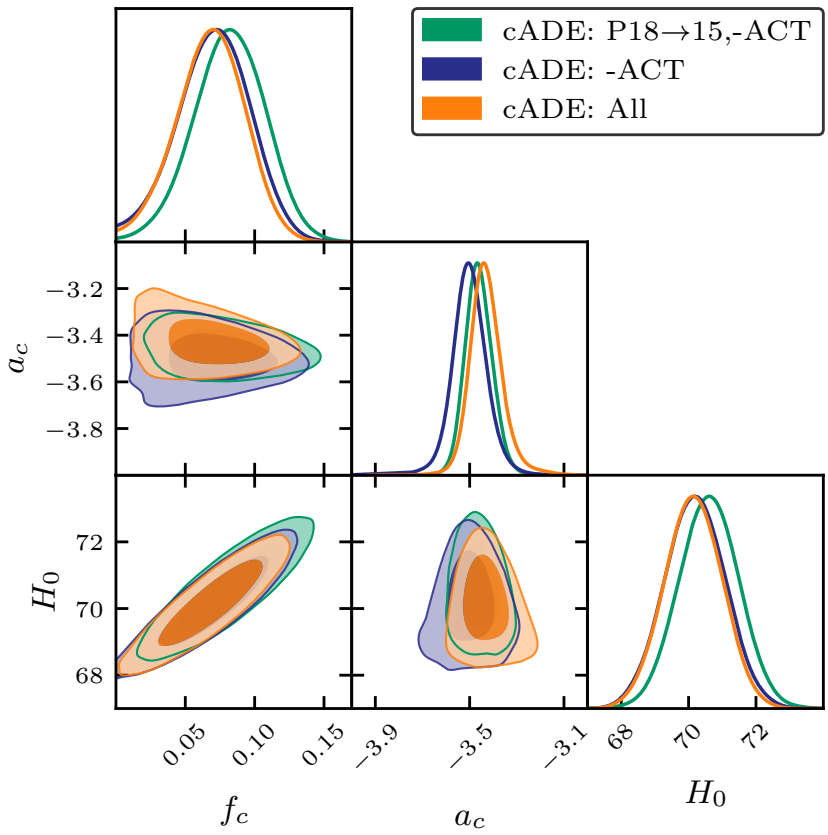

Figure 3.1: The marginalized joint posterior of parameters of the cADE model for data sets that highlight the impact of ACT and the 2018 update to the Planck data. The darker and lighter shades correspond respectively to the 68% C.L. and the 95% C.L.

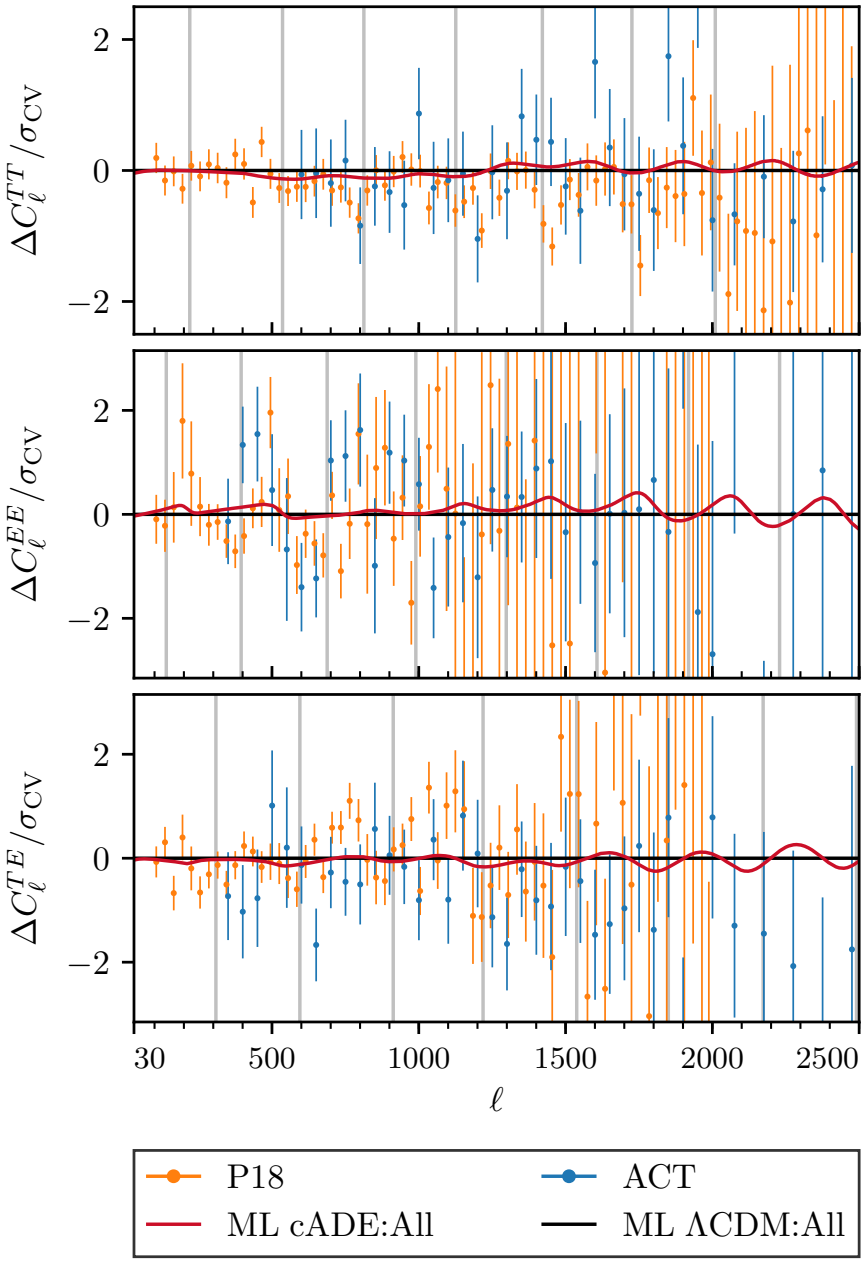

Figure 3.2: CMB residuals of Planck 2018 (orange points) and ACT (blue points) data and the ML cADE model (red curve) with respect to the ML ΛCDM model (black line) with both optimized to All data. The gray vertical lines indicate the positions of the acoustic peaks in the ML ΛCDM:All model.

3.4.1 All data

We begin with results for the All data combination and the cADE model. In Fig. 3.1, we show the constraints on the additional cADE parameters f_c and a_c as well as their impact on H_0. The mean value for f_c is 2.8 standard deviations from zero, which we will refer to as a 2.8σ detection, and its distribution is strongly correlated with that of H_0. In Tab. 3.1 we also show the maximum likelihood (ML) parameters, notably $H_0 = 70.25$ in cADE vs. 68.23 in ΛCDM, as well as the improvement of fit over ΛCDM, a total of $\Delta\chi^2_{\rm tot} = -11.5$ for 2 additional parameters. The portion that comes from Planck CMB power spectra, $\Delta\chi^2_{\rm P} = -0.2$ and from ACT $\Delta\chi^2_{\rm ACT} = -1.8$, reflects a slightly better fit to CMB power spectra than ΛCDM. Note that the ML value for a_c is near matter-radiation equality. Since the ML of a class of models depends on the dataset it is optimized to, from this point forward we refer to such models as e.g. ML cADE:All and ML ΛCDM:All.

In Fig. 3.2, we show the model and data residuals, both for Planck and ACT, of the ML cADE:All model relative to the ML ΛCDM:All model. The residuals are shown in units of $\sigma_{\rm CV}$, the cosmic variance error per multipole moment for the ML ΛCDM:All model

$$\sigma_{\rm CV} = \begin{cases} \sqrt{\frac{2}{2\ell+1}} C_\ell^{TT}, & \text{TT}\,; \\ \sqrt{\frac{1}{2\ell+1}} \sqrt{C_\ell^{TT} C_\ell^{EE} + (C_\ell^{TE})^2}, & \text{TE}\,; \\ \sqrt{\frac{2}{2\ell+1}} C_\ell^{EE}, & \text{EE}\,. \end{cases} \tag{3.4}$$

In spite of the higher H_0, the ML cADE:All model closely matches the ML ΛCDM:All model for all spectra and relevant multipoles. Along the $f_c - H_0$ degeneracy, f_c adjusts the CMB sound horizon scale to match the acoustic peak positions while a_c near matter-radiation equality allows the damping tail of the CMB to match as well. Note that the ACT data provide a new test, that has been successfully passed, for this class of solution by providing more sensitive polarization constraints than Planck in the damping tail $\ell \gtrsim 10^3$ as we shall

discuss in the next section. Since adding an extra Jeans-stable energy density component drives CMB acoustic oscillations and changes the heights of the peaks, small variations in $\Omega_c h^2, \Omega_b h^2, n_s$ are required as well, and these correlated changes remain mainly the same as those shown in Ref. [3]. We shall see below that a crucial test that distinguishes cADE and related explanations of the Hubble tension is the imperfect compensation in the polarization, especially at intermediate multipoles that correspond to modes that cross the horizon near a_c [3]. Relatedly, as shown in Tab. 3.1, the higher $\Omega_c h^2$ and H_0 values exacerbate the high $S_8 = \sigma_8(\Omega_m/0.3)^{1/2}$ values of ΛCDM so that accurate measurements of local structure test these scenarios as well [84, 2, 85, 86].

3.4.2 ACT impact

The ACT data provide better constraints than Planck on the CMB EE polarization spectrum at $\ell \gtrsim 10^3$ as well as competitive TE and corroborating TT constraints in this range. The former provides new tests of the cADE model as shown in Fig. 3.2. On the data side, it is notable that for TT the Planck data residuals compared with ΛCDM that oscillate with the acoustic peaks (gray lines) at $\ell \gtrsim 10^3$ are echoed in ACT data, albeit at a lower significance. We shall see below that were it not for Planck polarization constraints at lower multipole, the cADE fit to these oscillatory TT residuals would drive H_0 even higher. The additional constraining power of ACT polarization at high ℓ reduces the model freedom there and slightly shifts the compensation in acoustic driving toward higher a_c and lower $\Omega_b h^2$. This change in a_c can be seen in Fig. 3.1 where we also show the impact of removing ACT data. On the other hand the ability to raise H_0 is nearly unchanged.

Interestingly, the ACT TE data is not in good agreement with the Planck data as noted in [60] and attributed to $\sim 5\%$ calibration difference leading to ΛCDM parameter discrepancies at the 2.7σ level. In Fig. 3.2, we see that the Planck TE data have residuals that oscillate with the acoustic frequency when compared with ΛCDM, whereas the ACT TE data do not.

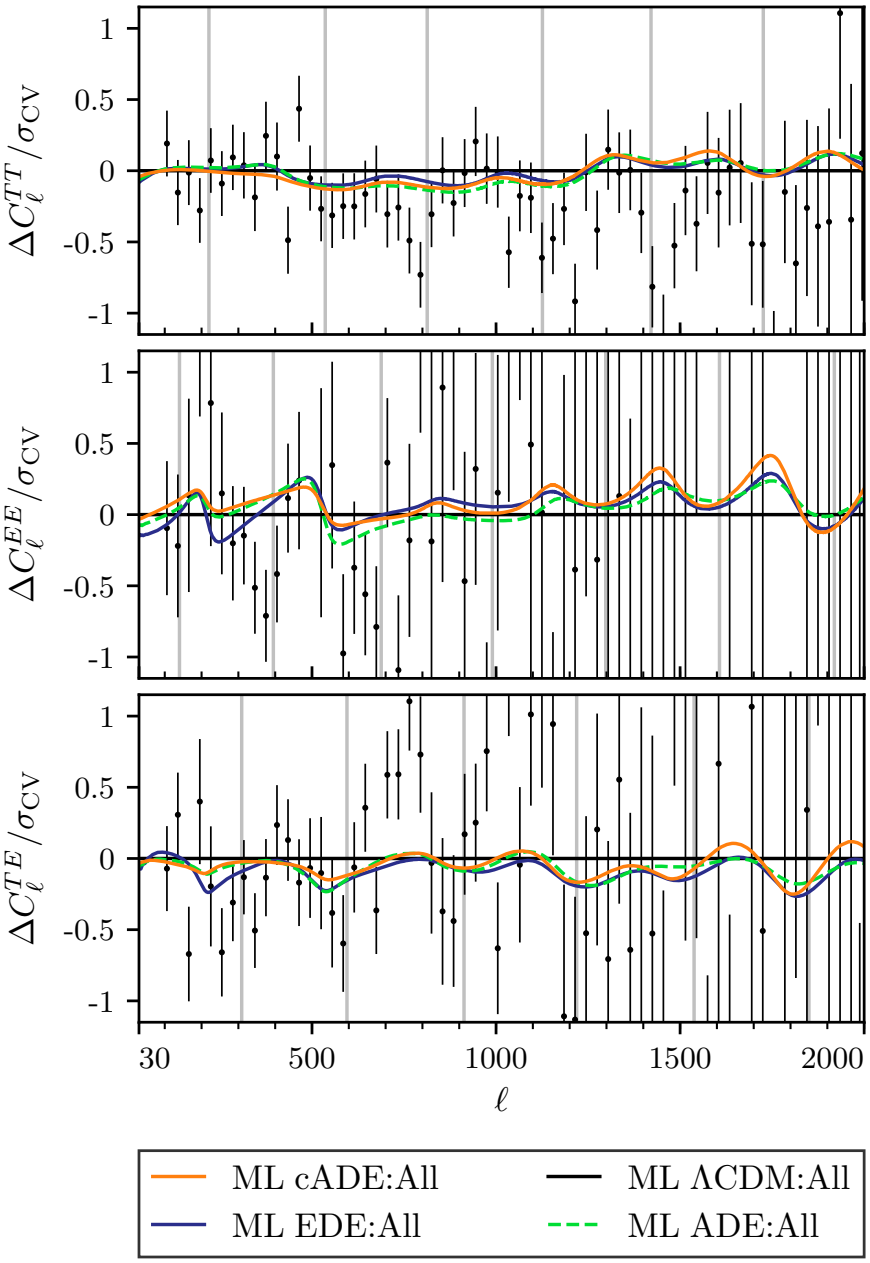

Figure 3.3: Planck CMB data residuals and the ML cADE, ADE and EDE models relative to the ML ΛCDM model, all optimized to All data. The gray vertical lines indicate the positions of the acoustic peaks in the ML ΛCDM:All model.

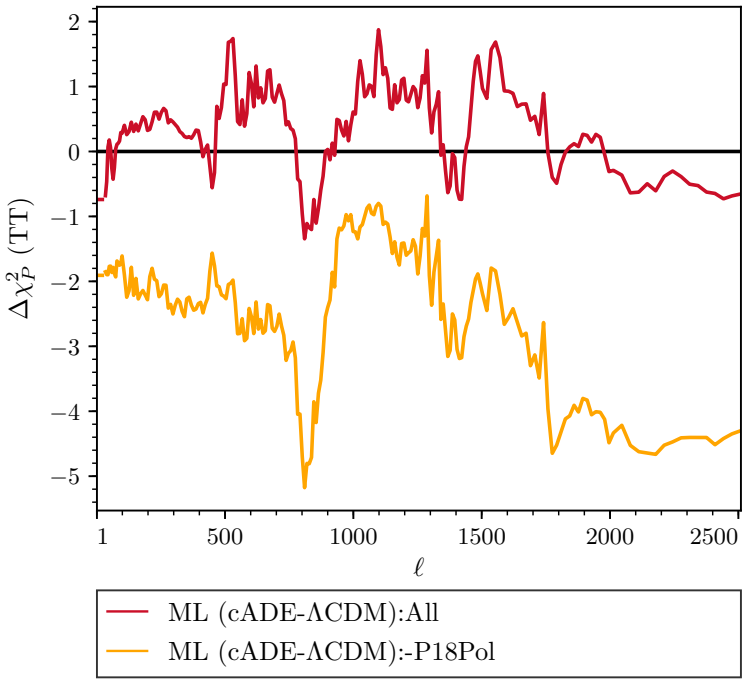

Figure 3.4: Cumulative $\Delta\chi^2_{\rm P}$ for the Planck 18 TT+lowl+lowE likelihoods between ML cADE and ML ΛCDM models, optimized to either All or -P18Pol data. Note that All includes the Planck 18 TTTEEE likelihood whereas -P18Pol does not.

The ML cADE:All model attempts to compensate but must then compromise on the fit to the high-ℓ power spectra. This tradeoff has important implications for the comparison of cADE and ΛCDM as well as cADE and alternate models that add extra energy density near matter-radiation equality. This data discrepancy also motivates the study of the impact of Planck polarization data below.

3.4.3 Planck impact

Planck 2015 vs. 2018 data

We start with the impact of the Planck 2018 data relative to the older 2015 release studied in [3] by reverting the data and removing ACT data in P18→15,-ACT. The main difference in the updated Planck data is the better polarization data and control over systematics, which makes both the TE and EE data important tests of the cADE model.

In Fig. 3.1 and Tab. 3.1, we see that the main impact on cADE is a slight reduction of its ability to raise H_0 and a shift to lower a_c that is countered by the ACT data in the All combination. This mild tension reflects the competition between fitting the high multipole spectra of both Planck and ACT and the intermediate multipole ($\ell \sim 500$) range of the Planck TEEE data. The latter is a critical test of the cADE scenario since the perturbation scales associated with them cross the horizon near matter-radiation equality and are highly sensitive to changes in the manner the acoustic oscillations are driven. Polarization data represent a cleaner test than temperature data since they lack the smoothing effects of the Doppler and integrated Sachs-Wolfe contributions. On the other hand, as we have seen Planck and ACT disagree somewhat on the TE spectrum in this range.

In Fig. 3.3 we highlight the Planck 2018 data residuals and ML cADE:All model residuals, both relative to ML ΛCDM:All model. Notice again the oscillatory residuals in TE and the features in cADE that respond to these residuals as well as the features in EE at $\ell \lesssim 600$.

Furthermore, because of the ability to adjust Planck foregrounds, the overall amplitude of the TT data residuals, which have foregrounds fixed to the best fit to Planck 18 alone for visualization in Fig. 3.3, are low compared with the models. To better isolate the regions of the data that impact the models the most, we also show the cumulative $\Delta\chi^2_{\rm P}$ contributed by the Planck TT+lowl+lowE data in Fig. 3.4 for the ML cADE:All relative to ML ΛCDM:All model. While the ML cADE:All model successfully minimizes differences with ΛCDM, there are notable regions where the $\Delta\chi^2_P$ changes rapidly: $\ell \sim 500$, 800, 1400. Note that the latter two regions are near the 3rd and 5th TT acoustic peaks and are related to the oscillatory TT residuals. We shall next see that these areas reflect the trade-off between fitting the high ℓ power spectra of Planck and ACT and the intermediate scale polarization spectra of Planck.

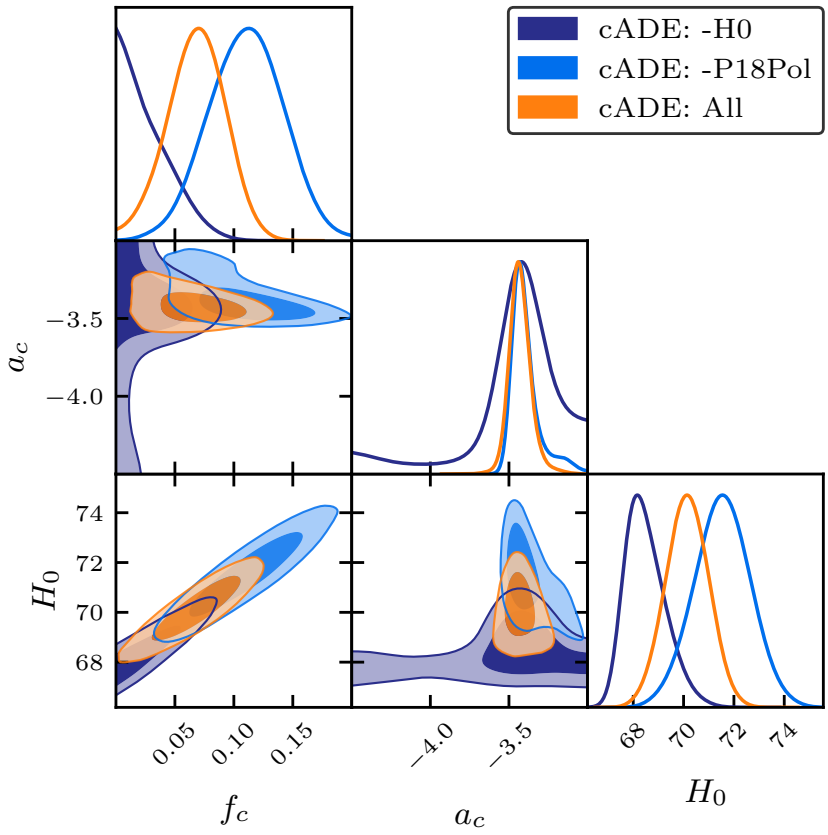

Figure 3.5: The marginalized joint posterior of parameters of the cADE model for data sets that highlight the role of Planck 2018 acoustic polarization data and SH0ES H_0 measurements. The darker and lighter shades correspond respectively to the 68% C.L. and the 95% C.L.

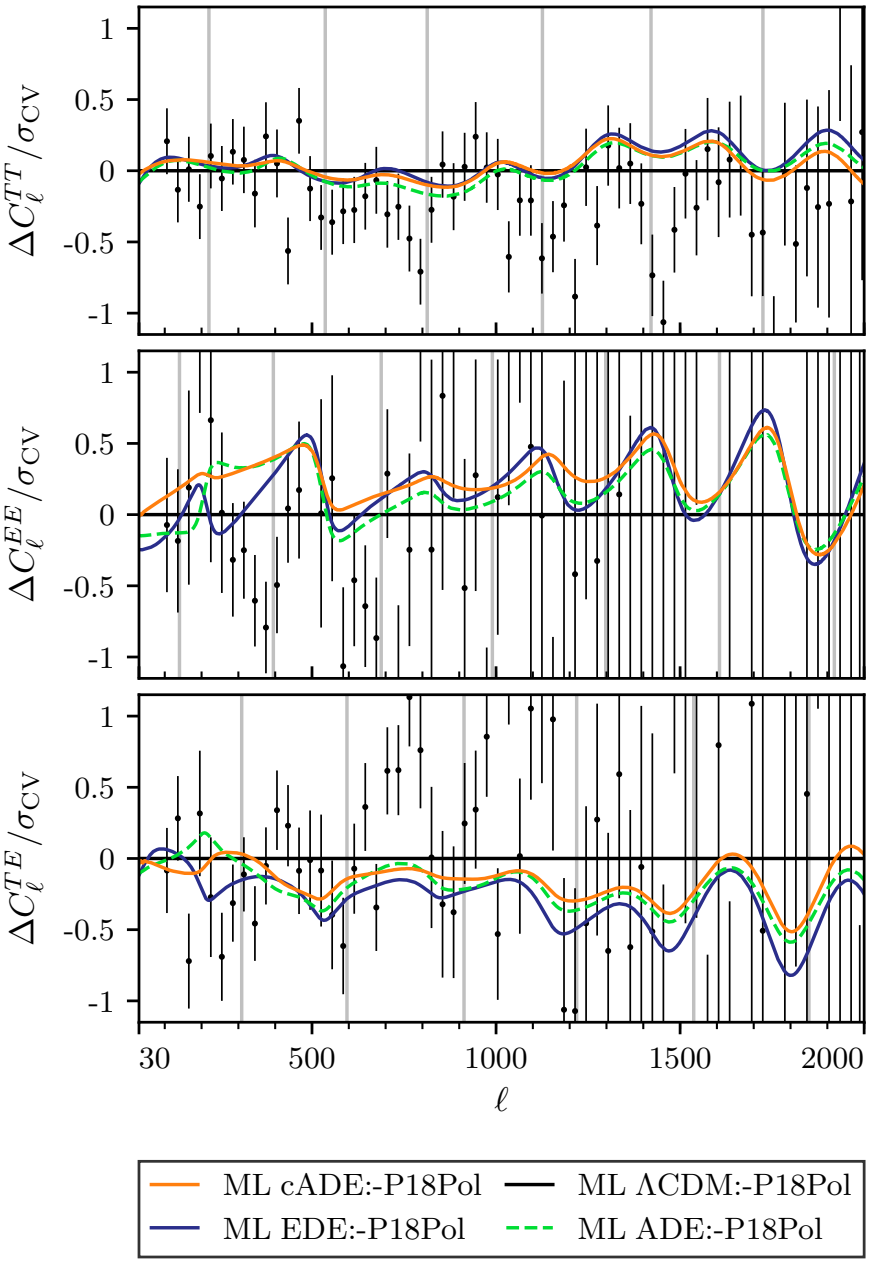

Figure 3.6: Planck CMB data residuals and the ML cADE, ADE and EDE models relative to the ML ΛCDM model, all optimized to the -P18Pol data. The gray vertical lines indicate the positions of the acoustic peaks in the ML ΛCDM:-P18Pol model.

Planck polarization impact

The crucial role of intermediate scale TE and EE data in distinguishing models and the discrepancy between the TE calibrations of Planck and ACT motivate a more direct examination of the impact of Planck polarization data. In Fig. 3.5 and Tab. 3.1, we show the cADE parameters and H_0 constraints without the Planck 2018 acoustic polarization data but including acoustic polarization data from ACT as -P18Pol. Notice that the ability to raise H_0 increases to $H_0 = 71.38$ for the ML cADE:-P18Pol model and total $\Delta\chi^2_{\rm tot}$ improvement over ΛCDM rises to -19.4. Correspondingly, a finite f_c is preferred at $\sim 3.7\sigma$ and its ML value increases to $f_c = 0.105$. The fit to both the remaining Planck CMB power spectra data and ACT temperature and polarization data correspondingly also improve by -4.3 and -4.3 respectively. The transition scale a_c can also further increase in value, especially at lower f_c.

In Fig. 3.6, we show how the ML cADE:-P18Pol model fits residuals in the Planck TT data relative to the ML ΛCDM:-P18Pol model. Notice that the cADE model now responds to the oscillatory TT residuals. In Fig. 3.4, we see that the main cumulative TT improvement comes from $\ell \gtrsim 1400$.

On the other hand, Planck polarization data at intermediate scales ($\ell \sim 500$) strongly disfavor this solution. In Fig. 3.7, we compare the cumulative Planck TTTEEE $\Delta\chi^2$ for the ML cADE:All model vs the ML cADE:-P18Pol model, both relative to their respective ML ΛCDM models.[1] While the former remains flat, reflecting an equally good fit for the cADE, the latter encounters a sharp degradation in the fit just below $\ell \sim 500$ and a more gradual degradation between $500 - 1000$. The first degradation is associated with features in the EE spectrum and the second receives contributions from the uniformly low TE spectrum in Fig. 3.6. Since the Planck polarization data are far from cosmic variance limited even just

1. The value of the cumulative $\Delta\chi^2_{\rm P}$(data) at the highest ℓ matches the values in Tab. 3.1 only for the cases where the optimization matches the data, i.e. ML cADE:-P18Pol in Fig. 3.4 and ML cADE:All in Fig. 3.7.

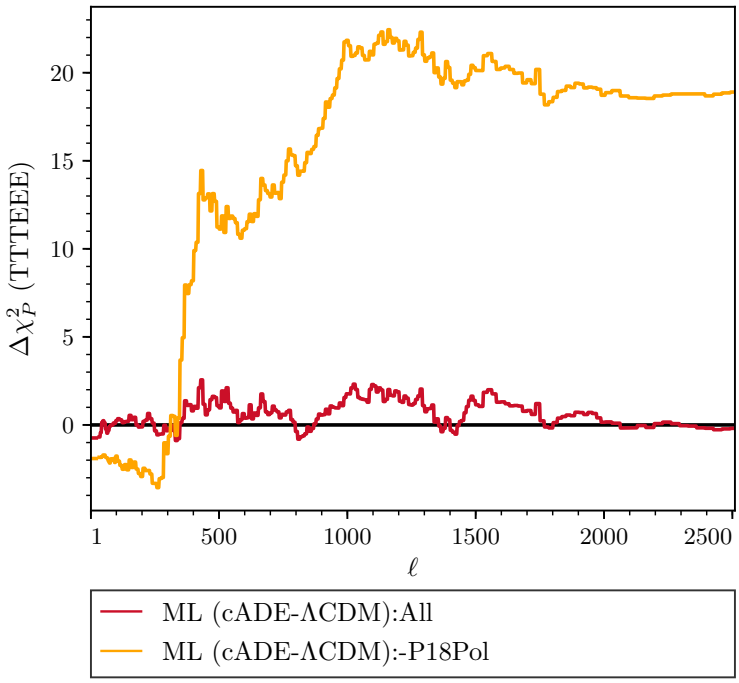

Figure 3.7: Cumulative $\Delta\chi^2_{\rm P}$ for the Planck 18 TTTEEE +lowl+lowE likelihoods between ML cADE and ML ΛCDM models, optimized to either All or -P18Pol data. Note that -P18Pol replaces the TTTEEE with the TT likelihood.

statistically, future data in this region can provide a sharp test of cADE and distinguish it from alternatives.

3.4.4 SH0ES impact

Given the highly significant H_0 tension in ΛCDM, it is interesting to ask whether preference for a higher H_0 in cADE simply reflects the SH0ES H_0 data. In Fig. 3.5 and Tab. 3.1, we show the impact of removing this data. Notice that although the ML value of H_0 drops to 69.19, the cADE constraints still allow a non-Gaussian tail to the higher H_0 values that are compatible with the All data. The ML cADE:-H0 model remains a better fit to both Planck and ACT temperature and polarization data than the ML ΛCDM:-H0 model which has a lower $H_0 = 67.8$. In this case, finite values for the cADE parameter f_c are no longer significantly preferred. Since all cADE models become indistinguishable from ΛCDM in the

	$\Delta\chi^2_{\rm tot}$	H_0	f_c	$\log_{10}a_c$	$w_{\rm f}$	c_s^2 or Θ_i/π
ADE (ALL)	-14.0	$70.25(69.67^{+0.93}_{-0.97})$	$0.061(0.055^{+0.028}_{-0.030})$	$-3.60(-3.57^{+0.20}_{-0.12})$	$0.55(1.37^{+0.37}_{-1.09})$	0.70(0.87±0.29)
EDE (ALL)	-16.6	$71.03(71.14^{+0.98}_{-0.99})$	$0.056(0.061^{+0.018}_{-0.017})$	$-3.71(-3.68^{+0.09}_{-0.07})$	0.5(fixed)	0.94(>0.84)
ADE (-ACT)	-11.9	70.55	0.074	-3.61	0.68	0.80
EDE (-ACT)	-13.7	71.61	0.068	-3.80	0.5(fixed)	0.92
ADE (-P18Pol)	-23.7	72.11	0.103	-3.51	0.57	0.85
EDE (-P18Pol)	-26.1	73.07	0.100	-3.65	0.5(fixed)	0.90
ADE (-H0)	-3.9	69.18	0.049	-3.58	0.81	0.71
EDE (-H0)	-4.0	70.11	0.044	-3.69	0.5(fixed)	0.94
ADE (P18→15,-ACT)	-14.1	$70.81(70.20^{+0.87}_{-0.88})$	0.086(0.079±0.033)	$-3.52(-3.50^{+0.14}_{-0.08})$	$0.87(1.89^{+0.85}_{-1.07})$	$0.86(1.07^{+0.30}_{-0.20})$
EDE (P18→15,-ACT)	-16.6	$71.92(71.40^{+1.07}_{-1.05})$	$0.074(0.064^{+0.020}_{-0.018})$	$-3.72(-3.72^{+0.10}_{-0.07})$	0.5(fixed)	0.90(>0.82)

Table 3.2: ML parameters and constraints (mean and the 68% C.L. lower and upper limits) for of cADE, ADE, EDE models with different data sets. $\Delta\chi^2_{\rm tot}$ values are quoted relative to the ML ΛCDM model for the same data set. The column labeled "c_s^2 or Θ_i/π" indicates c_s^2 for ADE and Θ_i/π for EDE. Since the boundary $\Theta_i/\pi = 1$ is consistent with the data, we have quoted the 1-sided 68% CL lower interval from this boundary. Both ADE and EDE have four parameters in addition to ΛCDM, but the $w_{\rm f}$ value of EDE is crudely optimized by setting it to the value of best solving the H_0 tension following [1].

limit $f_c \to 0$, there is a large prior parameter volume associated with the poorly constrained a_c that favors ΛCDM, pulling the posterior probability of H_0 to lower values and skewing the distribution.

3.4.5 Distinguishing model alternatives

As we have seen in the previous sections, intermediate scale polarization data is crucial for limiting the ability of the cADE model to raise H_0 as well as distinguishing it from ΛCDM. This is because differences in acoustic driving are most manifest for modes that cross the horizon while the additional energy density is important and the signatures in polarization vs. temperature spectra are clearer, due to the lack of other contaminating effects.

Intermediate scale polarization is equally important for distinguishing cADE from the wider class of ADE models or EDE models. In Tab. 3.2 we show results for these wider classes and the joint posterior of the common parameters along with H_0 are shown in Fig. 3.8. The ADE chains are converged at the $R-1 < 0.04$ level, reflecting degeneracies in poorly constrained parameters. Note that both models possess 4 additional parameters, but for EDE we have followed [1] in crudely optimizing $w_{\rm f}$ by setting it to $w_{\rm f} = 0.5$. In the ADE

case the ML H_0 value remains at $H_0 = 70.25$ in cADE while in EDE case it rises to 71.03. The total $\Delta\chi^2_{\rm tot}$ for the All dataset also improves from -11.5 to -14.0 and -16.6 respectively for 2 additional parameters. The All dataset therefore does not strongly favor either increase in model complexity. Note that because of the large parameter volume in ADE near $f_c \to 0$, the posterior of H_0 in that case is strongly pulled by the prior to lower values than the ML value. For EDE notice that in the scalar field interpretation $\Theta_i/\pi = 1$ is a field whose initial value is at the top of the potential and the data require a moderate tuning to this boundary value [3].

Tab. 3.2 also displays the ML models for the various other data combinations discussed above. The trends are similar to those discussed for cADE. In addition, for ADE, the All data favors a lower value for $w_{\rm f}$ due mainly to the ACT data as compared with the P15-based previous results from Ref. [3].

More interestingly for the future, Figs. 3.2 and 3.6 show that the current compromises between fitting the high ℓ power spectra of Planck and ACT vs. the intermediate scale Planck polarization data are model dependent, especially in the polarization spectra around $\ell \lesssim 500$. Since the Planck data are far from cosmic variance limited in TEEE, better measurements in this regime can distinguish between the various alternatives for adding extra energy density around matter radiation equality to alleviate the Hubble tension.

3.5 Discussion

The acoustic dark energy model, which is based on a canonical kinetic term for a scalar field which rapidly converts potential to kinetic energy around matter radiation equality, alleviates the Hubble tension in ΛCDM and successfully passes new consistency tests in the CMB damping tail provided by the ACT data, while being increasingly constrained and distinguished from alternate mechanisms by the better intermediate scale polarization data from Planck. The best fit cADE model has $H_0 = 70.25$ compared with 68.23 in ΛCDM

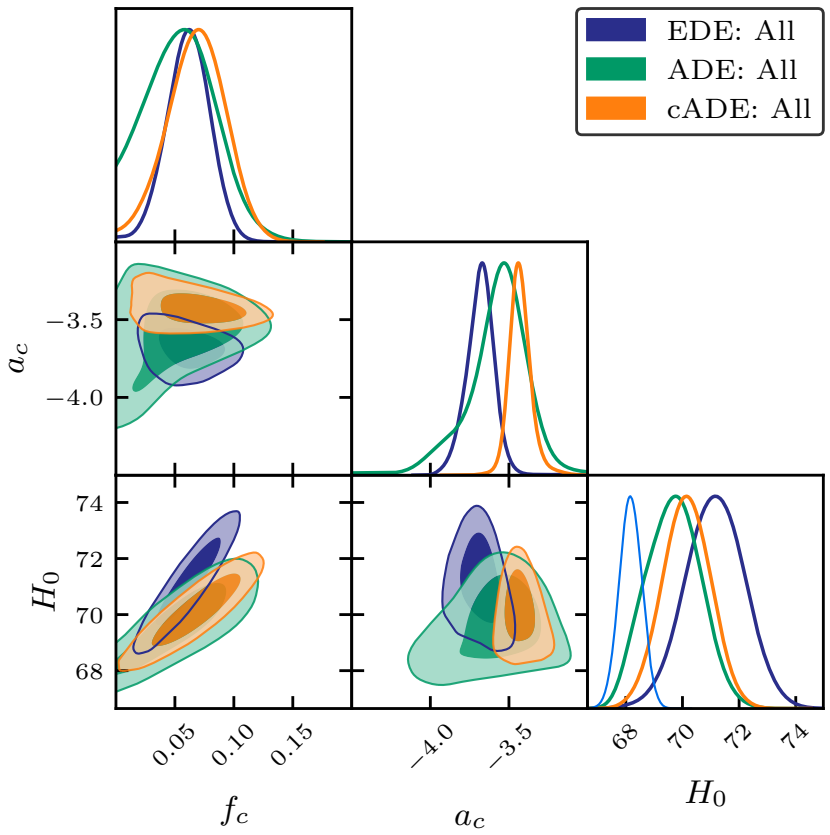

Figure 3.8: The marginalized joint posterior of parameters of different models for the All data. The darker and lighter shades correspond respectively to the 68% C.L. and the 95% C.L. The 1-D H_0 distribution of ΛCDM: All chain is also shown as the light blue curve.

and a finite cADE component is preferred at the 2.8σ level. While this preference is driven by the SH0ES measurement of H_0 itself, even without this data the cADE model prefers a higher H_0 than in ΛCDM.

Intermediate scale ($\ell \sim 500$) polarization data plays a critical role in testing these and other scenarios where an extra component of energy density alters the sound horizon and damping scale of the CMB. Such components also drive CMB acoustic oscillations leaving particularly clear imprints on the polarization of modes that cross the horizon around matter radiation equality. Were it not for the Planck 2018 polarization data, the ML cADE model would have $H_0 = 71.38$ and more fully resolve the Hubble tension. Intriguingly the ACT TE data do not agree with Planck TE data in their normalization [60] and in cADE the two data sets drive moderately different preferences in parameters, especially the epoch a_c at which its relative energy density peaks. In the wider class of non-canonical acoustic dark energy (ADE) or early dark energy (EDE), which differ in the manner that acoustic oscillations are driven, polarization data at these scales is critical for distinguishing models, with the current freedom allowing an even larger $H_0 \sim 70 - 71$ and $71 - 73$ at ML with and without Planck polarization, albeit with two additional parameters.

Given the current statistical and systematic errors in measurements, future intermediate scale polarization data can provide even more incisive tests of the cADE model and its alternatives to resolving the Hubble tension.

CHAPTER 4

THE EARLY DARK SECTOR, THE HUBBLE TENSION, AND THE SWAMPLAND

4.1 Introduction

The Early Dark Energy (EDE) model [13] is a prominent candidate to resolve the Hubble tension [89]. However, this model faces challenges both from data, in the form of exacerbated tensions with large-scale structure observations [2, 84, 85], and from theory, namely whether the model can be self-consistently described as a low-energy limit of a high-energy theory including gravity. To understand the interplay of these challenges, in this work we take guidance from the *Swampland Distance Conjecture* [90] (and its extension to axions [91, 92, 93, 94]), and extend EDE to an Early Dark *Sector*.

The Hubble tension, namely, the discrepancy in the value of the Hubble constant H_0 measured locally via the cosmic distance ladder using Type Ia supernovae (SNIa) [15, 95] and the value inferred from the cosmic microwave background (CMB) [8], from large-scale structure (LSS) [96, 97, 98, 99, 100, 101], and from other probes [89], presents a challenge to the standard ΛCDM cosmological model. In particular, the disagreement between *Planck* 2018 CMB observations and the SH0ES 2020 cosmic distance ladder measurement stands at 5.0σ statistical significance [7], with the two values given by $H_0 = 67.37 \pm 0.54$ km/s/Mpc [8] and $H_0 = 73.04 \pm 1.04\,\mathrm{km/s/Mpc}$ [7], respectively. While some local measurements have yielded H_0 values that are not in statistical disagreement with the ΛCDM-predicted value from CMB and LSS data (e.g., [53, 58]), it is generally true that local H_0 probes have yielded higher values than expected in ΛCDM.

A plethora of cosmological models have been proposed to bring these data sets into concordance, and resolve the Hubble tension. For a recent review see, e.g., [102]. These range from modifications to the early (pre-recombination) universe, to the late universe, and

to the theory of gravity in the local universe. However, all approaches face severe challenges: For example, late universe models that leave the sound horizon at the drag epoch unchanged are heavily constrained by the inverse cosmic distance ladder and generally cannot explain the SH0ES measurement [103]. Early universe models that reduce the the sound horizon at recombination can successfully raise the Hubble constant while maintaining consistency with CMB observations, but are often in tension with LSS observations, namely the galaxy clustering and cosmic shear auto- and cross-correlation two-point functions from the Dark Energy Survey Year 1 [2] and BOSS full-shape anisotropic galaxy clustering [84]; see also [104] and [105]. Nonetheless, the relative success of early universe models at raising the inferred H_0 motivates the search for an embedding into a more complete and yet still well motivated model that is consistent with all data sets. Several recent models have been proposed along these lines, e.g., [106, 107, 108].

An interesting case study is Early Dark Energy [13]. In this class of models, the expansion rate is increased near matter-radiation equality, so as to reduce the sound horizon at recombination, and thereby raise the H_0 value inferred from the angular scale of the sound horizon. The model can accommodate larger values of H_0 than ΛCDM whilst not degrading the fit to the CMB, and is thereby compatible with both SH0ES and *Planck*. However, the larger H_0 is accompanied by shifts in other ΛCDM parameters, such as the dark matter density $\Omega_c h^2$, the scalar spectral index n_s, and the amplitude of density perturbations σ_8. This brings the model into tension with LSS data [2, 84, 85]. Accordingly, when additional LSS data are included in the analysis, e.g., from the Dark Energy Survey, the Kilo-Degree Survey (KiDS) [109, 110], and the Subaru Hyper Suprime-Cam (HSC) survey [111], or from BOSS [84], the evidence for an EDE component is significantly diminished [2, 84, 85] (see [112] for an alternative viewpoint).

The minimal EDE model is comprised of a scalar field ϕ with a potential $V(\phi) = V_0 \left[1 - \cos(\phi/f)\right]^n$. This potential, first proposed in [113], is a generalization of the usual

axion potential (see [114] for a review). In this model, the relative energy density in ϕ is peaked at a critical redshift z_c, at which point the scalar field constitutes a fraction $f_{\rm EDE} \equiv \rho_\phi(z_c)/\rho_{tot}(z_c)$ of the energy density of the universe. The parameters of the model follow from simple considerations: $n \geq 2$ so as to have the EDE field's energy density rapidly redshift away following z_c, $V_0^{1/4} \sim$ eV so as to constitute $\approx 10\%$ of the universe at $z_{\rm eq}$, and $f \lesssim M_{pl}$ so as to endow the scalar with a mass $m \sim H(z_{\rm eq})$ and thereby set $z_c \sim z_{\rm eq}$.

This model is, at best, a phenomenological description of a more complicated theory. The conventional origin of periodic axion potentials is instantons. A complete model would need to explain why a tower of instantons $V(\phi) \sim \sum_n c_n e^{-S_n} \cos(n\phi/f)$, with S_n the instanton action, conspires to take the required form, despite the Planckian decay constant $f \sim M_{\rm pl}$, which would conventionally be associated with a total breakdown of the instanton expansion (see, e.g., [115, 116, 117]). One might presuppose that the model exists as a low-energy limit of a UV-complete theory, e.g., that EDE is in the landscape of string theory [118, 119], and that the low-energy parameter fine-tunings are sensible from the UV perspective. However, it might equally well be the case that the EDE model is in the swampland [120, 90]. So-called "swampland conjectures" (for a review, see [121, 122, 123]) attempt to delineate the boundaries of the landscape, and identify those properties that low-energy theories inherit from the high-energy theory. In particular, the Swampland Distance Conjecture [90] holds that any Planckian field excursion $|\Delta\phi| \sim M_{\rm pl}$, such as that in EDE, causes an exponential suppression of the mass of other fields in the theory, $m \propto e^{-c|\Delta\phi|/M_{\rm pl}}$, with $c > 0$ a number of $\mathcal{O}(1)$.

In this work we study the interplay of the swampland and the EDE model. We consider the impact of the Swampland Distance Conjecture (SDC) [90] (and its extension to axions [91, 92, 93, 94]) on the EDE inference of H_0 and on the tension of EDE and LSS data [2, 84, 85]. To this end, we promote EDE to an *Early Dark Sector* (EDS). We consider an

EDE-dependence of the mass of dark matter, given by,

$$m_{\rm DM}(\phi) = m_0 e^{c\phi/M_{pl}}, \tag{4.1}$$

where ϕ is initially $\phi_i \in [0, \pi f]$, and is zero in the present universe. We assume for simplicity that the above applies to all of the dark matter (as also considered in, e.g., the "Fading Dark Matter" model [124, 125]). The SDC prediction is that c is positive and order-1, such that the dark matter is exponentially lightened when ϕ rolls from $\phi_i \sim M_{\rm pl}$ to $\phi \sim 0$. We perform data analysis allowing c to vary, and allow the data to decide both the magnitude and sign of c.

We find that positive c ($c > 0$), which is the sign of c predicted by the SDC, raises S_8 and exacerbates the tension with LSS data in this model. On the other hand, we find that a small but negative c can lower S_8 without decreasing H_0, while simultaneously improving the fit to the CMB. This occurs due to an interplay of imprints on the cosmic microwave background, both at high-ℓ and on scales that enter the horizon around z_c, and imprints on the growth of structure, caused by a relative shift in the redshift of matter-radiation equality and by an induced attractive dark matter self-interaction (a dark-matter-philic "fifth-force") [1].

We perform a Markov Chain Monte Carlo (MCMC) analysis of a ('baseline') combined data set comprised of *Planck* 2018 primary CMB and CMB lensing data [127, 8, 128]; BAO distances from the SDSS DR7 main galaxy sample [46], the 6dF galaxy survey [129], and SDSS BOSS DR12 [45]; the Pantheon supernovae data set [44]; and the SH0ES H_0 measurement. We find a modest overall preference for $c < 0$, with the best-fit value $c = -5 \times 10^{-3}$.

We find that the EDS model is able to accommodate a lower S_8 than in EDE, and thereby lessen the tension with LSS data. To substantiate this, we supplement our baseline

1. This is related but distinct from the "cosmic axion force" [126]; in that work an ultra-light scalar mediates an interaction with the Standard Model, whereas in the in the EDS model the interaction is confined to the dark sector.

data set with Dark Energy Survey Year-3 data (DES-Y3) [14], approximated as a prior on $S_8 \equiv \sigma_8(\Omega_{\rm m}/0.3)^{0.5}$, and we repeat the MCMC analysis. We find that the best-fit EDS is better able to accommodate the DES-Y3 measurement than is EDE, with a relative reduction in $\chi^2_{\rm DES-Y3}$ of 1.1. However, like previous analyses [2, 84, 85], we find that the combined data set including DES-Y3 is statistically consistent with $f_{\rm EDE} = 0$, indicating that there is little Bayesian justification for this 4-parameter extension of ΛCDM.

Finally, we study the impact of recent CMB temperature and polarization data from the Atacama Cosmology Telescope (ACT) [130, 131]. The ACT DR4 data significantly improve upon the precision of *Planck* on small angular scales. The ACT collaboration analysis of the EDE model [132] found a moderate preference for $f_{\rm EDE} > 0$, in contrast to results from *Planck*. We perform an MCMC analysis of the EDS model fit to the baseline data set supplemented with ACT DR4 temperature and polarization spectra. Analogous to the EDE analysis of [132], we find that the inclusion of ACT data increases the preference for $f_{\rm EDE} > 0$, and significantly constrains the timing z_c. We find a factor of two improvement on the constraint on c relative to the baseline data set.

Turning these analyses on their head, we may ask what the data, when analyzed in the context of the EDE model, have to say about the Swampland Distance Conjecture. We find a 95% CL upper limit on c given by $c < 0.068$ for the baseline data set, and $c < 0.035$ and $c < 0.042$ at 95% CL when DES-Y3 or ACT are included, respectively. We interpret this as a modest tension between the Swampland Distance Conjecture and the EDE model, at the level of a $4 - 7\%$ fine-tuning.

The structure of this paper is as follows. In Sec. 4.2 we introduce the Early Dark Sector model, the dynamics, and the physics behind it. In Sec. 4.3 we detail the imprint on the cosmic microwave background and on large-scale structure. In Sec. 4.4 we discuss the data sets that will be used in our analyses, and perform MCMC analyses of the model fit to varying data set combinations. We detail the implications of this for the Swampland Distance

Conjecture in Sec. 4.4.4, and conclude in Sec. 4.5.

We work in natural units, where the speed of light is unity. The parameter c refers exclusively to the coupling parameter of the EDS model, and not the speed of light. We denote the reduced Planck mass $M_{\rm pl}(= 2.435 \times 10^{18}$ GeV). Unless otherwise stated, values for H_0 are given in units of km/s/Mpc.

4.2 From Early Dark Energy to The Early Dark Sector

The idea underlying the EDE model [13] is to shrink the comoving sound horizon at last scattering, r_s, defined by

$$r_s(z_*) = \int_{z_*}^{\infty} \frac{\mathrm{d}z}{H(z)} c_s(z), \tag{4.2}$$

with z_* the redshift of last scattering and c_s the sound speed of the photon-baryon plasma, through the inclusion of an additional source of energy density, namely the EDE. The reduced sound horizon allows an increased H_0 while remaining consistent with CMB observations of the *angular scale* of the sound horizon, θ_s, defined by,

$$\theta_s = \frac{r_s(z_*)}{D_A(z_*)}, \tag{4.3}$$

where D_A is the angular diameter distance to last scattering. By adjusting the redshift dependence of the EDE component, the CMB damping scale can simultaneously be adjusted to match observations, albeit at the expense of introducing a tuning or coincidence into the EDE model.

The baseline EDE model [13] is described by a canonical scalar field, with potential energy given by

$$V(\phi) = m^2 f^2 \left[1 - \cos\frac{\phi}{f}\right]^3. \tag{4.4}$$

This potential, of the form first proposed in [113], is a generalization of the usual axion

potential, corresponding to a careful fine-tuning of an instanton expansion or of other non-perturbative effects (see, e.g., the discussion in [2]). Alternative realizations and variations on the EDE model abound, see, e.g., [13, 76, 34, 52, 3, 79, 78, 82, 133, 77].

The common feature of these models is that the energy density transitions between redshifting slower than ordinary matter to redshifting faster across a critical redshift. In the baseline EDE model this is achieved as follows. At early times the scalar is frozen in place by Hubble friction, and effectively behaves as dark energy. The scalar is released from Hubble friction when $H \simeq m$, for a typical value of the initial field $\phi_i = \mathcal{O}(f)$. Around this time, the scalar field makes its maximal contribution to the energy density of the universe, i.e., the ratio of energy densities

$$f_{\rm EDE}(z) \equiv \frac{\rho_{\rm EDE}(z)}{\rho_{\rm tot}(z)}, \tag{4.5}$$

where $\rho_{\rm tot}$ is the total energy density, is maximal when $z = z_c$. As a shorthand, we will denote $f_{\rm EDE} \equiv f_{\rm EDE}(z_c)$, and will explicitly specify $f_{\rm EDE}(z)$ when referring to the above. At times after z_c, i.e., at lower redshifts, the field rolls down the potential $V(\phi)$ and undergoes damped oscillations. The energy density of the scalar rapidly redshifts away, naively leaving no trace in the post-recombination universe.

One can easily estimate the model parameters necessary to resolve the Hubble tension. The sound horizon and damping scale are most sensitive to dynamics that occur in the decade of redshift preceding last scattering [11]. This effectively imposes $z_c \sim z_{\rm eq}$, which in turn determines the mass parameter m as

$$m \sim 10^{-27}{\rm eV}. \tag{4.6}$$

Meanwhile, the discrepancy in the Hubble constant H_0 is roughly 10%, which, combined

with $\phi_i = \mathcal{O}(f)$ by standard arguments (see, e.g., [114]), implies that

$$V(z \sim z_c) \sim 0.1\, H_{\rm eq}^2 M_{\rm pl}^2, \tag{4.7}$$

and hence,

$$f \sim M_{\rm pl}. \tag{4.8}$$

Thus we see the EDE scalar field, insofar as it is relevant to the Hubble tension, naturally undergoes a field excursion $|\Delta\phi| \sim f \sim M_{pl}$.

Little is known about field theories near the Planck scale. At these scales one can reasonably expect quantum gravity effects, e.g., from string theory, to become relevant. When assessing models, in lieu of a concrete string theory construction, one approach is to take guidance from known calculable string theory examples, distilled into a simple set of conjectures – so-called "Swampland" conjectures [120] (for a review, see [121, 122, 123]). The Swampland conjectures collectively aim to delineate the boundary between effective field theories that are inconsistent once gravity is quantized (or more precisely, EFTs that do not admit a UV completion into quantum gravity [121]), and those that are consistent with quantum gravity (and hence do admit UV completion).

Of particular relevance to EDE is the SDC [90]. The SDC holds that any low-energy effective field theory is only valid in a region of field space bounded by the Planck scale, and the breakdown of effective field theory that occurs at Planckian field excursions is encoded in an exponential sensitivity of the mass spectrum of the effective theory. This can be expressed as, for the mass of at least one such field in the spectrum,

$$M \sim M_0 e^{-\alpha|\Delta|/M_{\rm pl}}, \tag{4.9}$$

where Δ is the distance traversed in field space, and α is an order-1 parameter. There are numerous concrete examples that support the SDC. For example, consider a universe with

an extra dimension that is a circle of radius R. Dimensional reduction on the circle yields a tower of massive Kaluza-Klein excitations, with masses given by

$$m_n^2 \simeq n^2 M_{\rm pl}^2 e^{-2\varphi/M_{\rm pl}}, \tag{4.10}$$

where $\varphi \equiv M_{\rm pl}\log(M_{\rm pl}R)$ is the canonically normalized radius of the circle. At large field values $\varphi \gtrsim M_{\rm pl}$, the Kaluza-Klein fields become exponentially light and a priori cannot be neglected. For other examples of the scaling in Eq. (4.9), see, e.g., the review in [123].

The EDE scenario is precisely the sort of model that the SDC is designed to address, namely a model with Planckian field excursions. While this is not unique to EDE, and is exhibited also in late-universe dark energy models, such as quintessence [134], the EDE model is unique in that this exponential sensitivity is activated in the high-redshift universe. Thus one might hope that cosmological observables such as the CMB and LSS may be powerful probes of the couplings predicted by the SDC, e.g., of the form in Eq. (4.9), in the EDE model.

With all this in mind, in this work we consider a simple model that implements these ideas. We extend the EDE model to the Early Dark *Sector* (EDS), and consider a coupling of the EDE field to dark matter of the form predicted by the SDC. While fields that exhibit the mass scaling in Eq. (4.9) could in principle be an arbitrary fraction of the total dark matter, for simplicity we assume ϕ couples to all dark matter. As a concrete model, we consider the following Lagrangian:

$$\mathcal{L} = \frac{1}{2}(\partial\phi)^2 + i\bar{\psi}\not{D}\psi - V(\phi) - m_{\rm DM}(\phi)\bar{\psi}\psi, \tag{4.11}$$

where ϕ is the EDE scalar with potential $V(\phi)$ and ψ is a fermionic cold dark matter candidate with ϕ-dependent mass $m_{\rm DM}(\phi)$. We consider the specific form of the potential

$V(\phi)$ given by Eq. (4.4), and a field-dependent mass $m_{\rm DM}(\phi)$ given by

$$m_{\rm DM}(\phi) = m_0 e^{c\phi/M_{\rm pl}}, \tag{4.12}$$

as motivated by the SDC, and in particular the extension of the SDC to axions [91, 92, 93, 94]. In our work we fix the convention that ϕ decreases over the course of cosmic evolution, i.e., ϕ evolves from $\phi_i > 0$ in the early universe to $\phi_f \sim 0$ in the present universe. The SDC then predicts that c defined by Eq. (4.12) is positive ($c > 0$), such that the dark matter mass is decreased by a Planckian field excursion of ϕ. In what follows, we refer to the system defined by Eqs. (4.11), (4.12), and (4.4), as the EDS model.

The background cosmology of the EDS model Eq. (4.11) is specified by the Friedmann equations, along with the scalar field equation of motion,

$$\ddot{\phi} + 2aH\dot{\phi} + a^2\frac{dV}{d\phi} = -a^2\frac{c}{M_{\rm pl}}\rho_{\rm DM}, \tag{4.13}$$

where dot denotes a derivative with respect to conformal time and $H = (1/a)\mathrm{d}a/\mathrm{d}t$ where t is cosmic time, and the conservation equation for the joint stress-energy of the dark matter and scalar field. The latter leads to the modified continuity equation for the dark matter density,

$$\dot{\rho}_{\rm DM} + 3aH\rho_{\rm DM} = \frac{c}{M_{\rm pl}}\dot{\phi}\rho_{\rm DM}. \tag{4.14}$$

A full derivation of the equations of motion at the background and linear-perturbation level is given in App. A.1. We may understand the background cosmology in a relatively straightforward way. On the dark matter side, Eq. (4.14) may be solved exactly, to give the evolution of the dark matter density at all times. We find

$$\rho_{\rm DM}(a) = \frac{3M_{\rm pl}^2 H_0^2 \Omega_{\rm DM}}{a^3}\frac{m_{\rm DM}(\phi)}{m_{\rm DM}(\phi_0)}, \tag{4.15}$$

with $m_{\rm DM}(\phi_0)$ the present-day dark matter mass. This is consistent with the conservation of the comoving DM number density, $a^3 n_{\rm DM}(a) = 3M_{\rm pl}^2 H_0^2 \Omega_{\rm DM}/m_{\rm DM}(\phi_0)$. Meanwhile, the scalar field may be understood as evolving in a time-dependent effective potential, which can be read off from Eq. (A.6) as

$$V_{\rm eff}(\phi, a) \equiv V(\phi) + \rho_{\rm DM}(a), \tag{4.16}$$

where $\rho_{\rm DM}(a)$ is given by Eq. (4.15).

As a fiducial numerical example, we consider the best-fit model in the fit to primary CMB, CMB lensing, BAO, SNIa, and SH0ES data, to be presented later in this work (see Tab. 4.1). We will refer to this example throughout; the parameters (to be varied in Sec. 4.3 and sampled in our MCMC analysis) are given by, for the EDS parameters,

$$\begin{aligned} f_{\rm EDE} &= 0.142, & \log_{10}(z_c) &= 3.58, \\ \theta_i \equiv \frac{\phi_i}{f} &= 2.72, & c_\theta \equiv c \cdot \frac{f}{M_{\rm pl}} &= -0.0010, \end{aligned} \tag{4.17}$$

where we have defined c_θ as c in units of f, analogous to the rescaling of ϕ into θ, and

$$\begin{aligned} 100\theta_s &= 1.04114, & \Omega_b h^2 &= 0.02284, \\ \Omega_c h^2 &= 0.13043, & \log(10^{10} A_s) &= 3.079, \\ n_s &= 0.9931, & \tau &= 0.0600, \end{aligned} \tag{4.18}$$

for the ΛCDM parameters. The corresponding particle physics parameters are given by

$$\begin{aligned} c &= -0.0049, & \phi_i &= 0.55 M_{\rm pl}, \\ f &= 0.20 M_{\rm pl}, & m &= 5.4 \times 10^{-28}\,{\rm eV}, \end{aligned} \tag{4.19}$$

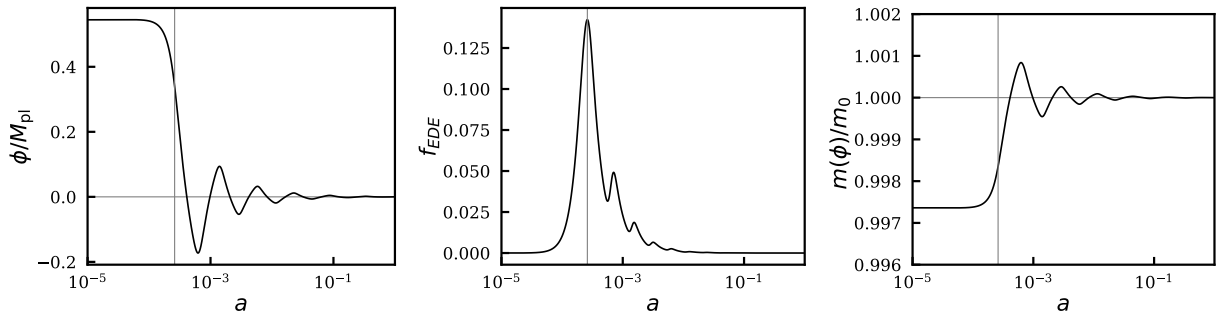

Figure 4.1: Fiducial example background evolution of the scalar field, the energy density fraction $f_{\rm EDE}$, and the dark matter mass $m_{\rm DM}(\phi)$. The vertical lines indicate the location of z_c. The scalar field indeed undergoes a Planckian field excursion (up to an order-1 factor), leading to a $\approx 0.3\%$ change to $m_{\rm DM}$ around z_c. See Eq. (4.17) for parameters.

implying a change in the dark matter mass,

$$\frac{\Delta m_{\rm DM}}{m_{\rm DM}} \equiv \frac{m(\phi_i) - m_0}{m_0} = -0.003. \tag{4.20}$$

The tension-related derived cosmological parameters are given by

$$\begin{aligned} H_0 &= 72.52\,, \qquad & S_8 &= 0.848, \\ \sigma_8 &= 0.848, \qquad & \Omega_m &= 0.3000, \end{aligned} \tag{4.21}$$

which can be compared with the SH0ES 2020 measurement $H_0 = 73.2 \pm 1.3$ [95], and the DES-Y3 measurements [14] $S_8 = 0.776 \pm 0.017$, $\Omega_m = 0.339^{+0.032}_{-0.031}$, and $\sigma_8 = 0.733^{+0.039}_{-0.049}$. Note that SH0ES has been included in the data sets that are used in this fit, while DES-Y3 has not. We will discuss in detail the tension with and interplay between these data sets in Sec. 4.4.

The cosmological evolution of the EDE scalar field, the fractional energy density $f_{\rm EDE}(z)$, and the dark matter mass $m_{\rm DM}(\phi)$, for the above parameters, are shown in Fig. 4.1. The scalar field undergoes an $\mathcal{O}(M_{\rm pl})$ excursion, and near $z = z_c = 3801$ comprises 14% of the energy density of the universe. This energy density is rapidly dissipated as the field rolls

down the potential and begins to oscillate, and at $z = 10^3$ its contribution is less than 2% of the energy density of the universe. The dark matter mass undergoes a fractional change corresponding to a mass that is 0.3% lighter in the early universe than in the late universe.

The equations of motion for linear perturbations of the scalar field and dark matter may be derived following the same procedure as for the background evolution, namely, from the variation of the action with respect to the scalar field perturbations and the conservation of the perturbed joint stress-energy tensor (see App. A.1). In the synchronous gauge, we find for the scalar field perturbation,

$$\ddot{\delta\phi} + 2aH\dot{\delta\phi} + \left(k^2 + a^2\frac{d^2V}{d\phi^2}\right)\delta\phi + \frac{\dot{h}}{2}\dot{\phi} = -a^2\frac{c\rho_{\rm DM}}{M_{\rm pl}}\delta_c, \tag{4.22}$$

and for the dark matter,

$$\dot{\delta}_c + \theta + \frac{\dot{h}}{2} = \frac{1}{M_{\rm pl}}c\dot{\delta\phi}, \tag{4.23}$$

$$\dot{\theta} + aH\theta = \frac{1}{M_{\rm pl}}ck^2\delta\phi - \frac{1}{M_{\rm pl}}c\dot{\phi}\theta, \tag{4.24}$$

where $\theta \equiv \partial_i v^i$ and h is the trace of the spatial metric perturbation. These results are specific to the choice of SDC-inspired dark matter mass dependence in Eq. (4.12); the equations of motion for a general ϕ-dependent dark matter mass $m(\phi)$ are given in App. A.1. The phenomenology of perturbations will be discussed in detail in Sec. 4.3.

Finally, we note the model we consider here is similar to, but distinct from, the modified gravity implementation of coupled EDE in [108]. While both setups include a field-dependent dark matter mass, here we consider an axion-like sinusoidal $V(\phi)$, Eq. (4.4), whereas [108] considered a monomial $V(\phi) = \lambda\phi^4$. These two choices for $V(\phi)$ are known to exhibit different phenomenology; see, e.g., the discussion in [34, 76].

4.3 Phenomenology: The CMB and the Growth of Structure

Here we investigate the novel EDS impact of the coupling between the scalar field and dark matter on the CMB and large-scale structure of the Universe.

4.3.1 CMB

In Fig. 4.2, we show the impact of varying c with the other parameters fixed to their values in Eqs. (4.17) and (4.18) compared with the Planck TT, EE, TE data. The various models are plotted as differences with respect to the best-fit model to baseline data set in units of the cosmic variance per multipole,

$$\sigma_{\rm CV} = \begin{cases} \sqrt{\frac{2}{2\ell+1}} C_\ell^{TT}, & TT\,; \\ \sqrt{\frac{1}{2\ell+1}} \sqrt{C_\ell^{TT} C_\ell^{EE} + (C_\ell^{TE})^2}, & TE\,; \\ \sqrt{\frac{2}{2\ell+1}} C_\ell^{EE}, & EE, \end{cases} \tag{4.25}$$

of the best-fit model. From the $\Delta c = \pm 0.02$ parameter variations around the best-fit $c = -0.005$, which is comparable to the scale of its observational errors, we can see that the main effects on the TT power spectrum of decreasing c is a localized decrease in power near $\ell \sim 500$ and an increase in power at high multipole moments $\ell \gtrsim 700$.

These effects are induced by the gravitational effects of the change of dark matter mass on the CMB acoustic oscillations. These gravitational effects come through the Newtonian gauge Weyl potential $\Psi + \Phi$; see, e.g., [6]. The change in the Weyl potential drives acoustic oscillations, especially around the epoch that the oscillations reach their first extrema $kr_s(z) = \pi$ where r_s is the comoving sound horizon. In Fig. 4.3, we show the time evolution of the Weyl potential and dark matter mass for the $\Delta c = -0.02$ model with respect to the best-fit EDS model. The Weyl potential is shown in blue and orange curves for $k = 0.038$ and $0.0857\,\mathrm{Mpc}^{-1}$, which correspond to $\ell \sim 500$ and 1100, respectively. The dashed ver-

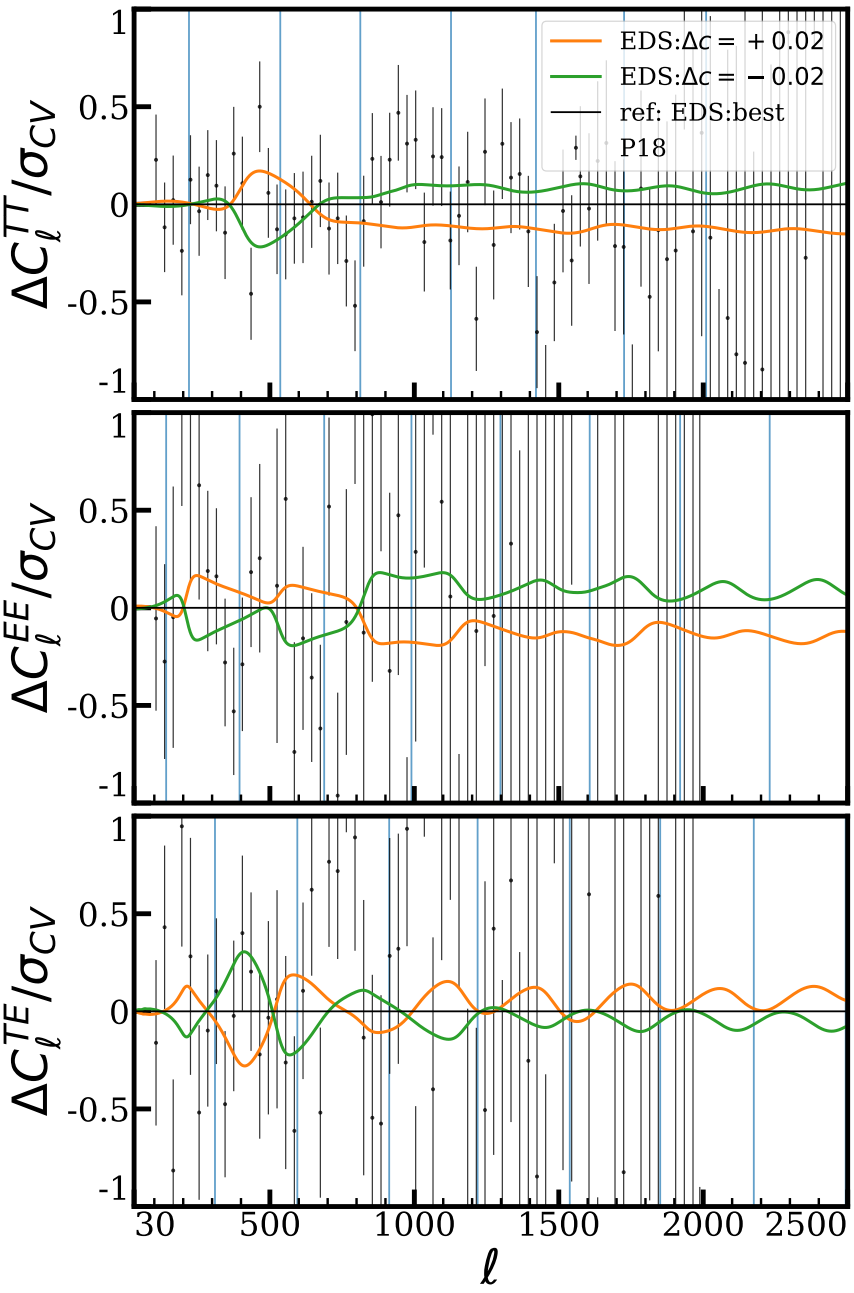

Figure 4.2: Planck 2018 data residuals relative to the EDS best-fit model to the baseline data set. Models with $\Delta c = \pm 0.02$ around the best-fit -0.005 with all other parameters fixed to their values in Eqs. (4.17) and (4.18) are shown for comparison. The blue vertical lines indicate the positions of the acoustic peaks in the best-fit EDS model.

tical lines indicate locations where $kr_s(z) = \pi$ for each k mode with the same color, and the shaded area indicates the epoch between z_c and recombination. We see that the Weyl

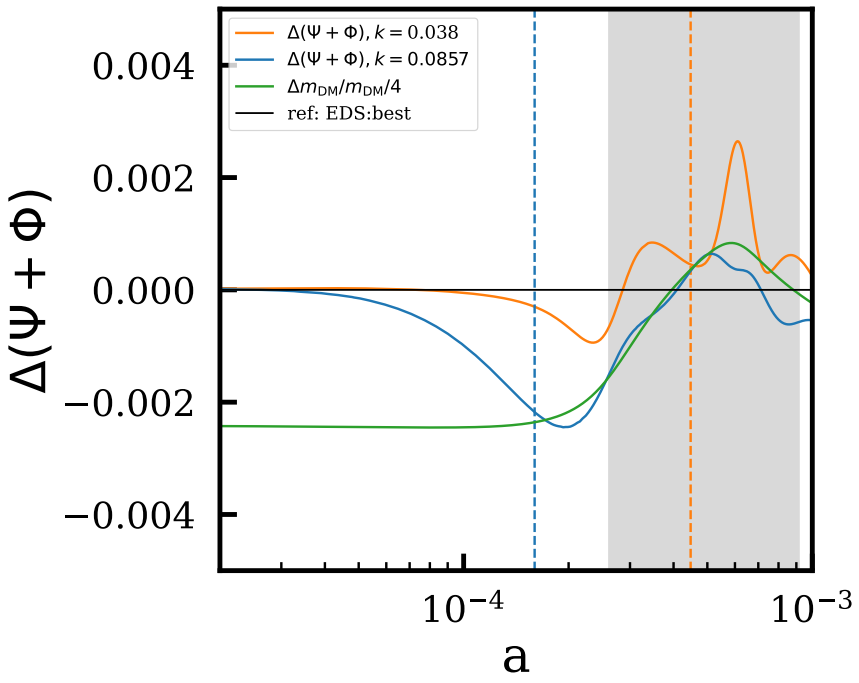

Figure 4.3: Time evolution of Weyl potential, in units of the initial comoving curvature pertubation, and the dark matter mass for $\Delta c = -0.02$ with respect to the best-fit EDS model. All the other parameters are fixed to their values in Eq. (4.17) and (4.18). The dashed vertical lines indicate locations of $kr_s(a) = \pi$ for each k mode with the same color where r_s is the comoving sound horizon. The shaded area indicates the epoch between z_c and recombination.

potential change follows the dark matter mass change, which oscillates with time. For a negative c, the dark matter mass is smaller before z_c and larger during an epoch between z_c and recombination. For modes that cross $kr_s = \pi$ well before z_c, the decrease in the dark matter mass at that time causes a larger relative decay in the Weyl potential and a corresponding increase in the amplitude of the acoustic peaks at the corresponding multipoles $\ell \gtrsim 700$. On the other hand, for modes that cross right around z_c, the change in the Weyl potential flips sign at the critical phase for driving the acoustic mode, leading to a local decrement in the power around $\ell \sim 500$.

As we can see from Fig. 4.2, these effects for variations of $\Delta c = \pm 0.02$ with other parameters fixed are too large to be accommodated by the data and must be compensated by other parameters. This can be done largely within the EDS sector itself, without sub-

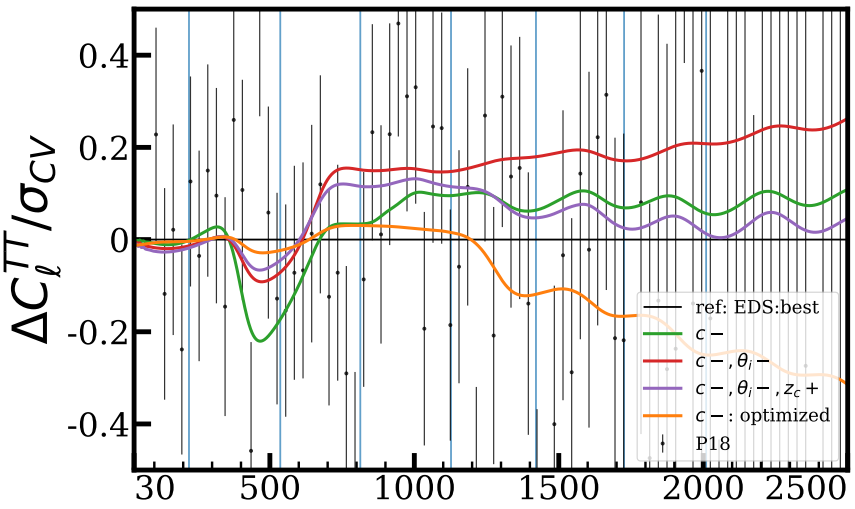

Figure 4.4: Comparison between the Planck TT data and both the global best-fit EDS model where $c = -0.005$ (black line) and the best model for the baseline data set with $c = -0.025$ fixed ($c-$ optimized, orange line). The other curves show the effect of varying the EDS parameters c, θ_i, and z_c from the former to the latter in the direction indicated by the $+$ and $-$ with the remaining parameters fixed to the global best-fit model.

stantially modifying the other ΛCDM parameters of Eq. (4.18), especially $\Omega_c h^2$. We study these compensating effects in Fig. 4.4, where we show TT power spectra for both the global best-fit EDS model where $c = -0.005$ (black line) and the best model with $c = -0.025$ fixed (orange line). We then iteratively perform the parameter shifts from the former to the latter so as to understand the compensations and hence the expected parameter degeneracies in the fit to data. One may appreciate from Fig. 4.4 that lowering c from $c = -0.005$ to $c = -0.025$ generates a significant dip in $C_\ell^{\rm TT}$ around $\ell \sim 500$. This can be compensated by lowering the initial phase θ_i, however this comes at the expense of significant residuals at somewhat higher multipoles. Next, tuning z_c changes the damping scale, and hence the high-ℓ amplitude. Therefore, we expect a $c - \theta_i - z_c$ degeneracy in the fit to data. This expectation is confirmed by MCMC analyses, e.g., Fig. 4.9, to be presented in Sec. 4.4.

In particular these compensations do not involve the *present* cold dark matter density $\Omega_c h^2$, leaving a range of allowed c at fixed $\Omega_c h^2$. Indeed in the best-fit model with $c = -0.005$, $\Omega_c h^2$ remains very close to its best-fit value for EDE (i.e. $c = 0$) but the change in

the dark matter mass makes the cold dark matter density at early times smaller. We shall see next that this delays the onset of the matter-dominated growth of density fluctuations and hence allows a smaller amplitude of structure today.

4.3.2 Growth of Structure

As we have seen, the CMB allows $c < 0$ with a present dark matter density $\Omega_c h^2$ nearly fixed. In this context, there are two distinct effects of c on the growth of structure and hence S_8 as can be seen in Fig. 4.5. The first is that for $c < 0$ the dark matter mass is lighter at $z > z_c$ and the dark matter density smaller. Therefore the start of the matter-dominated growth of density fluctuations is delayed, which leads to a smaller amplitude of fluctuations today for $c < 0$, all else equal. This can be seen in Fig. 4.5 as the negative change in density fluctuation right after z_c. Note that the behavior before z_c is due to the Weyl potential change induced by the change of the dark matter mass, as we see in Fig. 4.3. This pre-z_c effect will be suppressed for larger k modes where horizon crossing occurs much earlier. The second effect is that the ϕ field mediates an enhanced gravitational force for the dark matter, which increases the growth of structure for large values of $|c|$.

To understand this second effect, in App. A.2 we derive the equation of the dark matter density perturbation growth at second order in c, under a quasistatic approximation for the sourced scalar field perturbations, namely, the assumption that spatial gradients dominate over temporal derivatives for $\delta\phi$. This is a good approximation deep inside the horizon. In this limit, the impact of $\delta\rho_{\rm DM}$ on $\delta\phi$ takes the form of a non-oscillatory offset $\delta\phi^{(0)} \propto c\delta_c$ (see Eq. A.20). Substituting this back into the equation for δ_c, the resulting effect is an $\mathcal{O}(c^2)$ self-interaction. We find

$$\ddot{\delta}_c + \mathcal{H}\dot{\delta}_c = 4\pi G a^2 \rho_c \delta_c \left(1 + \frac{2c^2k^2}{k^2 + a^2 d^2V/d\phi^2}\right) , \tag{4.26}$$

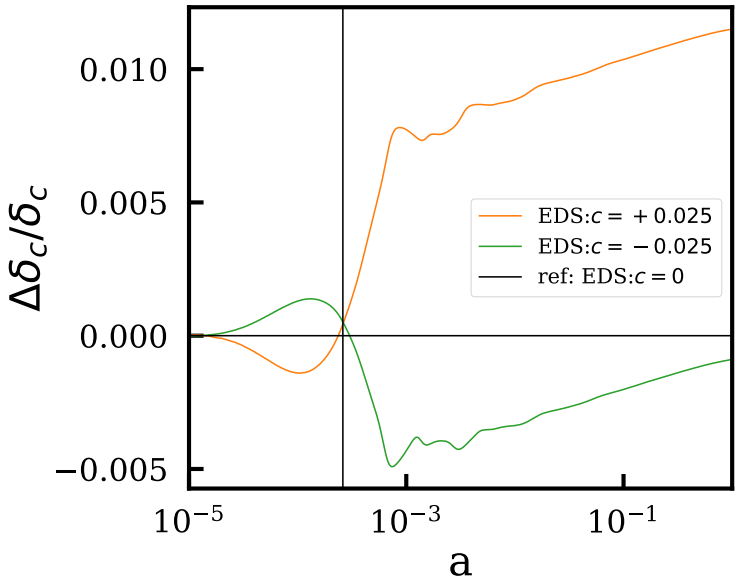

Figure 4.5: Density growth of EDS best-fit model as c varied, with fixed H_0 and all other parameters (except θ_s) fixed to their values in Eqs. (4.17) and (4.18). The vertical line indicates the location of z_c. Here $k = 0.2h\,\mathrm{Mpc}^{-1}$.

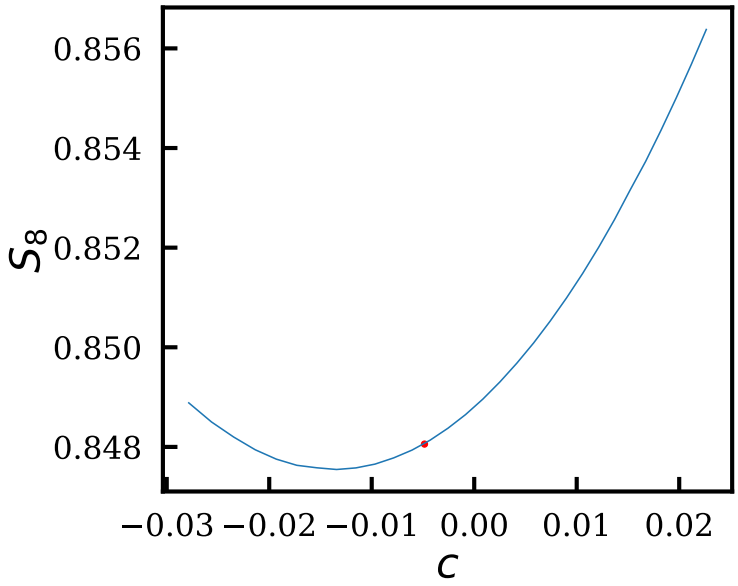

Figure 4.6: S_8 value as function of c, with fixed H_0 and all other parameters (except θ_s) fixed to their values in Eqs. (4.17) and (4.18). The red dot indicates the best-fit model.

where $\mathcal{H}$ is the Hubble parameter defined with respect to conformal time. From this one

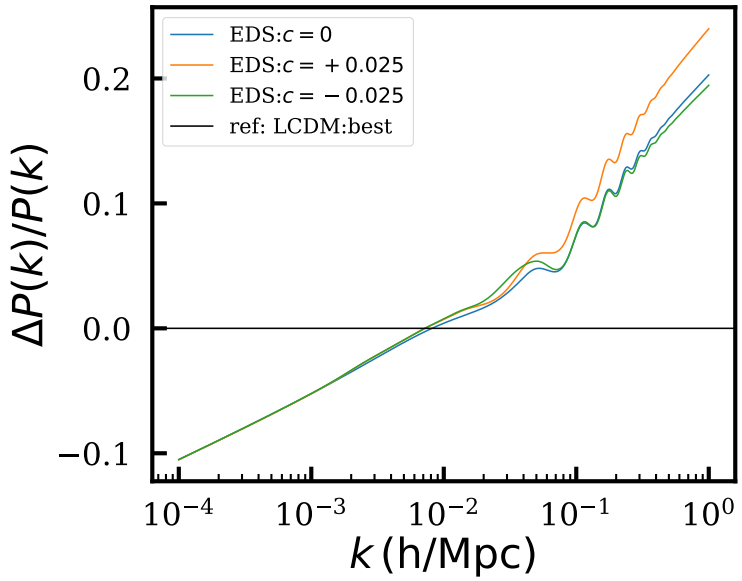

Figure 4.7: Matter power spectra of EDS best-fit model as c varied, with fixed H_0 and all other parameters (except θ_s) fixed to their values in Eqs. (4.17) and (4.18). The results are compared to the best-fit ΛCDM model.

may read off an effective gravitational constant,

$$G_{\rm eff} = G_N \left(1 + \frac{2c^2k^2}{k^2 + a^2 d^2V/d\phi^2}\right), \tag{4.27}$$

which is independent of the sign of c. This expression simplifies in the high-k limit, namely, for physical wavenumbers greater than the mass of the EDE scalar field, which satisfy,

$$\frac{k}{a} \gg m_\phi \equiv \sqrt{d^2V/d\phi^2}. \tag{4.28}$$

In this limit, we have,

$$G_{\rm eff} = G_N(1 + 2c^2), \tag{4.29}$$

which is independent of k and the scalar field potential. This enhanced gravitational constant can understood as a dark matter-philic scalar-mediated force.

The range of k-modes which satisfy Eq. (4.28) changes throughout cosmic history, as the

EDE scalar evolves. Before z_c, for the parameters in Eq. (4.17), the field mass is $|m_\phi| \simeq 3.9 \times 10^{-14}\,\mathrm{eV} \simeq 18\,h/\mathrm{Mpc}$. After z_c, the field is released from Hubble friction and begins to oscillate, and the mass rapidly decreases. After this, modes come to satisfy Eq. (4.28). The modes predominantly responsible for setting S_8, $k \approx 0.2\,h/\mathrm{Mpc}$, satisfy Eq. (4.28) shortly after z_c, while longer-wavelength modes begin to satisfy Eq. (4.28) at later times t_k as $a(t_k) \sim k^2$. The mass eventually settles to its value at the minimum of the effective potential and quasistatically evolves with ρ_{DM}. We derive in App. A.2 the scaling of this quasistatic mass with parameters and show that it remains negligible, even with the enhanced local ρ_{DM} of virialized structures. Consequently, even on nonlinear scales today, the scalar mediates an enhanced force on the dark matter.

A direct consequence of the enhanced gravitational constant in Eq. (4.29) is that both positive and negative c will increase the late-time growth of δ_c. This may be appreciated from Fig. 4.6, where we show S_8 as c is varied (with H_0 held fixed). While S_8 may be slightly decreased by a small negative c, making c further negative leads to a net increase in S_8. This may be understood analytically as follows. In the matter-dominated limit, the enhanced gravitational force on the dark matter, below the Compton scale $k \gg a m_\phi$, changes the growth rate to $\lim_{c \ll 1} \delta_c \propto a^{1+6c^2/5} \simeq a(1 + \log(a) 6c^2/5)$. This determines the fractional change in σ_8 as $\Delta\sigma_8/\sigma_8 \simeq \Delta\delta_c(z=0)/\delta_c \simeq -\log(a_{\mathrm{eq}}) 6c^2/5 \simeq 9.6c^2$. This simple estimate captures the qualitative behavior of S_8 in Fig. 4.6; more quantitatively we find $S_8 = 0.8488(1 + 0.22c + 7.93c^2)$.

These effects are encoded in the matter power spectrum by a c-dependent enhancement on small scales. The linear matter power spectrum for varying c is shown in Fig. 4.7, where one may appreciate a net enhancement for both positive and negative c. The enhancement is lessened in the negative c case, since the fifth force effect is mitigated by the delayed onset growth effect, while the opposite occurs for $c > 0$.

The imprint on the matter power spectrum is most significant on small scales. This is

true for both the imprint of the shift in matter-radiation equality (from the dark matter mass variation), and of the enhanced gravitational interaction. The latter effectively 'turns on' as modes come into the quasistatic approximation, and small-scale modes have had the greatest period of time spent under its influence. In our EDS model, these two competing effects leave only a small ability to lower S_8 with c. Interestingly though, these two effects are determined by different regions of the scalar field potential: the shift in $z_{\rm eq}$ is determined by the release from Hubble friction of the axion from the hilltop of the cosine potential, while the enhanced gravitational interaction is determined by the scalar field mass in the minimum of the potential. This opens the possibility of modifying the potential in such a way as to reduce the second effect and lower S_8 to below its ΛCDM value, e.g., if ϕ becomes heavy in the late universe. We leave the exploration of this possibility to future work.

4.4 Constraints from Data

In this work we take as our baseline data set the following combination:

1. **CMB**: *Planck* 2018 [127, 8, 128] low-ℓ and high-ℓ [`Plik`] temperature and polarization power spectra ($TT/TE/EE$), and reconstructed CMB lensing power spectrum.

2. **BAO**: distance measurements from the SDSS DR7 main galaxy sample [46], the 6dF galaxy survey [129], and SDSS BOSS DR12 [45], namely, the optimally combined LOWZ and CMASS galaxy samples.

3. **Supernovae**: The Pantheon supernovae data set [44], comprised of relative luminosity distances of 1048 SNe Ia in the redshift range $0.01 < z < 2.3$.

4. $\boldsymbol{H_0}$: The 2019 SH0ES cosmic distance ladder measurement $H_0 = 74.03 \pm 1.42\,\mathrm{km/s/Mpc}$ [15].[2]

2. We use the SH0ES 2019 measurement to facilitate comparison with previous work, but note that a more recent SH0ES measurement has recently appeared, with a smaller error

We supplement the above baseline data set with additional LSS data from the Dark Energy Survey Year-3 (DES-Y3) analysis [14]:

5. **DES-Y3**: Dark Energy Survey Year-3 [14] weak lensing and galaxy clustering data, namely, galaxy-galaxy, shear-shear, and galaxy-shear two-point correlation functions, implemented as a Gaussian constraint on $S_8 \equiv \sigma_8(\Omega_{\rm m}/0.3)^{0.5}$ corresponding to the DES-Y3 measurement $S_8 = 0.776 \pm 0.017$.

The approximation of DES data with an S_8 prior procedure was validated with DES-Y1 data in the context of EDE [2]. In this work, in light of the significant computational expense of evaluating the full DES 3×2pt likelihood, we assume that an S_8 prior continues to be a good approximation in the EDS model with DES-Y3 data. As we will see, the baseline data set combination restricts the EDS model to be a small departure from EDE, and thus one expects the validation test of [2] to apply, at least at the level of marginalized 1d and 2d posterior probability distributions.

Finally, we also supplement our baseline data set with CMB data from the Atacama Cosmology Telescope (ACT):

6. **ACT:** The ACT DR4 [130, 131] temperature and polarization power spectra. When combining these data with the *Planck* CMB likelihood, we apply the multipole cut determined in [130] to the ACT data to avoid double-counting information, in particular setting $\ell_{\rm min,TT} = 1800$.

The ACT collaboration analyzed the EDE model in [132] and found that ACT data combined with low-ℓ *Planck TT* data ($\ell < 650$, similar to *WMAP*) mildly prefer a non-zero $f_{\rm EDE}$ at $\approx 3\sigma$ significance (see also [135] and [4]). When combining ACT with the full *Planck* data set, this preference is no longer seen, due to the dominant statistical weight of *Planck* (which does not prefer EDE on its own). In our work we consider ACT in combination with the

bar and slightly lower value ($H_0 = 73.04 \pm 1.04\,{\rm km/s/Mpc}$) [7].

baseline data set, including *Planck* 2018. We take care in combining ACT and *Planck*, and in particular we apply a multipole cut $\ell_{\rm min,TT} = 1800$ to ACT data to avoid double counting information (following [130]). We additionally use increased precision settings in the theoretical computation of CMB power spectra when ACT is included in the joint data set, as emphasized in [130, 136].

We perform MCMC analyses of the EDS scenario using a modified version of CLASS ([137, 138])[3] and posterior sampling with `Cobaya` [139]. We impose broad uniform priors on the ΛCDM parameters. Following past work on Early Dark Energy (e.g., [2]), we impose uniform priors on the EDE parameters $f_{\rm EDE} = [0.001, 0.5]$ and $\log_{10}(z_c) = [3.1, 4.3]$, and a uniform prior on the initial field displacement in units of the decay constant f, as $\theta_i = [0.1, 3.1]$. The choice and impact of EDE priors is discussed in detail in [2]. Given that the EDE physics is sensitive primarily to θ_i (and not ϕ_i per se), and given that θ_i is itself relatively well-constrained by data [76, 2], we express $m_{\rm DM}(\phi)$ as $m_{\rm DM}(\theta) = m_0 e^{c_\theta \theta}$, with $c_\theta \equiv cf/M_{pl}$. We impose a uniform prior $c_\theta = [-0.08, 0.08]$. Since θ_i is fairly well constrained for cases that alleviate the Hubble tension, this allows c_θ to function as a proxy for $m_{\rm DM}$.

We follow the Planck convention for the neutrino masses, namely, we hold the sum of the neutrino masses fixed to 0.06eV with a single massive neutrino eigenstate. We analyze the MCMC chains using `GetDist` [140][4], and consider chains to be converged when the Gelman-Rubin statistic [141] satisfies $R - 1 < 0.05$. To determine maximum-likelihood parameter values we use the "BOBYQA" likelihood maximization method implemented in `Cobaya` [142, 143, 144]. When handling ACT data, we use increased `CLASS` precision settings as discussed in [130], and a slightly relaxed convergence criterion $R - 1 < 0.07$ due to the computational expense of these calculations. In all EDS runs, we use increased `CLASS` precision setting `perturb_sampling_stepsize` $= 0.02$.

3. http://class-code.net

4. https://github.com/cmbant/getdist

Constraints on the EDS scenario from Planck, BAO, SNIa, and SH0ES.

Model	ΛCDM	EDS	EDE
$\mathbf{100\theta_s}$	$1.04218\ (1.04205 \pm 0.00027)$	$1.04114\ (1.04136 \pm 0.00040)$	$1.04091\ (1.04141 \pm 0.00036)$
$\mathbf{\Omega_b h^2}$	$0.02249\ (0.02252 \pm 0.00013)$	$0.02284\ (0.02291 \pm 0.00024)$	$0.02286\ (0.02280^{+0.00020}_{-0.00022})$
$\mathbf{\Omega_c h^2}$	$0.11840\ (0.11821 \pm 0.00085)$	$0.1343\ (0.1288^{+0.0056}_{-0.0046})$	$0.1344\ (0.1296 \pm 0.0039)$
$\boldsymbol{\tau}$	$0.0594\ (0.0595^{+0.0068}_{-0.0078})$	$0.0600\ (0.0570 \pm 0.0075)$	$0.0600\ (0.0578 \pm 0.0072)$
$\mathbf{\log(10^{10} A_s)}$	$3.052\ (3.052 \pm 0.015)$	$3.079\ (3.062 \pm 0.017)$	$3.079\ (3.067 \pm 0.015)$
$\boldsymbol{n_s}$	$0.9686\ (0.9691 \pm 0.0035)$	$0.9931\ (0.9847 \pm 0.0073)$	$0.9930\ (0.9865 \pm 0.0071)$
$\boldsymbol{c_\theta}$		$-0.0010\ (-0.0024^{+0.0091}_{-0.015})$	
$\mathbf{f_{EDE}}$		$0.142\ (0.099^{+0.056}_{-0.041})$	$0.142\ (0.104^{+0.034}_{-0.030})$
$\mathbf{\log_{10} z_c}$		$3.58\ (3.602^{+0.071}_{-0.19})$	$3.58\ (3.606^{+0.037}_{-0.11})$
$\boldsymbol{\theta_i}$		$2.72\ (< 3.14)$	$2.73\ (2.60^{+0.31}_{+0.022})$
c		$-0.005\ (-0.011^{+0.029}_{-0.047})$	
$\phi_i\ [M_{\rm pl}]$		$0.547\ (0.53^{+0.10}_{-0.15})$	$0.549\ (0.48 \pm 0.11)$
$\log_{10}(f/{\rm eV})$		$26.69\ (26.857^{+0.058}_{-0.37})$	$26.69\ (26.652^{+0.080}_{-0.14})$
$\log_{10}(m/{\rm eV})$		$-27.27\ (-27.04^{+0.30}_{-0.55})$	$-27.28\ (-27.195^{+0.031}_{-0.23})$
$\Delta m_{\rm DM}/m_{\rm DM}$		$-0.003\ (-0.007 \pm 0.021)$	
σ_8	$0.8093\ (0.8087 \pm 0.0060)$	$0.8481\ (0.838^{+0.011}_{-0.013})$	$0.8490\ (0.815 \pm 0.011)$
Ω_m	$0.3047\ (0.3039 \pm 0.0050)$	$0.3000\ (0.3012 \pm 0.0056)$	$0.3003\ (0.3017 \pm 0.0051)$
S_8	$0.8156\ (0.8140 \pm 0.0098)$	$0.8481\ (0.840 \pm 0.014)$	$0.8495\ (0.838 \pm 0.013)$
H_0	$68.16\ (68.21 \pm 0.39)$	$72.52\ (71.1 \pm 1.2)$	$72.50\ (71.2 \pm 1.1)$
$\Delta\chi^2_{\rm tot}$	0	-18.1	-16.2

Table 4.1: Maximum-likelihood (ML) parameters and 68% CL marginalized constraints for the ΛCDM, EDS, and EDE models, in the fit to a combined data set comprised of Planck 2018 CMB, CMB lensing, BAO, SNIa, and SH0ES. Parameters in bold are sampled in the MCMC analyses.

4.4.1 EDS vs EDE: The Interplay of H_0 and S_8

We first perform a direct comparison of the EDE and EDS models fit to the baseline data set, namely, *Planck* 2018 primary CMB anisotropies, *Planck* 2018 CMB lensing, BAO, Pantheon, and SH0ES. The posteriors are shown in Figs. 4.8 and 4.9, the best-fit parameters and parameter constraints are given in Tab. 4.1, and the χ^2 statistics of the best-fit models are given in Tab. 4.2.

The best-fit EDS and EDE models (Tab. 4.1) have near-identical cosmological parameters. They are distinguished primarily by the parameter c, which is $c = -5 \times 10^{-3}$ in EDS, while $c = 0$ in EDE by definition. The models have near identical best-fit H_0 and S_8, with $H_0 = 72.50$ km/s/Mpc and 72.52 km/s/Mpc, and $S_8 = 0.8481$ and 0.8495, for EDS and EDE respectively. Both models are a significant χ^2 reduction in comparison to the best-fit

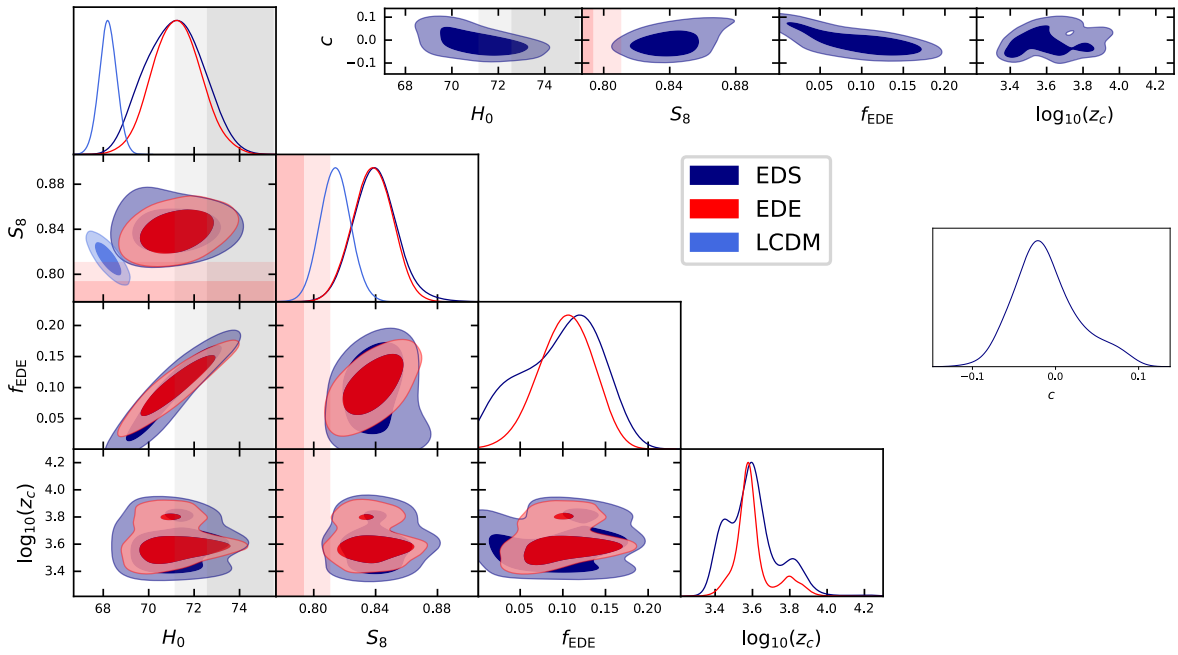

Figure 4.8: Interplay of the H_0 and S_8 tensions in the EDS, EDE, and ΛCDM models (as labeled). The plot shows posterior distributions for the fit to the baseline data set (CMB, CMB lensing, BAO, SNIa, and SH0ES). Shaded grey and pink bands denote the SH0ES measurement and the DES-Y3 S_8 constraint, respectively.

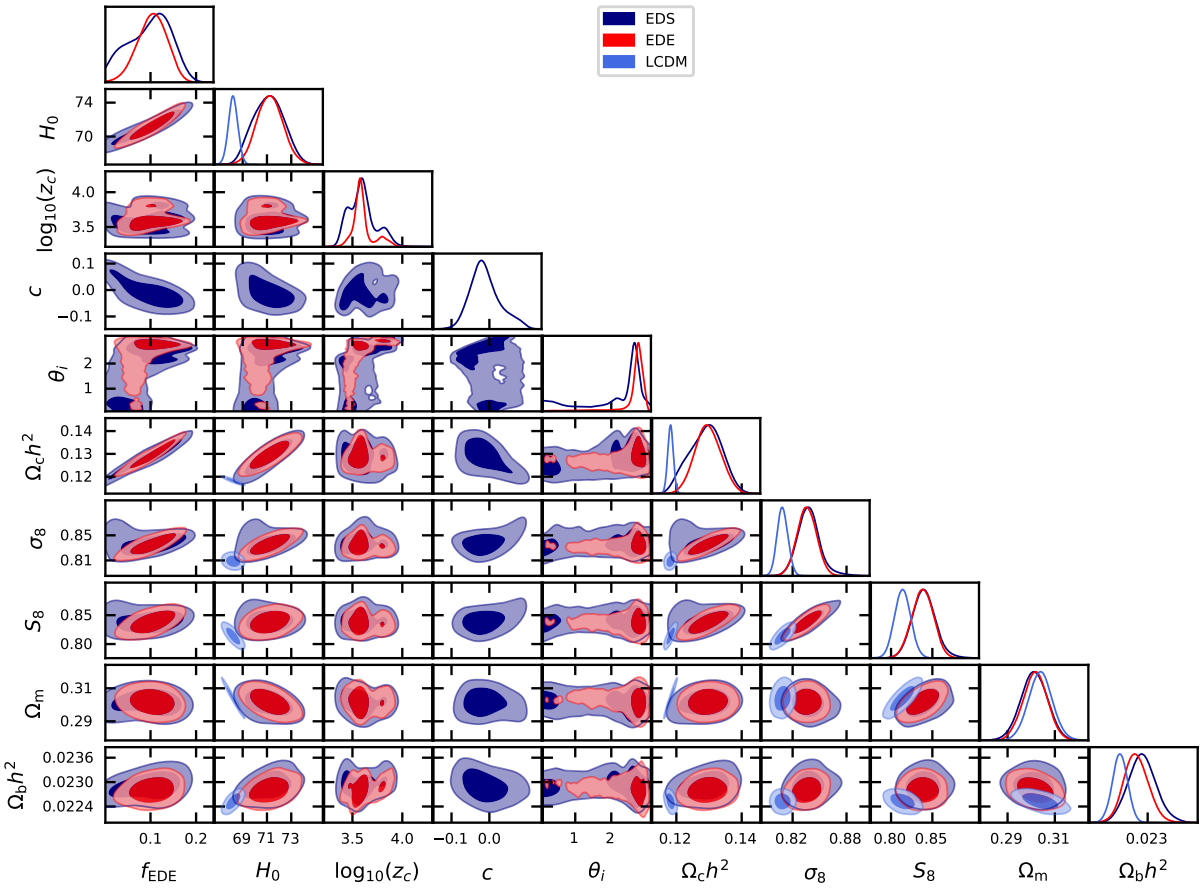

Figure 4.9: Enlarged set of posterior distributions for the fit to the baseline data set (CMB, CMB lensing, BAO, SNIa, and SH0ES) for ΛCDM, EDE, and EDS.

EDS χ^2 statistics
from the fit to *Planck* 2018, BAO, SNIa, SH0ES

Datasets	ΛCDM	EDS	EDE
Primary CMB:			
Planck 2018 low-ℓ TT	22.9	20.9	20.9
Planck 2018 low-ℓ EE	397.2	397.2	397.2
Planck 2018 high-ℓ TT+TE+EE	2346.5	2345.1	2346.9
LSS:			
Planck CMB lensing	8.9	10.0	10.0
BAO (6dF)	0.00005	0.008	0.005
BAO (DR7 MGS)	1.7	2.0	2.0
BAO (DR12 BOSS)	3.4	3.4	3.5
SNIa (Pantheon)	1034.8	1034.7	1034.7
SH0ES	17.2	1.2	1.2
Planck prior	1.9	2.2	2.2
$\Delta\chi^2_{\text{Primary CMB}}$	0	-3.4	-1.6
$\Delta\chi^2_{\text{LSS}}$	0	$+1.4$	$+1.5$
$\Delta\chi^2_{\text{SH0ES}}$	0	-16.0	-16.0
$\Delta\chi^2_{\text{tot}}$	0	-18.1	-16.2

Table 4.2: χ^2 statistics for the ML ΛCDM, EDS, and EDE models in the fit to the baseline data set (CMB, CMB lensing, BAO, SNIa, and SH0ES).

ΛCDM, while the EDS model, with $c = -5 \times 10^{-3}$, is a slightly better fit to the data than EDE, with a relative χ^2 reduction of $\Delta\chi^2_{\text{EDS}-\text{EDE}} = -1.9$. This is driven by the high-ℓ CMB data, which in turn drives the mild preference for $c < 0$, as discussed in Sec. 4.3.

The marginalized posterior distributions, shown in Fig. 4.8, shed more light on the differences between the models. From the $H_0 - S_8$ panel of Fig. 4.8, one may appreciate that the tight $H_0 - S_8$ correlation in EDE is softened in EDS, evidenced by an overall flattening of the 1σ posterior, and a slight anti-correlation of H_0 and S_8 in the 95% contour. Focusing on the SH0ES 1σ region, indicated by the dark grey band, we see that the EDS model allows a notable reduction in S_8 relative to EDE. This suggests that, in the high-H_0 context, the EDS model may allow greater compatibility with current LSS data, e.g., from the Dark Energy Survey, than the EDE model. We return to this point in Sec. 4.4.2.

The ability to raise H_0 and simultaneously lower S_8 in EDS relative to EDE is obscured in the 1d marginalized posteriors and the marginalized parameter constraints. This occurs due to the low-H_0 region of parameter space, $H_0 \lesssim 70$ km/s/Mpc, where the 95% CL contour in EDS extends to significantly larger S_8 values than in EDE. The net effect, i.e., after marginalizing, is for the 1d S_8 posterior in EDS to be near-identical to that in EDE, differing only in the high-S_8 tail.

EDS χ^2 statistics
from the fit to *Planck* 2018, BAO, SNIa, SH0ES, and S_8 from DES-Y3

Datasets	ΛCDM	EDS	EDE
Primary CMB:			
Planck 2018 low-ℓ TT	22.4	21.0	20.9
Planck 2018 low-ℓ EE	396.1	396.7	396.6
Planck 2018 high-ℓ TT+TE+EE	2349.6	2344.7	2345.5
LSS:			
Planck CMB lensing	9.9	9.9	9.9
BAO (6dF)	0.011	0.085	0.078
BAO (DR7 MGS)	2.1	2.7	2.6
BAO (DR12 BOSS)	3.4	4.0	4.0
S_8 (DES-Y3)	2.5	6.5	7.6
SNIa (Pantheon)	1034.7	1034.8	1034.8
SH0ES	15.4	2.2	2.0
Planck prior	1.9	1.6	2.0
$\Delta\chi^2_{\text{Primary CMB}}$	0	-5.7	-5.1
$\Delta\chi^2_{\text{LSS}}$	0	+5.3	+6.3
$\Delta\chi^2_{\text{SH0ES}}$	0	-13.2	-13.3
$\Delta\chi^2_{\text{tot}}$	0	-13.9	-11.9

Table 4.3: χ^2 values for the ML ΛCDM, EDS, and EDE models in the fit to *Planck* primary CMB and CMB lensing, BAO, SNIa, SH0ES, and S_8 from DES-Y3.

These two corners of parameter space, i.e., high-H_0-low-S_8 and low-H_0-high-S_8, correlate with the EDS parameter c. This can be appreciated from the $c - H_0$ and $c - S_8$ panels in Fig. 4.8, where one may see that high-H_0-low-S_8 correlates with $c < 0$, while low-H_0-high-S_8 correlates with $c > 0$. This suggests that additional S_8 data would prefer $c < 0$; we return to this in Sec. 4.4.2. There is an additional effect at $c < 0$, which amplifies the overall preference

Constraints on the EDS scenario from *Planck* 2018, BAO, SNIa, SH0ES, and S_8 from DES-Y3.

Model	ΛCDM	EDS	EDE
$\mathbf{100\theta_s}$	1.04202 (1.04208 ± 0.00027)	1.04143 (1.04151 ± 0.00039)	1.04138
$\mathbf{\Omega_b h^2}$	0.02258 (0.02258 ± 0.00013)	0.02273 (0.02287 ± 0.00022)	0.02281
$\mathbf{\Omega_c h^2}$	0.11760 (0.11754 ± 0.00078)	0.1284 ($0.1247^{+0.0042}_{-0.0047}$)	0.1287
$\boldsymbol{\tau}$	0.0535 (0.0577 ± 0.0071)	0.0583 (0.0557 ± 0.0074)	0.0581
$\mathbf{\log(10^{10} A_s)}$	3.041 (3.046 ± 0.014)	3.063 (3.051 ± 0.015)	3.065
$\boldsymbol{n_s}$	0.9706 (0.9704 ± 0.0035)	0.9884 (0.9812 ± 0.0072)	0.9895
$\boldsymbol{c_\theta}$		-0.0034 ($-0.0044^{+0.0076}_{-0.0097}$)	
$\boldsymbol{f_{\rm EDE}}$		0.112 (< 0.140)	0.109
$\mathbf{\log_{10} z_c}$		3.57 (> 3.39)	3.56
$\boldsymbol{\theta_i}$		2.69 (< 2.84)	2.77
c		-0.020 ($-0.020^{+0.025}_{-0.032}$)	
$\phi_i\,[M_{\rm pl}]$		0.461 (0.46 ± 0.12)	0.463
$\log_{10}(f/{\rm eV})$		26.62 ($26.835^{+0.057}_{-0.43}$)	26.61
$\log_{10}(m/{\rm eV})$		-27.29 ($-26.90^{+0.21}_{-0.63}$)	-27.31
$\Delta m_{\rm DM}/m_{\rm DM}$		-0.0009 (-0.0095 ± 0.014)	
σ_8	0.8024 (0.8044 ± 0.0054)	0.8287 (0.8206 ± 0.0096)	0.8320
Ω_m	0.3004 (0.2999 ± 0.0046)	0.2931 (0.2961 ± 0.0052)	0.2934
S_8	0.8028 (0.8043 ± 0.0084)	0.8192 (0.815 ± 0.010)	0.8228
H_0	68.47 (68.51 ± 0.36)	71.96 (70.7 ± 1.2)	72.02
$\Delta\chi^2_{\rm tot}$	0	-13.9	-11.9

Table 4.4: ML parameters and marginalized parameter constraints for ΛCDM and EDS in the fit to a combined data set comprised of *Planck* 2018 primary CMB and CMB lensing, BAO, SNIa, SH0ES, and S_8 data from DES-Y3. Parameters in bold are sampled in the MCMC analyses. For EDE we present the ML parameters, but not marginalized parameter constraints, as we do not repeat the MCMC for EDE (see [2] for analysis of a similar data set combination in EDE). Upper and lower bounds are quoted at 95% CL.

of the baseline data set for $c < 0$: the negative c region includes a weak multimodality in $\log_{10}(z_c)$, and in particular at $\log_{10}(z_c) \simeq 3.8$ the 1σ contour is contained completely within $c < 0$. These effects combine to give an overall mild asymmetry in the posterior, weighted toward $c < 0$, and we find $c = -0.011^{+0.029}_{-0.047}$.

4.4.2 Impact of Dark Energy Survey data

We now supplement the baseline data set with DES-Y3 data [14], approximated by a Gaussian constraint on $S_8 \equiv \sigma_8(\Omega_{\rm m}/0.3)^{0.5}$ corresponding to the DES-Y3 measurement $S_8 = 0.776 \pm 0.017$. To contextualize these results, we perform the same analysis for ΛCDM. We do not repeat the baseline+DES-Y3 analysis for EDE, in light of computational expense and given that the role of S_8 data in EDE was studied in detail in [2].

The best-fit parameters and parameter constraints are given in Tab. 4.4 and the χ^2 statistics are given in Tab. 4.3. Consistent with expectations from the fit to the baseline data set, Sec. 4.4.1, we find that when DES-Y3 is included the best-fit EDS has a lower S_8 than EDE, whilst having a near-identical value of H_0. We find $S_8 = 0.8192$ and $S_8 = 0.8228$ in EDS and EDE respectively, corresponding to a $\Delta\chi^2_{\rm DES-Y3} = -1.1$ between the two models. Meanwhile the H_0 values are respectively 71.96 km/s/Mpc and 72.02 km/s/Mpc for the two models, corresponding to $\Delta\chi^2_{\rm SH0ES} = +0.1$. Comparing the total χ^2, Tab. 4.3, we find that the best-fit EDS is an improvement over EDE of $\Delta\chi^2_{\rm EDS-EDE} = -2.0$.

The marginalized posterior distributions are shown in Figs. 4.10 and A.2. The preference for $f_{\rm EDE} > 0$ is significantly diminished when DES-Y3 is included (as expected based on previous work for EDE [2, 84, 85]), and in place of a detection we find only an upper bound. We find a 95% CL upper bound $f_{\rm EDE} < 0.14$, which, while consistent with the H_0-resolving regime of parameter space, is also consistent with $f_{\rm EDE} = 0$, similar to results in the non-interacting EDE scenario [2] when DES-Y1, HSC, and KV-450, are included. However, one may appreciate from the $H_0 - S_8$ panel that EDS exhibits a substantial overlap between the 95% CL contours of both the SH0ES measurement (grey bands) and DES-Y3 measurement (pink bands). This indicates that the EDS model fit to baseline+DES-Y3 data is statistically consistent with both SH0ES and DES-Y3, at 95% CL. This is encoded in the marginalized parameter constraints by a broadening of the error bars in EDS relative to EDE: comparing to Tab. VIII of [2], we see that the error bar on H_0 in the EDE fit to a comparable combination

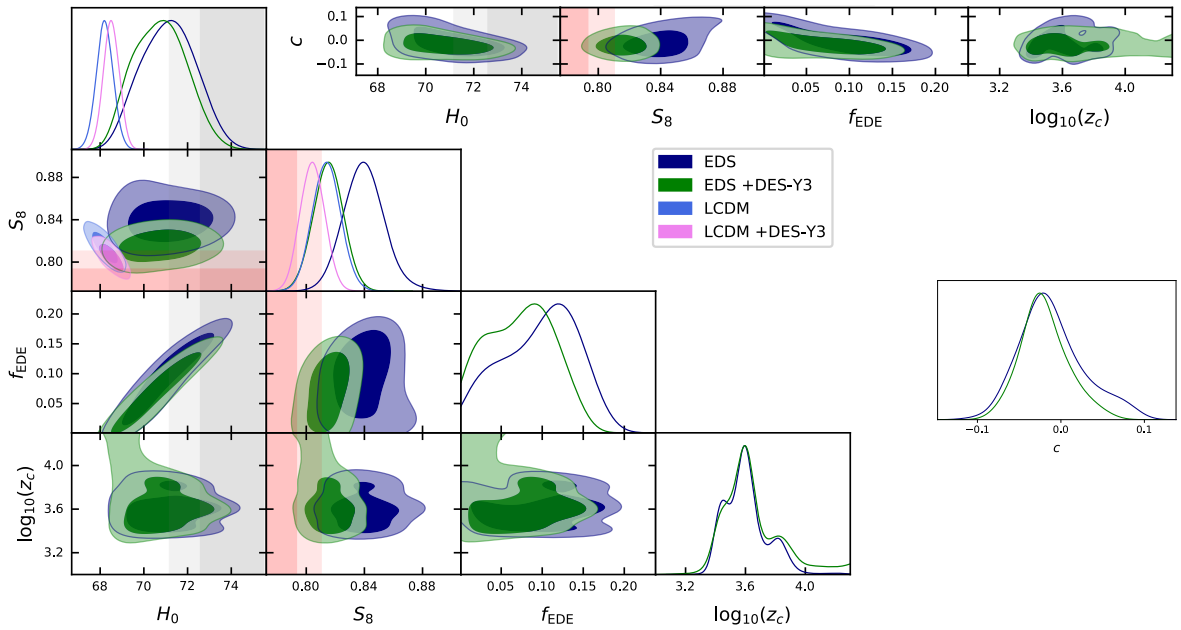

Figure 4.10: The impact of S_8 data. The plot shows posterior distributions for the fit to the baseline data set (CMB, CMB lensing, BAO, SNIa, and SH0ES) supplemented with DES-Y3 data, approximated by a prior on S_8, for ΛCDM, EDE, and EDS. Shaded grey and pink bands denote the 2019 SH0ES measurement and the DES-Y3 S_8 constraint, respectively.

of data sets is $\approx \pm 1.1$, whereas in our analysis we find an error bar ± 1.2.

The weighting of the posterior to $c < 0$ is slightly strengthened by the inclusion of DES-Y3 data, as the additional S_8 data disfavors the low-H_0-high-S_8 region discussed in Sec. 4.4.1. We find $c = -0.020^{+0.025}_{-0.032}$ and highlight the 1d c posterior in Fig. 4.10, where the support for the $c > 0$ tail of the distribution present in the fit to the baseline data set has been significantly reduced. Looking at the the $c - \log_{10}(z_c)$ panel, we again see a weak multimodality, now accompanied by a tail out to large z_c.

4.4.3 Constraints from ACT Data

Finally, we consider the impact of high-precision small-scale CMB data, namely, the latest measurements from the Atacama Cosmology Telescope fourth data release (DR4) [131, 130]. The ACT collaboration analysis of EDE [132], in a fit to the combination of ACT, large-scale

Planck TT, Planck CMB lensing, and BAO data, has found a moderate $\approx 3\sigma$ preference for a non-zero EDE component, finding $f_{\rm EDE} = 0.091^{+0.020}_{-0.036}$. As a first look at ACT and the EDS model, we supplement our baseline data set with ACT TT, TE, and EE data. We include the full Planck likelihood, including the high-ℓ temperature and polarization power spectra, and impose the multipole cut determined in [130] to the ACT data to avoid double-counting information, in particular setting $\ell_{\rm min,TT,ACT} = 1800$.

When using the ACT data we use enhanced precision settings in our modified version of the Boltzmann code `CLASS`. The need for this increased precision is documented in [130] (see their Appendix A). This increased precision comes at the cost of additional computational expense in the MCMC analyses. In light of this, and in light of the existing ACT collaboration analyses of ΛCDM [130] and EDE [132], in this work we perform an MCMC analysis of only the EDS model (and not EDE or ΛCDM), and we present maximum-likelihood parameters for only EDS and ΛCDM (and not EDE). Future optimization of the precision parameters needed for these calculations, and/or the development of emulators with which to accelerate the Boltzmann code (e.g., as in [145]), will be useful.

The best-fit parameters and parameter constraints for the analysis including ACT are given in Tab. 4.5, and χ^2 statistics are given in Tab. 4.6. The marginalized posterior distributions are shown in Fig. 4.11.

Inclusion of the ACT data provides a factor of two improvement on the error on c. We find $c = -0.002^{+0.015}_{-0.024}$ in comparison with $c = -0.011^{+0.029}_{-0.047}$ from the fit to the baseline data set. This dramatic reduction is largely driven by the ability of ACT to constrain the timing of the EDE component, z_c. Indeed, from the posterior distribution of $\log_{10}(z_c)$ in Fig. 4.11, one may appreciate that the inclusion of ACT data in the EDS analysis almost completely removes the multimodality exhibited in the fit of EDS to the baseline data set, as ACT removes the high-z_c tail (as discussed in [132]). The reduced multimodality in z_c propagates to the marginalized constraint on c, leading to an overall reduction in the error

bar.

Meanwhile, the preference for a non-zero EDE component is strengthened (as found in [132, 135, 146]): we find the marginalized constraint $f_{\rm EDE} = 0.108^{+0.053}_{-0.023}$ when ACT is included, compared to $f_{\rm EDE} = 0.099^{+0.056}_{-0.041}$ without ACT data. However, the $f_{\rm EDE}$ posterior distribution in Fig. 4.11 is significantly broader than a Gaussian, exhibiting ample support on the boundary of the prior at $f_{\rm EDE} \approx 0$. Indeed we find the 95% CL constraint $f_{\rm EDE} = 0.108^{+0.063}_{-0.095}$, which nearly reaches $f_{\rm EDE} = 0$. This is reflected also in the 2d posteriors, e.g., $f_{\rm EDE} - H_0$ and $f_{\rm EDE} - S_8$, which are consistent with $f_{\rm EDE} = 0$ at the 95% confidence level. The marginalized constraints on H_0 and S_8 are consistent with those from the fit to the baseline data set, while the best-fit values of both are lower when ACT is included, with $H_0 = 71.79$ and $H_0 = 72.52$ with and without ACT respectively, and $S_8 = 0.8385$ and $S_8 = 0.8481$ with and without ACT, respectively.

Turning to the χ^2 values, Tab. 4.6, we find that the best-fit EDS model is an improvement over the best-fit ΛCDM model by $\Delta\chi^2 = -19.0$. This is slightly enhanced relative to that in the fit to the baseline data set ($\Delta\chi^2_{\rm tot,\,baseline} = -18$, Tab. 4.2), driven in part by $\Delta\chi^2_{\rm ACT} = -1.9$, consistent with the mild preference of ACT data for a non-zero EDE component.

4.4.4 The Swampland

As discussed in Sec. 4.2, the SDC states that a Planckian field excursion leads to an exponential suppression of the mass of other fields. The simple setup studied here, with the scalar field coupled to all of the dark matter, provides a minimal context within which to test the SDC. A similar idea has been explored previously in the context of quintessence, where it was dubbed Fading Dark Matter [124].

The 95% bounds on the parameter c are given in Tab. 4.7. The posterior distributions for swampland-related quantities (the field excursion, the axion decay constant, and the coupling

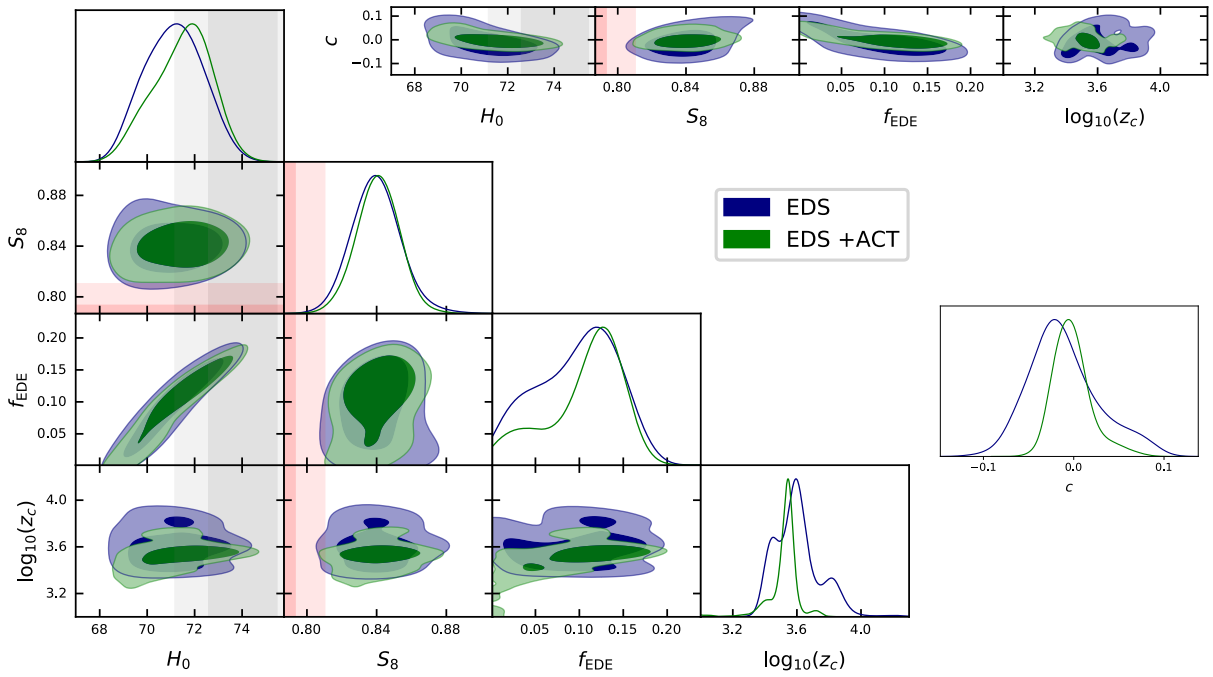

Figure 4.11: Constraints including ACT data. The plot shows posterior distributions for the fit of the EDS model to the baseline data set (CMB, CMB lensing BAO, SNIa, and SH0ES) with and without the addition of ACT primary CMB data. Shaded grey and pink bands denote the SH0ES measurement and the DES-Y3 S_8 constraint, respectively.

Maximum Likelihood and Marginalized Parameter Constraints from the combination of the baseline data set and ACT data.

Parameter	ΛCDM	EDS
$\mathbf{100\theta_s}$	1.04219	$1.04150\ (1.04151^{+0.00034}_{-0.00039})$
$\boldsymbol{\Omega_b h^2}$	0.02248	$0.02257\ (0.02258 \pm 0.00017)$
$\boldsymbol{\Omega_c h^2}$	0.1181	$0.1311\ (0.1302^{+0.0055}_{-0.0034})$
$\boldsymbol{\tau}$	0.0599	$0.0565\ (0.0546 \pm 0.0071)$
$\mathbf{log(10^{10} A_s)}$	3.059	$3.071\ (3.068 \pm 0.015)$
$\boldsymbol{n_s}$	0.9725	$0.9876\ (0.9865^{+0.0077}_{-0.0065})$
$\boldsymbol{c_\theta}$		$-0.0008\ (0.0013^{+0.0013}_{-0.0065})$
$\boldsymbol{f_{\rm EDE}}$		$0.119\ (0.108^{+0.053}_{-0.023})$
$\mathbf{log_{10} z_c}$		$3.545\ (3.521^{+0.071}_{-0.032})$
$\boldsymbol{\theta_i}$		$2.79\ (2.44^{+0.46}_{+0.16})$
c		$-0.005\ (-0.002^{+0.015}_{-0.024})$
$\phi_i\,[M_{\rm pl}]$		$0.474\ (0.490 \pm 0.093)$
$\log_{10}(f/{\rm eV})$		$26.61\ (26.726^{+0.011}_{-0.19})$
$\log_{10}(m/{\rm eV})$		$-27.32\ (-27.270^{+0.033}_{-0.16})$
$\Delta m_{\rm DM}/m_{\rm DM}$		$-0.0009\ (-0.0011^{+0.0078}_{-0.011})$
σ_8	0.8128	$0.8393\ (0.840^{+0.010}_{-0.0094})$
Ω_m	0.3003	$0.2995\ (0.3003 \pm 0.0052)$
S_8	0.8172	$0.8385\ (0.841 \pm 0.012)$
H_0	68.23	$71.79\ (71.5^{+1.4}_{-1.1})$
$\Delta\chi^2_{\rm tot}$	0	-19.0

Table 4.5: Maximum likelihood (ML) parameters and marginalized parameter constraints for EDS and ΛCDM in the fit including ACT data. Parameters in bold are sampled in MCMC analyses. For ΛCDM we give only ML parameters, due to the significant computational expense of MCMC analyses at the high precision settings required to analyse ACT data.

c), along with their correlations with the Hubble parameter H_0, are shown in Fig. 4.12. The SH0ES measurement is shown in grey bands. From this one may appreciate that the EDE resolution of the Hubble tension scenario, namely, the ability for the EDE model to be $1-2\sigma$ consistent with SH0ES, indeed rests upon a Planckian field excursion $|\Delta\phi|/M_{\rm pl} \simeq 1/2$, and a Planckian axion decay constant $f \sim M_{\rm pl}/5$. Thus one naturally expects the parameter c to play a role in this model.

However, turning to Tab. 4.7, we see that the SDC parameter c is constrained to be $c < 0.068$ from the baseline data set, at 95% CL, and $c < 0.035$ and $c < 0.042$ at 95% CL

χ^2 statistics
from the fit to *Planck* 2018, BAO, SNIa, SH0ES, and ACT

Datasets	ΛCDM	EDS
Primary CMB:		
Planck 2018 low-ℓ TT	22.2	21.3
Planck 2018 low-ℓ EE	397.2	396.4
Planck 2018 high-ℓ TT+TE+EE	2346.3	2345.9
ACT	243.2	241.2
LSS:		
Planck CMB lensing	8.4	9.8
BAO (6dF)	0.0008	0.015
BAO (DR7 MGS)	1.8	2.1
BAO (DR12 BOSS)	3.4	3.4
SNIa (Pantheon)	1034.7	1034.7
SH0ES	16.7	2.5
Planck prior	4.1	2.0
$\Delta\chi^2_{\textit{Planck}\text{ primary CMB}}$	0	-2.1
$\Delta\chi^2_{\text{ACT}}$	0	-1.9
$\Delta\chi^2_{\text{LSS}}$	0	$+1.2$
$\Delta\chi^2_{\text{SH0ES}}$	0	-14.2
$\Delta\chi^2_{\text{tot}}$	0	-19.1

Table 4.6: χ^2 statistics for the ML ΛCDM and EDS models in the fit to the baseline data set (CMB, BAO, SNIa, and SH0ES) supplemented with ACT data.

when DES-Y3 or ACT are included, respectively. From this we infer a mild tension of the data, in the context of the EDE model, with the SDC at the level of a $4-7\%$ fine-tuning.

While the degree of fine tuning may not be severe, it is interesting to note that these constraints are an order of magnitude stronger than constraints on other would-be $\mathcal{O}(1)$ swampland parameters. In particular, the de Sitter (dS) Swampland Conjecture [147] states that scalar field potentials cannot be arbitrarily flat, and are bounded by $V'/V \geq \mathcal{O}(1)$ in Planck units. The would-be $\mathcal{O}(1)$ parameter of the dS conjecture is constrained by data to be $V'/V \lesssim 0.51$ (2σ) [148] or $V'/V \lesssim 1.35$ (3σ) [149] (see also [150]). Compared to the constraints on SDC order-1 parameter presented in this work ($c < 0.035$, $c < 0.042$, and $c < 0.068$ at 95% CL), one may appreciate the latter are considerably stronger than

constraints on the swampland found in previous works.

Finally, we note that a more complete analysis, which we will not pursue here, would be to allow variation in the fraction of dark matter $f_{\rm DM}$ to which the scalar field couples. This would introduce one new parameter to the already four-parameter EDS extension to ΛCDM. We expect the $\approx 5\%$ fine-tuning of c in our fixed-$f_{\rm DM}$ analysis to translate to slightly lesser fine-tunings of c and $f_{\rm DM}$ once $f_{\rm DM}$ is allowed to vary.

Constraints on the Swampland Distance Conjecture

Datasets	95% upper limit on c
baseline	$c < 0.068$
baseline + S_8 from DES-Y3	$c < 0.035$
baseline + ACT	$c < 0.042$

Table 4.7: Constraints on the Swampland Distance Conjecture parameter c, defined by the early dark energy dependence of the dark matter mass $m_{\rm DM} = e^{c\phi/M_{\rm pl}}$. Upper and lower bounds are 95% CL.

4.5 Discussion

In this work have extended Early Dark Energy to an Early Dark *Sector* (EDS). Motivated by the Swampland Distance Conjecture [90] (SDC), the EDS is comprised of the EDE scalar field along with a dark matter candidate whose mass is exponentially sensitive to Planckian field excursions of the EDE scalar. The aims of this model are two-fold: (1) to understand the interplay of the H_0 and S_8 tensions, and determine whether the competition between these can be softened by embedding EDE into a larger model, and (2) to determine the extent to which EDE (namely the H_0-tension-resolving region of EDE parameter space) is in conflict with the SDC, and thereby determine whether the EDE resolution of the Hubble tension lies in the landscape or the swampland.

Concretely, the EDS model is a one-parameter extension of EDE, parameterized by an additional parameter c corresponding to the exponent in the dark matter mass, $m_{\rm DM}(\phi) = m_0 e^{c\phi/M_{\rm pl}}$, where ϕ is the EDE scalar. In our sign convention, where ϕ is initially > 0 and

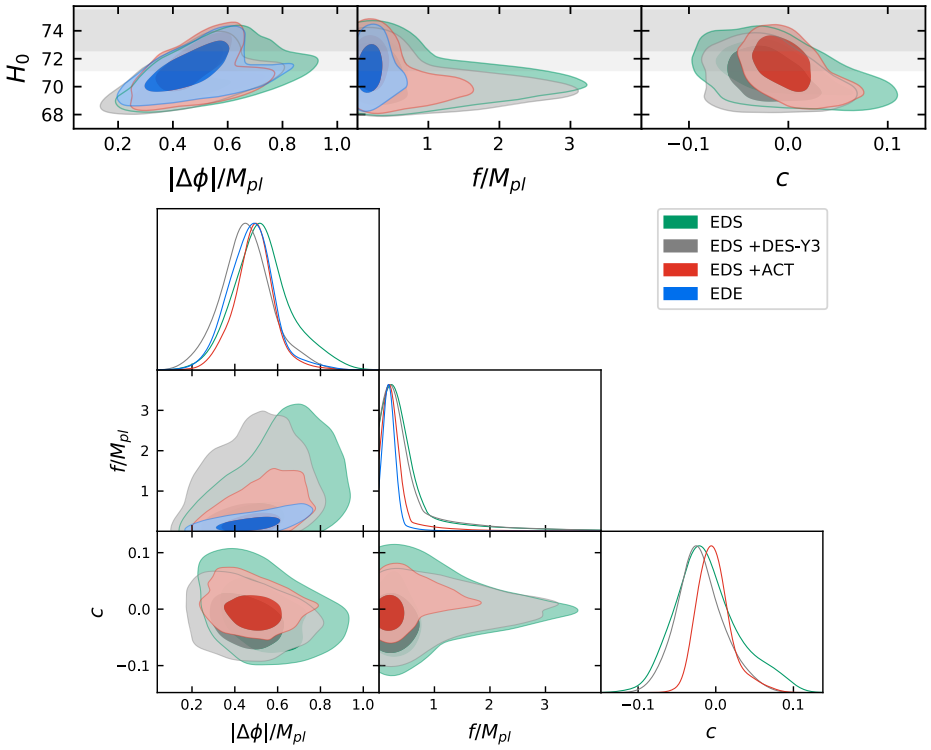

Figure 4.12: Early Dark Energy and the swampland conjectures. We show the posterior distributions of the field excursion, axion decay constant, and dark matter mass dependence, along with their correlation with H_0, in the fit to varying data sets. The swampland distance conjecture would suggest that $c = \mathcal{O}(1) > 0$, while the data constrain $c < 0.068$, 0.035, and 0.042 at 95% confidence, for the baseline data set, the baseline + DES-Y3, and baseline + ACT, respectively, and slightly prefer $c < 0$.

decreases over cosmic evolution, the SDC predicts that $c > 0$ and $c = \mathcal{O}(1)$. The parameter c has important impacts on both the CMB and on the growth of structure. In the CMB the imprint of c contains a localized feature around $\ell \simeq 500$, corresponding to modes that enter the horizon near z_c and a sign reversal in its effect at much higher multipoles. This can be understood in terms of the impact of the dark matter mass on the radiation driving of acoustic oscillations, as described in Sec. 4.3.

Meanwhile, $c > 0$ (at fixed $\Omega_c h^2$) leads to an enhanced growth of structure, due to the relative shift in matter radiation equality to earlier times. The growth of structure is also subject to a second effect: an effective dark matter self-interaction (a dark "fifth force") that is attractive, and in the limit of high k has strength $c^2 G_N$. This leads to enhanced structure formation on small scales for both positive and negative c. The combination of the two growth effects allows a small but negative c to decrease S_8. Incidentally, this small negative c also improves the fit to the CMB.

Armed with the theory motivation and understanding of the phenomenology, we have performed MCMC analyses of the EDS model fit to a baseline data set combination of *Planck* 2018 primary CMB and CMB lensing [127, 8, 128]; BAO from the SDSS DR7 main galaxy sample [46], the 6dF galaxy survey [129], and SDSS BOSS DR12 [45]; the Pantheon supernovae data set [44], and the 2019 SH0ES H_0 measurement [15]. We have performed additional MCMC analyses of the baseline data set supplemented with Dark Energy Survey Year-3 data [14] and supplemented with data from ACT [130, 131].

From the analysis of the baseline data set we find that EDS can accommodate lower S_8 values than EDE without compromising on H_0. The low-S_8-high-H_0 region of parameter space is correlated with small but negative c, and we find a mild overall preference for $c < 0$ in the fit to the baseline data set. When the data set is supplemented with DES-Y3, we find that S_8 decreases while leaving H_0 nearly unchanged, while maintaining the preference for $c < 0$. Compared to EDE, we find EDS is better able to accommodate the DES-Y3 data by

$\Delta\chi^2_{\rm DES-Y3,EDS-EDE} = -1.1$. This demonstrates the ability of the EDS model to at least partially resolve the tension of EDE with large scale structure data.

When ACT data are included we find a significant improvement on the constraint on c, driven largely by the improved constraint on z_c. Finally, all of these analyses constrain c to be significantly less than 1: we find $c < 0.068$ from the baseline data set, at 95% CL, and $c < 0.035$ and $c < 0.042$ at 95% CL when DES-Y3 or ACT are included, respectively. Taken at face value, this indicates a tension between the EDE resolution of the Hubble tension and the SDC.

Finally, we evaluate the overall preference of the data for the EDE model vs. EDS. To compare the EDS and EDE models we calculate the Akaike Information Criterion [151], which for the baseline data set yields $\Delta{\rm AIC} \simeq 0$, suggesting no preference for one model over the other. A more detailed model comparison could be done by computing the Bayesian evidence for each model; we leave this for future work.

We close this analysis with the following summary comments:

1. The EDS extension of EDE, namely EDE with the EDE-dependent dark matter mass $m_{\rm DM}(\phi) = m_0 e^{c\phi/M_{\rm pl}}$, can partially ameliorate the tension between the EDE resolution of the Hubble tension and LSS data. However, the data are statistically consistent with $c = 0$.

2. ACT data significantly constrain both the timing z_c of the EDE component and the EDS coupling parameter c. We find that supplementing the baseline data set with ACT data improves the constraint on c by a factor of two, and nearly eliminates the preference for $c < 0$.

3. Order-1 values of c in H_0-resolving EDE are ruled out by the data. While the SDC does not make any prediction for the fraction of dark matter to which the EDE scalar is coupled, this nonetheless suggests a mild tension between the SDC and EDE resolution of the H_0 tension.

There remain many directions for future work. Our analysis is motivated by the SDC, but the latter makes no prediction for fraction of dark matter to which the scalar field couples. Therefore a natural model extension is allow this fraction to vary in the fit to cosmological data sets. Other variations of our analysis would be to consider different choices of $V(\phi)$, such as monomial ϕ^n or hyperbolic $\tanh(\phi/f)^n$ potentials, and different choices of the dark matter coupling, such as $m_{\rm DM} = m_0(1 + c\phi^2/M_{pl}^2)$. A final possibility is to examine the role of EDE-dark matter interactions in resolving the coincidence problem inherent in early universe resolutions to the Hubble tension, namely, why the new physics becomes transiently relevant around matter-radiation equality, and not in the many decades of redshift before this epoch. We leave these interesting possibilities to future work.

CHAPTER 5

PHENOMENOLOGY OF MODIFIED GRAVITY AT RECOMBINATION

5.1 Introduction

Since the discovery of cosmic acceleration [152, 153], understanding its physical origin has become one of the primary goals of experimental efforts to measure the cosmic microwave background (CMB) and the large scale structure (LSS) of the Universe. In parallel it has been realized that the same measurements can be used to study gravity on cosmological scales including the possibility that modified gravity (MG) could explain cosmic acceleration (for reviews, see Refs. [154, 155, 156]).

Both CMB measurements and LSS data, probing the universe mainly at early and late times respectively, have proven to be extremely powerful in pursuing this program. Current surveys already provide precision constraints [23, 157, 8, 45] and future surveys, such as CMB-S4 [158], Euclid [159] and LSST [160], are expected to greatly exceed their performance [161, 162, 163, 164] and test General Relativity (GR) to unprecedented precision.

Most of the phenomenological effort in testing gravity on cosmological scales has been focused on constraining parameterized modifications to the Einstein equations relating the matter density contrast to the lensing and the Newtonian potentials [165, 166, 167, 168, 169, 170] and has targeted the late times, during the epoch of cosmic acceleration [171, 18, 172, 173, 174].

In this paper we discuss thoroughly for the first time the phenomenology and observational imprints of such modifications to gravity at early times and especially at the time of recombination. By enforcing the conservation of comoving curvature on superhorizon scales, we determine the initial conditions and evolution of perturbations in the radiation dominated epoch, relating their amplitude to inflationary perturbations. We implement this approach

in the Einstein-Boltzmann solver CAMB [175] extending the range of applicability of the MGCAMB code [161, 176] to early times.

Considering a parametrization for deviations from GR that decouples early and late times, we discuss both analytically and numerically the behavior of linear perturbations at all epochs of the universe and their impact on cosmological observables. In particular we focus on the MG imprint left on the acoustic peaks of the CMB power spectrum and baryon acoustic oscillations (BAO). We complete this analysis with a discussion of the MG effects on the clustering of LSS and on the lensing of the CMB and galaxies. As a result we significantly enlarge the pool of measurements that can be used to test gravity, notably, with the inclusion of the full constraining power of CMB observations.

These extensions allow us to investigate whether MG effects at early times could explain existing discrepancies between cosmological datasets [177] and in particular tensions between CMB measurements and low redshift probes (see also [178] and references therein for related work on early dark energy). We show that a different value for the effective gravitational constant at early times can partially relax tensions internal to the CMB dataset and between the CMB and local measurements of the Hubble constant and weak lensing of galaxies. This is achieved by changing the CMB temperature, polarization and lensing predictions in a compatible manner due to the combined effect that MG has on the acoustic oscillations and on lensing and results in a preference for a larger gravitational constant at early times at greater than 98% C.L. We comment on why such a resolution is not possible with only late time modifications to gravity.

This paper is organized as follows. In Sec. 5.2 we review the parametrized framework to modified gravity that we use and present initial conditions for superhorizon perturbations. In Sec. 5.3 we discuss analytically and numerically the behavior of cosmological perturbations at different epochs. In Sec. 5.4 we present the effect of such modifications on the acoustic peaks of the CMB and other cosmological observables. In Sec. 5.5 we review the tools that

we use in practical tests of MG at early and late times. In Sec. 5.6 we present the data constraints and discuss parameter degeneracies and the coordination of different physical effects to alleviate tensions. We conclude in Sec. 5.7.

5.2 Parametrized deviations from ΛCDM

In Sec. 5.2.1 we review the general parameterized approach to modifications of gravity for linear perturbations employed in Ref. [176], which assumes a metric theory of gravity with minimally coupled ordinary matter. To extend this parametrization to early times, we derive the superhorizon solutions to the perturbation equations in Sec. 5.2.2 and relate the amplitude of perturbations above the horizon to the amplitude of curvature perturbations set by inflation. We assume a given, but possibly modified, background Hubble expansion rate with a constant effective equation of state parameter. These general relations are applied to specific cases that isolate the various aspects of the modifications in the following sections.

5.2.1 Modified Gravity Equations

In conformal Newtonian gauge, metric perturbations are specified by two gravitational potentials, the Newtonian potential Ψ and the intrinsic spatial curvature potential Φ, giving the line element in a spatially flat background:

$$ds^2 = a^2(\tau)[-(1+2\Psi)d\tau^2 + (1-2\Phi)\delta_{ij}dx^i dx^j]\,, \tag{5.1}$$

where $a(\tau)$ is the scale factor as a function of conformal time τ. In addition the stress-energy tensor for the matter species that we consider is given at first order in perturbations by:

$$\begin{aligned} T^0_{\ 0} &= -\rho - \delta\rho\,, \\ T^0_{\ j} &= (\rho + P)v_j\,, \\ T^i_{\ j} &= (P + \delta P)\delta^i_{\ j} + \pi^i_{\ j}\,, \end{aligned} \tag{5.2}$$

where ρ and $\delta\rho$ are the average energy density and its perturbation, P and δP are the average pressure and its perturbation, v_j is the fluid velocity and $\pi^i_{\ j}$ denotes the traceless ($\pi^i_{\ i} = 0$) component of the stress-energy tensor perturbations. In Fourier space, the scalar component of the velocity can be expressed as its divergence $\theta \equiv ik^j v_j$ and the anisotropic stress by $(\rho + P)\sigma \equiv -(\hat{k}_i\hat{k}^j - \delta_i^{\ j}/3)\pi^i_{\ j}$. We assume that matter is still covariantly conserved in the metric so that its equations of motion follow

$$\delta\rho' + 3(\delta\rho + \delta P) = -(\rho + P)\left(\frac{\theta}{\mathcal{H}} - 3\Phi'\right), \tag{5.3}$$

$$\begin{aligned} [(\rho + P)\theta]' + 4(\rho + P)\theta = \frac{k^2}{\mathcal{H}}\Big[&\delta P - (\rho + P)\sigma \\ &+ (\rho + P)\Psi\Big]\,, \end{aligned} \tag{5.4}$$

where $' = d/d\log a$ here and throughout. The evolution of anisotropic stress σ is given by the radiation Boltzmann equations and is also unmodified in form. Here $\mathcal{H} \equiv \dot{a}/a = aH$ is the conformal Hubble rate where dot denotes $d/d\tau$ here and throughout.

In GR, the Einstein equations determine the metric given the matter fields as:

$$k^2\Phi = -4\pi G a^2 \Delta\rho\,, \tag{5.5}$$

$$k^2[\Phi - \Psi] = 12\pi G a^2(\rho + P)\sigma\,, \tag{5.6}$$

where $\Delta\rho \equiv \delta\rho + 3\frac{\mathcal{H}}{k^2}(\rho + P)\theta$ is the comoving-gauge density perturbation. Following Ref. [176], we modify these two Einstein equations with the addition of two free functions of time and scale, $\mu(a,k)$ and $\gamma(a,k)$, to phenomenologically parametrize deviations from GR in the two metric variables:

$$k^2\Psi = -4\pi\mu G a^2[\Delta\rho + 3(\rho + P)\sigma]\,, \tag{5.7}$$

$$k^2[\Phi - \gamma\Psi] = 12\pi\mu G a^2(\rho + P)\sigma\,, \tag{5.8}$$

where μ parameterizes the effective gravitational constant as μG while γ encodes the ratio of the two potentials. When both μ and γ are equal to unity, the model reduces to GR and more generally we will refer to this parameterization as MG .

Notice that we parameterize the Poisson equation (5.7) with the lapse Ψ rather than the curvature potential Φ. This convention highlights the fact that Ψ enters directly into the dynamics of non-relativistic matter and makes it easier to implement the condition that its evolution given the background expansion depends only on Φ/Ψ above the horizon if the comoving curvature is conserved [167]. In this sense, μ scales the overall gravitational effect of all matter while γ encodes the difference between the gravitational effects on non-relativistic and relativistic matter.

Also note that μ and γ can in principle be arbitrary functions of time and scale allowing us to encompass the scalar sector of any metric theory of gravity where all matter species are minimally coupled to the metric (see, for example, Ref. [179] for a recent review).

5.2.2 Superhorizon Solutions and Initial Conditions

To utilize the MG parametrization described by Eqs. (5.7, 5.8) at early times, we have to derive initial conditions for perturbations when they are above the horizon. We present the main results in this section and further details on the specific case we consider in the next

section can be found in Appendix B.2.

In the standard cosmological scenario, initial conditions for the perturbations are set by inflation. Using the fact that comoving gauge curvature is still conserved as $k/\mathcal{H} \to 0$ (see Appendix B.1) we can compute the initial conditions at the time when inflation ends and set them for perturbations later on, before the given mode re-enters the horizon.

We can thus derive the superhorizon solutions and initial conditions for perturbations in any gauge assuming some background Friedmann-Robertson-Walker expansion. If $\mathcal{R}$ is constant, Ref. [180] shows, using a separate universe argument, that in any metric theory of gravity [1] with a spatially flat background

$$\mathcal{R} \approx -\Phi + \frac{H}{H'}(\Psi + \Phi'). \tag{5.9}$$

This equation has the formal solution

$$\Phi = -\left(1 - \frac{H}{g}\int d\log a \frac{g'}{H}\right)\mathcal{R} + C\frac{H}{g}, \tag{5.10}$$

where the integrating factor $g = e^{\int(\Psi/\Phi)d\log a}$ and C is an integration constant for what is generally a decaying mode.

Assuming that the background expansion has a Hubble rate $H \propto a^{-3(1+w)/2}$, we can solve this equation for Ψ and Φ. If the Friedmann equation itself is modified, w simply parameterizes the expansion history and is not necessarily the equation of state parameter of the matter. For the case where Φ/Ψ does not vary on the Hubble time scale or faster, which is true for most models during an epoch when $w = \text{const.}$, the growing mode of Eq. (5.10) is solved by constant Φ and Ψ. Assuming that the anisotropic stress of the matter is dominated by neutrinos, we can integrate their equation of motion to find these constants. Since this

1. In comoving gauge of the metric as defined in Ref. [180], Eq. (5.9) is exact and coincides with comoving gauge as defined by the matter velocity as $k/\mathcal{H} \to 0$ (see Eq. B.2).

equation is not modified in form, the result is the same as in GR

$$\sigma_\nu = \frac{8}{45}\frac{1}{1+4w+3w^2}\left(\frac{k}{\mathcal{H}}\right)^2\Psi, \tag{5.11}$$

so that

$$\Phi - \gamma\Psi = \frac{16}{15}\frac{\mu R_\nu}{1+4w+3w^2}\Psi, \tag{5.12}$$

where $R_\nu = 8\pi G\rho_\nu/3H^2$. Combining this with Eq. (5.9), we obtain

$$\begin{aligned}\Psi &= -\frac{15(1+4w+3w^2)}{10+16\mu R_\nu+30w+15\gamma(1+4w+3w^2)}\mathcal{R},\\ \Phi &= -\frac{16\mu R_\nu+15\gamma(1+4w+3w^2)}{10+16\mu R_\nu+30w+15\gamma(1+4w+3w^2)}\mathcal{R}.\end{aligned} \tag{5.13}$$

Our starting assumption that $\Phi/\Psi \approx$const. implicitly requires constant γ and μR_ν, but does not place other restrictions on whether the Friedmann equation is itself modified. This suffices for our purposes since R_ν is constant for a radiation dominated expansion with $w = 1/3$ and the neutrino anisotropic stress becomes negligible in other limits. For the more general case, one can solve for the evolution of Φ and Ψ given the evolution of γ and μR_ν by supplementing Eqs. (5.8) and (5.9) with their time derivatives.

5.3 Perturbation Evolution

From this point forward, we focus on an illustrative, but scale independent, parameterization of the parameters $\mu(a)$ and $\gamma(a)$, which isolates either early time or late time modifications to gravity, with the former being new to this work. This is achieved by using a smoothed step functional form for these functions, as discussed in Sec. 5.3.1. Furthermore, we assume an unmodified ΛCDM background to isolate the effect of the modifications to linear perturbation theory. We present analytic results for perturbation evolution in Sec. 5.3.2 and numerical results in Sec. 5.3.3. Most of the analytic results can be easily extended to the scale dependent

case since each k-mode evolves independently in linear theory.

5.3.1 Step Parameterization

In order to separate early time and late time effects on perturbations, we shall consider a phenomenological parametrization that models a transition between these two regimes. Furthermore, to isolate the effects of the modified perturbation equations from the influence of the background expansion, we assume an unmodified ΛCDM expansion history from this point forward.

In particular we parameterize μ and γ as step-functions in e-folds $N \equiv \log a$ with the following smooth step-like form:

$$f(x) = \frac{f_0 + f_\infty}{2} - \frac{f_0 - f_\infty}{2} \frac{x}{\sqrt{1+x^2}}\,, \tag{5.14}$$

where $x = (N - N_T)/\Delta_T$ and $f \in \{\mu, \gamma\}$. Here we have four parameters: f_0 and f_∞ are the values of the quantity today and at early times respectively, $N_T \equiv \log a_T$ denotes the e-folds of transition between the two regimes, and Δ_T is the e-fold width of the transition. In this paper, we set $N_T = -3.4$, corresponding to $z \sim 30$ as it is approximately the median of the ~ 6 e-folds between recombination and today. As such, the transition happens at a time that is well after recombination, before the late time accelerated expansion and beyond the reach of the next generation of large scale structure surveys. We further choose $\Delta_T = 1$ to avoid a sharp transition which would introduce spurious effects on the CMB power spectrum.

We test the stability of our results to the choice of transition width in Appendix B.3. The results depend only weakly on Δ_T if it is around 1, and become sensitive to Δ_T when it is much larger since the transition would affect physical processes around recombination. When Δ_T is very small the results converge to a unique answer, but produce spurious effects on the CMB power spectrum which would not be present if the transition occurred on the

Hubble time scale or greater.

Thus, in addition to ΛCDM parameters, we have four additional free parameters: μ_0, μ_∞, γ_0, γ_∞. Note that for more realistic gravity models we usually expect the two functions μ and γ to be scale dependent.

5.3.2 Analytic Results

In this section we show some analytic results that help interpret the novel features of perturbation evolution in MG at early times. We discuss the limiting cases of superhorizon and subhorizon evolution in the various epochs of a ΛCDM background expansion. Using the step parameterization, we isolate the impact of a nearly constant μ and γ at early and late times.

Superhorizon Solutions

On superhorizon scales, our general derivation in the previous section applies before and after the step. In particular, given our assumption that the background expansion history is unmodified, we have in the radiation dominated epoch

$$\begin{aligned} \Psi &= -\frac{10}{10\gamma+5+4\mu R_\nu}\mathcal{R}\,, \\ \Psi+\Phi &= -\left(1+\frac{5}{10\gamma+5+4\mu R_\nu}\right)\mathcal{R}\,. \end{aligned} \tag{5.15}$$

where $(\Psi+\Phi)/2$ is the Weyl potential that enters into gravitational lensing and the integrated Sachs-Wolfe effect in the CMB. While both γ and μ larger than one would result in a smaller amplitude of the initial gravitational and Weyl potentials, their quantitative effect is different. In particular, changing μ results in a smaller change in the gravitational potentials, with respect to γ, since it is multiplied by the neutrino fractional energy density R_ν. This is a consequence of the fact that, given the background expansion, superhorizon potentials

depend only on Φ/Ψ which itself is determined by γ alone in the absence of anisotropic stress. This behavior of the Weyl potential plays an important role in understanding the modified CMB power spectrum that we shall discuss in Sec. 5.4.1.

For modes that remain outside the horizon after radiation domination, when $R_\nu \ll 1$, the solutions well before or after the step reduce to

$$\Psi = -\frac{3(1+w)}{2+3\gamma(1+w)}\mathcal{R}\,, \tag{5.16}$$

$$\Psi+\Phi = -\frac{3(1+w)}{2+3\gamma(1+w)}(1+\gamma)\mathcal{R}\,, \tag{5.17}$$

and in particular in the matter dominated limit $w = 0$ and these relations further simplify. Notice that after radiation domination the superhorizon solution does not depend on μ but only γ. During the recent acceleration epoch, well after the step, w is not constant and so these solutions do not strictly apply but since $\Phi/\Psi = \gamma$, Eq. (5.10) implies

$$\Psi = -\left(1-\frac{H}{\gamma a^{1/\gamma}}\int d\log a\frac{a^{1/\gamma}}{H}\right)\frac{\mathcal{R}}{\gamma},$$

$$\Psi+\Phi = (1+\gamma)\,\Psi. \tag{5.18}$$

This integral relation can be expressed in terms of the hypergeometric function for the ΛCDM expansion history which shows that Eq. (5.16,5.17) qualitatively describe the transition to Λ domination but predicts it to be more rapid. A larger γ also causes a slower decay of the potential during the acceleration epoch.

Subhorizon Solutions

In the subhorizon regime, the evolution of the matter perturbations determines the evolution of the potentials and vice versa. Since the equations of motion of matter given the metric are not affected by MG, we first examine its behavior given the metric.

Deep in the radiation dominated epoch, the baryon density is negligible and the photon density, or monopole perturbation $\Theta_0 = \frac{1}{4}\delta_\gamma$, can be formally expressed as (see Eq. D-6 in Ref. [181][2]):

$$[\Theta_0 - \Phi](\tau) = [\Theta_0 - \Phi](0)\cos(kc_s\tau) - \frac{k}{\sqrt{3}}\int_0^\tau d\tau'[\Phi + \Psi](\tau')\sin[kc_s(\tau - \tau')]\,, \tag{5.19}$$

where $c_s = 1/\sqrt{3}$. Since the radiation density fluctuation dominates the source of the Poisson equation, once the photons enter into acoustic oscillations around sound horizon crossing, the Weyl potential decays to zero. This decay also provides a source to the acoustic oscillations through the integral term in Eq. (5.19) which we refer to as the radiation driving effect. This extra source can carry a phase shift if the timing of the decay is modified. This same effect causes the well-known phase shift due to freestreaming neutrinos (e.g. [182]).

As we shall see, the phenomenology of acoustic oscillations is then determined by two pieces: the initial superhorizon conditions for $\Theta_0 - \Phi$, the Weyl potential and the modification of the timing of the decay of the latter. Since $\Theta_0(0) = -\Psi(0)/2$, MG does not change the initial value of $[\Theta_0 - \Phi](0) = \mathcal{R}$, so the change of this solution comes from the integral of the Weyl potential. Since the Weyl potential always decays to zero after horizon crossing in the radiation dominated epoch, the amplitude of the driving effect depends on its initial value. We see from Eq. (5.15) that a larger γ gives a lower value of $|\Phi + \Psi|(0)$, which decreases the driving effect. The impact of μ on the amplitude is smaller but it does influence the timing of the decay. A larger μ provides a larger source to the Weyl potential and delays the decay. This then produces a phase shift in the acoustic oscillations as we shall see in Sec. 5.4.1.

Cold dark matter density perturbations δ_c evolve according to:

$$\ddot{\delta}_c + \frac{\dot{a}}{a}\dot{\delta}_c = -k^2\Psi - 3\ddot{\Phi}\,. \tag{5.20}$$

2. Note that Φ in Ref. [181] is $-\Phi$ in this paper and $V = \theta/k$, $p\Pi = 3(\rho + P)\sigma/2$.

In the radiation dominated epoch, we can treat the right hand side as an external driving force $S(k,\tau) = -k^2\Psi - 3\ddot{\Phi}$. Given that the potentials decay at horizon crossing, as discussed above, well after horizon crossing δ_c settles into a logarithmic growing mode [183]:

$$\delta_c(k,\tau) = -A\Psi(k,0)\log(Bk\tau)\,, \tag{5.21}$$

where A and B are constants that can be determined from

$$\begin{aligned} A &= -\frac{1}{\Psi(k,0)}\int_0^\infty d\tau S(k,\tau)\tau\,, \\ A\log B &= \frac{3}{2} + \frac{1}{\Psi(k,0)}\int_0^\infty d\tau S(k,\tau)\tau\log(k\tau)\,. \end{aligned} \tag{5.22}$$

The MG effect therefore again comes from the initial conditions and the timing of the decay. Recall also that $\tau \propto a$ in the radiation dominated epoch. Even though A and B themselves have no k-dependence deep in the radiation dominated regime, a change in B alters the transition in k between the constant and $\log(k\tau)$ terms in δ_c. A change in B occurs when the epoch of potential decay is shifted. This is especially pronounced for μ whereas γ mainly changes the overall amplitude A.

After the Universe becomes matter dominated, the self gravity of matter causes its density fluctuation to grow due to $k^2\Psi$ whereas $\ddot{\Phi}$ remains negligible. After recombination, the baryon density fluctuation also obeys Eq. (5.20) and so the combined baryon and cold dark matter component is

$$\delta_m'' + \left(2 + \frac{H'}{H}\right)\delta_m' + \frac{k^2}{\mathcal{H}^2}\Psi = 0, \tag{5.23}$$

as usual. The MG influence comes from the Poisson equation (5.7) for Ψ and involves μ whereas γ drops out of the equations. A larger μ increases the amplitudes of the potentials due to the larger effective gravitational constant and therefore enhances the growth. During the matter dominated epoch, neglecting the effect of massive neutrinos for simplicity, we

have

$$\delta_m'' + \frac{1}{2}\delta_m' - \frac{3}{2}\mu\delta_m = 0 \tag{5.24}$$

and therefore for the growing mode

$$\delta_m \propto a^{\frac{\sqrt{24\mu+1}-1}{4}} . \tag{5.25}$$

When $\mu = 1$, it reduces to the standard $\delta_m \propto a$ solution. When μ deviates from unity, the matter perturbation increases as μ increases. Massive neutrinos slow the growth rate in the same way below their freestreaming scale by acting in the opposite sense as a component that modifies the background expansion but does not contribute to the perturbations.

In the acceleration epoch, to good approximation $\delta_m \propto D^{\frac{\sqrt{24\mu+1}-1}{4}}$ where D is the GR linear growth function of ΛCDM [184].

5.3.3 Numerical Results

In this section we complement our analytical analysis with results from numerical integration using the modified Einstein-Boltzmann code described in Appendix B.2.

In Fig. 5.1, we show the numerical solution for the Weyl potential at different scales while in Fig. 5.2 we show the relative comparison of the transfer functions of the Weyl potential and synchronous gauge matter density perturbations at redshift zero. We choose four example models defined by $\mu_\infty = 1.2$, $\gamma_\infty = 1.2$, $\mu_0 = 1.2$, $\gamma_0 = 1.2$ while keeping fixed all other cosmological parameters. We refer to the scale factors at matter-radiation equality, MG parameter transition, and matter-dark energy equality as, respectively, $a_{\rm eq}$, $a_{\rm T}$, and $a_{\rm DE}$. The wavenumbers of the modes that enter the horizon at the corresponding times, which are determined by $k_i = \mathcal{H}(a_i)$, are referred to as $k_{\rm eq}$, $k_{\rm T}$, and $k_{\rm DE}$.

As we can see from Fig. 5.1, before horizon crossing, as expected from the analytic results, μ has a very limited impact on the evolution of the Weyl potential, while a larger

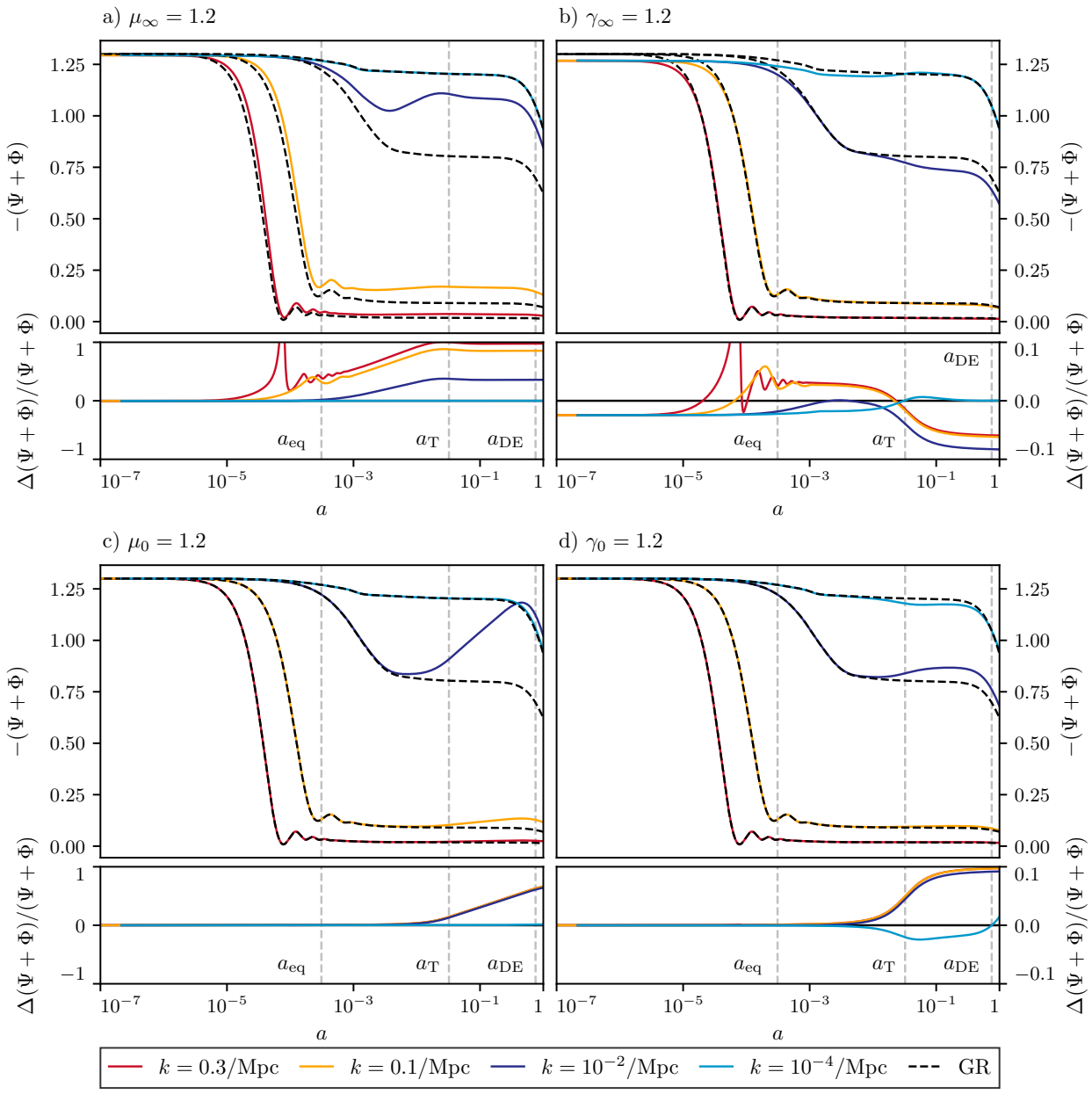

Figure 5.1: The comparison of the Weyl potential evolution between our MG example models and GR. The four panels represent models with $\mu_\infty = 1.2$, $\gamma_\infty = 1.2$, $\mu_0 = 1.2$ and $\gamma_0 = 1.2$ respectively. The three vertical dashed lines indicate, from left to right respectively, matter-radiation equality, the transition of the MG parameters (here $z = 30$, see definition in Sec. 5.3.1), and Λ-matter equality. The positions where the Weyl potentials drop indicate horizon crossing for different k-modes. When crossing the horizon during radiation epoch, a larger μ delays the potential decay significantly while the same change in γ leads to a small effect. For details of the early and late time behaviors and the effect of the transition, see the discussion in Sec. 5.3.3.

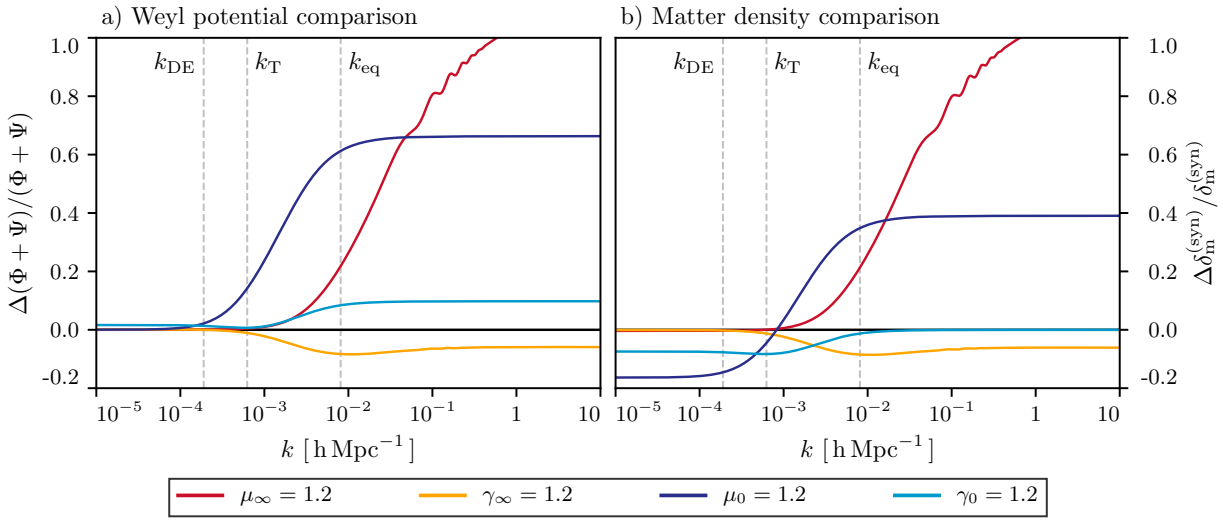

Figure 5.2: The fractional change in transfer functions relative to their GR values at redshift $z = 0$ due to MG of (a) the Weyl potential and (b) the synchronous gauge matter density perturbations. Different colors represent different example models as in Fig. 5.1, as shown in legend. The vertical lines show the scales, $(k_{\rm DE}, k_{\rm T}, k_{\rm eq})$, corresponding to the modes crossing the horizon at Λ-matter equality, transition in the MG functions, and matter-radiation equality respectively.

γ decreases its amplitude in both radiation dominated and matter dominated epochs and slows the potential decay in the acceleration epoch.

At horizon crossing, for modes that cross during radiation domination, an increase in μ delays the decay of the Weyl potential while the same change in γ leads to a much smaller effect. As we see in Eq. (5.19), this implies that μ being different from its GR value through recombination changes the phase of acoustic oscillations in the CMB. Modes that enter the horizon before matter-radiation equality (*i.e.* $k > k_{\rm eq}$) still grow logarithmically but if $\mu_\infty \neq 1$, the change in the decay epoch also changes the constant vs. logarithmic coefficients that results in an enhancement that grows with k, as shown in Fig. 5.1a. γ mainly changes the overall amplitude of the decay and therefore leads to much less scale dependence.

After horizon crossing, during the matter and acceleration epochs, a larger μ increases the growth rate of perturbations due to a larger effective gravitational constant μG. The relative change in growth is scale independent during the matter and acceleration epochs,

since we assumed a scale independent parametrization for μ.

We now comment on the behavior of perturbations when crossing the transition of the MG functions at $z = 30$. For subhorizon modes, the time derivative term Φ' in the continuity equation (5.4) becomes negligible, so that the density perturbations remain continuous even when γ or μ change rapidly. From the Poisson equation (5.7) we know that $\Psi \propto \mu$, and from Eq. (5.8) we have $\Phi = \gamma\Psi \propto \mu\gamma$ and hence $(\Psi + \Phi) \propto \mu(1 + \gamma)$. Therefore, a transition in $\mu(1 + \gamma)$ results in a transition in the Weyl potential that can be clearly seen for γ on subhorizon scales in Fig. 5.1. This feature is present but hidden in the μ case due to the change in the growth of density perturbations that overcomes this effect.

For superhorizon modes in the matter dominated limit, μ is irrelevant for the two potentials and remains so during the transition, we thus see zero impact in the μ_∞ and μ_0 example models. For γ, on the other hand, the potentials settle on the predictions from Eq. (5.17) before and after the transitions since the conservation of comoving curvature ensures that there is no memory of the transition once it is complete.

Combined these changes in growth lead to features in the transfer functions at $z = 0$ displayed in Fig. 5.2. At scales that are superhorizon at $k_{\rm DE}$, only γ_0 shows a relative deviation from GR, in the Weyl potential. For a transition from an unmodified to a modified gravity model, $\mu = 1 \to 1.2$, the scale independent change in growth appears as a scale independent increase in the transfer function at $k \gg k_{\rm T}$. On the other hand with a transition from a modified to an unmodified gravity model $\mu = 1.2 \to 1$, this matter dominated growth only happens between horizon crossing and a_T so that its full effect occurs for $k \gg k_{\rm eq}$. In addition there is also a scale-dependent component due to the modified logarithmic growth during radiation domination.

For both γ_0 and γ_∞, the transition produces a step in the Weyl potential for modes $k > k_{\rm T}$ and hence a step in the Weyl transfer function. For γ_∞ there is an additional change in the logarithmic growth during radiation domination that partially compensates for this

step.

This discussion is tightly connected with the behavior of matter density perturbations whose scale dependence at $z = 0$ can be seen in Fig. 5.2. There we show the relative comparison of the synchronous gauge matter density perturbations with respect to their GR behavior.

For both γ_∞ and μ_∞ the behavior is very close to that of the Weyl potential (for more detail, see above discussion). For the late time models, μ_0 and γ_0, some differences appear. In the μ_0 model, the amplitude on superhorizon scales decreases because μ does not affect the evolution of Ψ at such scales, thus $\delta_c \propto 1/\mu$. In the γ_0 model, the amplitude on superhorizon scales decreases because its impact on Ψ and hence δ_c differs from $\Phi + \Psi$, see Eq. (5.16). For the modes that enter the horizon well before $z = 30$, the amplitude remains unchanged because γ does not affect the subhorizon matter perturbation evolution.

5.4 Impact on Observables

In this section we study the impact of MG on cosmological observables, including the CMB power spectrum, the BAO scale, gravitational lensing and the matter power spectrum.

5.4.1 CMB temperature power spectrum

As we have seen in the previous sections, early time MG affects both initial conditions and the evolution of perturbations. Therefore we expect a change in the physics of photon-baryon acoustic oscillations that will have a significant impact on the CMB power spectra. Since the Boltzmann equations remain unchanged in form, if we treat the gravitational potential as an external driving force for the photon-baryon fluid, the impact of MG can be understood from these changes in the potential evolution in the same way as in GR [181].

To aid our interpretation of these effects, we start with the impact on the sources of CMB anisotropy in k-space in Fig. 5.3. There we show $\Theta_0 + \Psi$, the monopole corrected for

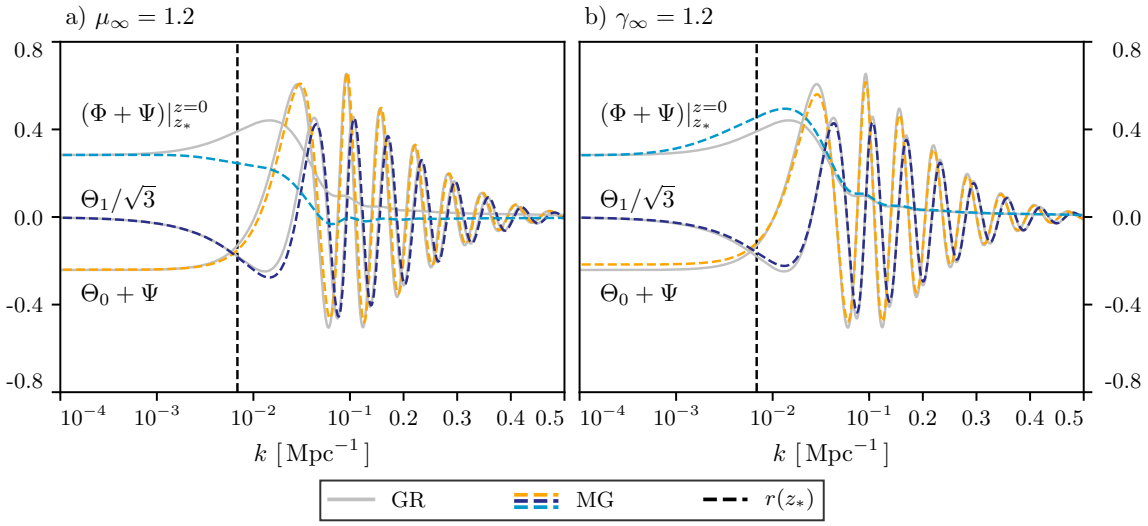

Figure 5.3: The CMB anisotropy source functions in k-space in units of amplitude of primordial comoving curvature perturbation in two MG example models with $\mu_\infty = 1.2$ and $\gamma_\infty = 1.2$ and GR. Different lines correspond to different physical effects and models, as shown in figure and legend. The vertical dashed line shows mode that crosses the horizon at recombination (z_*).

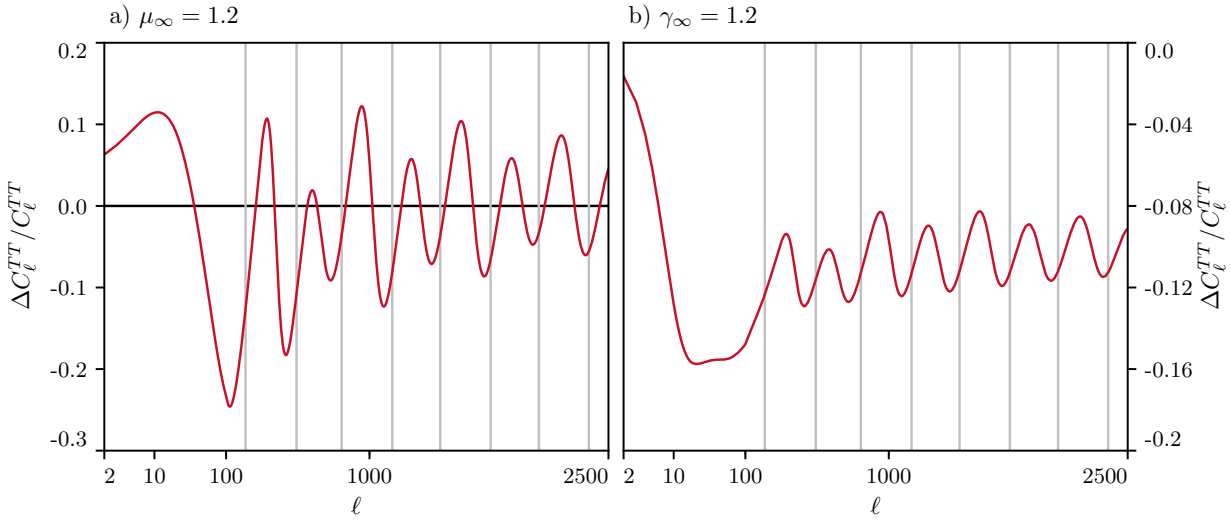

Figure 5.4: The fractional change in the unlensed CMB temperature spectrum in two MG example models with $\mu_\infty = 1.2$ and $\gamma_\infty = 1.2$ relative to the GR spectrum. The vertical solid lines indicate the angular position of the GR peaks of the unlensed CMB spectrum. Notice that the variations are mainly out of phase with the peaks.

the ordinary Sachs-Wolfe effect, and the dipole Θ_1 at the redshift of recombination z_*. We also show the difference in Weyl potential between recombination and today $(\Phi+\Psi)|_{z_*}^{z=0}$ as

a proxy for the integrated Sachs-Wolfe (ISW) effect, including its early time contribution. Fig. 5.3 shows these three quantities in GR and in two example models with $\mu_\infty = 1.2$ and $\gamma_\infty = 1.2$ respectively. In addition we can see in Fig. 5.4 the un-lensed scalar part of the CMB temperature spectrum for the two example models compared to the GR scalar spectrum in the harmonic domain.

As we can see μ_∞ induces a significant phase shift of both the temperature monopole and dipole. This phase shift comes from the shift in the epoch that the Weyl potential drives the oscillations as discussed in the previous section, see Eq. (5.19), and shown in the top left panel of Fig. 5.1. This is the leading effect that we see, with respect to GR, in Fig. 5.4(a).

In the angular power spectra, this phase shift corresponds to a shift of the scale of the acoustic peaks to higher multipole with $\mu_\infty = 1.2$ vs. 0 of $\Delta\ell \simeq 18$, where the exact number is calibrated on the third peak. In Fig. 5.4 this is visible as oscillatory fractional changes to the spectrum that are out of phase with the peaks themselves (vertical lines). This should be contrasted with a change in the fundamental angular scale of the acoustic peaks θ_s which causes a shift $\Delta\ell \simeq -\ell\Delta\theta_s/\theta_s$. As we shall see, the two parameters μ_∞ and θ_s are consequently partially degenerate, with the degeneracy broken by the measurement of multiple acoustic peaks.

A smaller effect induced by a change in μ_∞ is a difference in baryon modulation. As we can see in Fig. 5.3 there is an amplitude change for modes that reach the oscillation minimum, as opposed to maximum, at recombination. This is caused by the fact that increasing μ_∞ increases the gravitational potential and hence the baryon modulation effect. At about the same relevance we can also see the effect of the change in the epoch of Weyl potential decay on the efficiency of radiation driving. The latter two effects are difficult to see in Fig. 5.4 as they are sub-leading with respect to the phase shift. They can be uncovered by cancelling the shifts due to μ_∞ and θ_s at a fiducial multipole, e.g. the third acoustic peak.

A larger γ_∞, on the other hand, shows three effects on the CMB power spectrum: a

decrease in the amplitude of the acoustic peaks, a further decrease at scales larger than the first acoustic peak, $10 \lesssim \ell \lesssim 100$, and a phase shift. First of all, the overall amplitude change comes from the driving effect. As we see in Eq. (5.19), a larger γ_∞ gives a lower initial value of $|\Phi + \Psi|$, which decreases the value of $\Theta_0 + \Psi$, hence the overall amplitude of CMB temperature fluctuation. Notice that the integral part in Eq. (5.19) has opposite sign and approximately twice the amplitude of the initial part in GR, so the fractional difference of C_l^{TT} is approximately 4 times as the fractional difference of the initial Weyl potential Eq. (5.15) and another factor of 2 comes from the square in the calculation of power spectrum.

On intermediate scales just larger than the first acoustic peak, the reduction in the amplitude of the Sachs-Wolfe and Doppler effects further suppresses power in Fig. 5.4. Above the horizon in the matter dominated epoch $\Theta_0 + \Psi = \Psi/3$ and so Eq. (5.15) and the photon conservation equations predicts the rough amplitude with some reduction in the effect due to the ISW effect. At large scales where fluctuations are above the horizon at the transition, the SW and ISW effects from the transition add coherently and since $\mu = 1$ after the transition, they cancel leaving temperature power spectrum differences that vanish as $\ell \to 0$.

Finally a deviation of γ_∞ from unity also induces a small phase shift. Calibrated to the third peak, the shift for $\gamma_\infty = 1.2$ is $\Delta\ell \simeq 3$ and remains nearly constant throughout the acoustic peaks. We shall see that this phase shift causes a partial degeneracy between μ_∞ and γ_∞.

MG at late time, conversely, does not affect acoustic oscillations but rather changes the spectrum of un-lensed CMB temperature fluctuations through the ISW effect. At the transition, the time derivative of the Weyl potential causes an enhancement of the temperature power spectrum that is dependent on the width of the transition. As we show in Appendix B.3, if the transition is much sharper than $\Delta_T \sim 1$ efold, the ISW effect makes the CMB

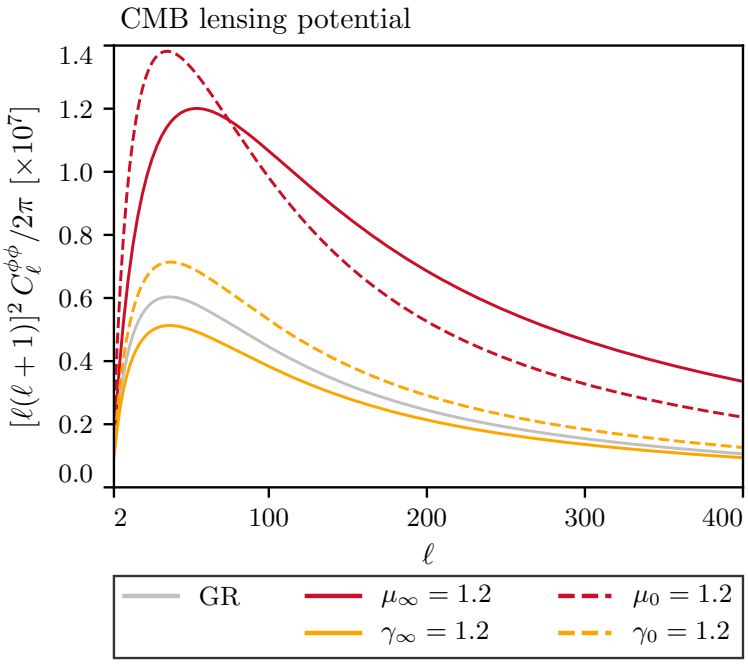

Figure 5.5: The CMB lensing potential power spectrum in the harmonic domain. Different colors correspond to different models as shown in legend.

highly sensitive to the difference between μ and γ at early and late times.[3] Since such a transition is unrealistic for a model whose deviations from GR evolve on the Hubble timescale, we fix $\Delta_T = 1$.

Both early times MG models modify the Weyl potential, as shown in Fig. 5.2a, and thus change the lensing potential of the CMB accordingly in Fig. 5.5. Raising either μ_∞ or μ_0 raises the amplitude of the lensing potential whereas μ_∞ also causes a notable change in its shape as a result of the scale dependent enhancement of modes that entered the horizon during radiation domination as shown in Fig. 5.2a. Raising γ_∞ or γ_0 decreases and increases the lensing potential respectively with little change in the shape. These changes to the lensing potential produce observable effects in the smoothing of the acoustic peaks and CMB lens reconstruction.

3. Furthermore as discussed in Appendix B.3, MGCAMB implements the switch between GR at early times and potential deviations at late times instantaneously and produces inconsistent, not merely overly sensitive, results if the parametrization is not designed to go smoothly to zero on the low redshift side of the transition (cf. [23] Planck 2015 paper).

5.4.2 Weak Lensing

Measurements of the galaxy weak lensing (WL) shear correlation function provide a powerful way of studying MG models. In this section we discuss the impact of MG on weak lensing observables through the Weyl potential.

As we discussed in the previous sections, in GR, anisotropic stress is negligible at late times so the Weyl potential power spectrum is just a re-scaling of the matter power spectrum, but this is not generally true in MG. The difference between the two can be clearly seen comparing the two panels of Fig. 5.2. For this reason it is important to build lensing observables starting from the Weyl potential power spectrum.

The amplitude of the WL power spectrum is usually parametrized in terms of σ_8, the rms amplitude of linear matter density fluctuations Δ_m convolved with a spherical tophat of radius $8\,h^{-1}\,\mathrm{Mpc}$ at $z = 0$, and the matter density parameter Ω_m, in their combination $S_8 \equiv \sigma_8 \Omega_m^{0.5}$. When considering MG models we need to take into account the difference between the Weyl potential and matter density perturbations. For this reason we replace the matter density fluctuations Δ_m with $\Delta_{\rm WL}$ where

$$\Delta_{\rm WL} \equiv -\frac{k^2(\Phi+\Psi)}{8\pi G a^2 \rho_m}\,, \tag{5.26}$$

and define $\sigma_8^{\rm WL}$ using this field. Eq. (5.26) is normalized such that, in GR and in absence of matter anisotropic stresses $\sigma_8^{\rm WL} \to \sigma_8$. In MG it is easy to see that, in absence of matter anisotropic stresses:

$$\sigma_8^{\rm WL} = \frac{1+\gamma}{2}\mu\,\sigma_8 \tag{5.27}$$

so that its general definition extends the definition in [8] and reduces to it when matter anisotropic stresses are negligible.

We show in Fig. 5.6 the fractional change in $\sigma_8^{\rm WL}$ as a function of the four MG parameters

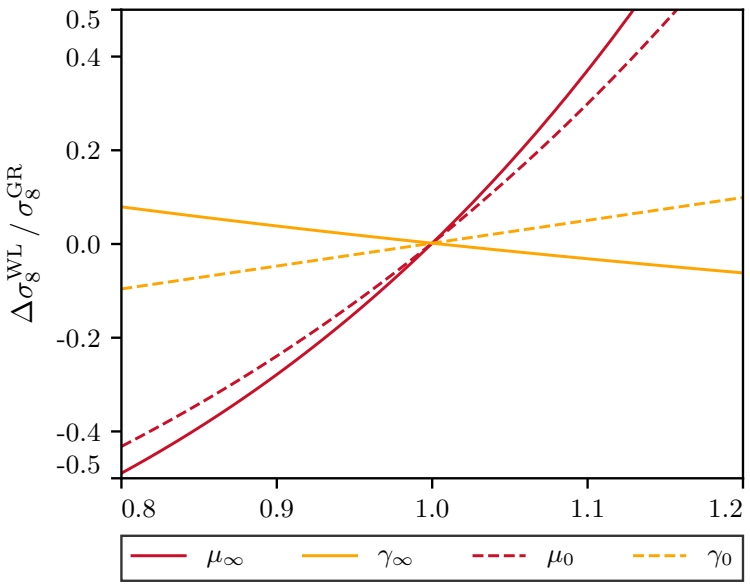

Figure 5.6: The fractional change in $\sigma_8^{\rm WL}$ from its the GR value. Different colors correspond to different models as shown in legend.

around the GR value with all other parameters fixed. As we can see this closely resembles the amplitude change of the Weyl potential at small scales, shown in Fig. 5.2. Raising μ_∞, μ_0, or γ_0 all raise the lensing observable, whereas raising γ_∞ lowers it. Furthermore, for the γ_0 case, the amplitude of the matter power spectrum on sub-horizon scales does not change while the amplitude of the Weyl potential tracks the change in γ_0 and illustrates why it is important to use Eq. (5.26) as the parameter controlling WL. Notice that the definition of $\sigma_8^{\rm WL}$ only addresses one aspect of the difference between GR and MG by incorporating the dependence on MG of the redshift zero calibration. The amplitude of the lensing signal at a given redshift depends on the growth of perturbations and scale of the measurements. In GR these are addressed by considering the combination $\sigma_8\Omega_m^{0.5}$ while in MG there would be a residual dependence on μ and γ due to the scale and redshift dependent sub horizon growth. For compatibility with this convention we use $\sigma_8^{\rm WL}\Omega_m^{0.5}$ as a simple proxy for the WL observable in MG but test its fidelity in the $\mu_0 - \gamma_0$ space directly (see Fig. 5.10).

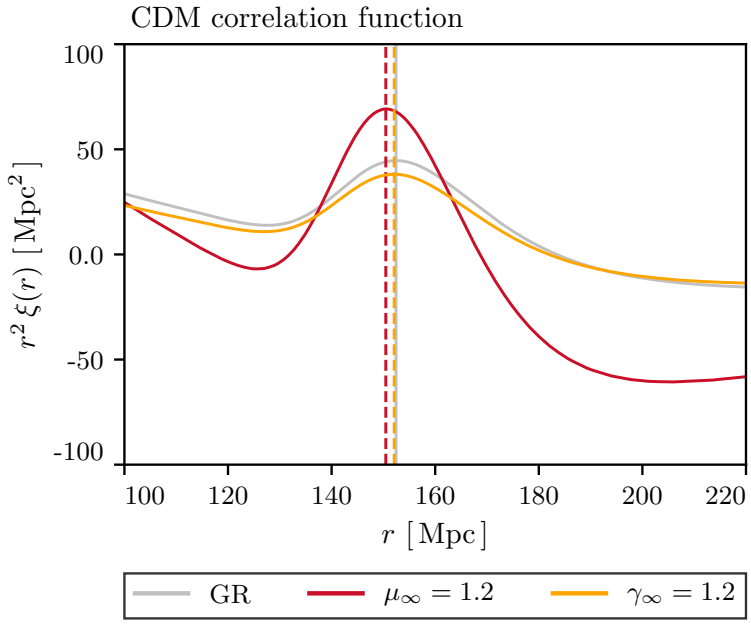

Figure 5.7: The CDM spatial linear correlation function $\xi(r)$. Different colors correspond to different models as shown in legend. Vertical lines represent the BAO peak which are slightly shifted by early time MG parameters.

5.4.3 Matter power spectrum

The clustering of galaxies provides another powerful and complementary probe of MG. The modifications induced on the underlying CDM power spectrum that it traces follow closely what we discussed for the transfer functions in Sec. 5.3.3. Galaxies are biased tracers of the CDM and as shown in [185, 186], bias in the linear regime is expected to be scale dependent if the linear growth is also scale dependent as it is in MG. Precise modeling within parametrized approaches requires cosmological simulations but one would expect that it qualitatively follows the response of the local growth to the linear density perturbation treated as a local background density [186].

An observable that is more robust to these complications is the location of the BAO peak in the galaxy correlation function. However, in case of early modified gravity, we have to take into account the fact that an acoustic phase shift induced by the decay of the gravitational potential would also shift the position of the BAO peak.

In Fig. 5.7 we can clearly see this effect. We compare the CDM spatial linear correlation function in GR to the two early MG models that we consider, keeping all other cosmological parameters fixed. The phase shift induced by μ_∞ shows as a shift in the BAO peak of the correlation function. In our test case of $\mu_\infty = 1.2$ we have that $\Delta r_{\rm peak} = 1.9\,{\rm Mpc}$ corresponding to $\Delta r_{\rm peak}/r^{GR}_{\rm peak} = 1.2\%$.

Since γ_∞ also induces a phase shift we can observe a corresponding shift in the BAO peak also in the case of $\gamma_\infty = 1.2$, with $\Delta r_{\rm peak} = 0.35\,{\rm Mpc}$ and $\Delta r_{\rm peak}/r^{GR}_{\rm peak} = 0.2\%$. The relative sizes of the γ_∞ and μ_∞ shift in the BAO peak is the same as that of the phase shift in the CMB peaks.

Notice that the shape of the correlation function is also modified in these two cases, especially in the μ_∞ case where the there is a substantial enhancement of high-k power in Fig. 5.2. This would provide a powerful way of testing these models once bias is understood.

We warn the reader that the measured peak position in the galaxy correlation function is usually compared to the acoustic-scale distance ratio $D_V(z)/r_{\rm drag}$, as measured by a LSS survey with effective redshift z. While this holds in GR, it is not strictly true in early MG models so that one has to check whether the difference is within the experimental error bars.

5.5 Analysis Methods

In this section we discuss cosmological constraints and parameter dependencies by performing MCMC parameter estimation with different datasets using a modified version of the Einstein-Boltzmann solver CAMB described in the Appendix B.2. All of the cosmology models we test have the six standard ΛCDM parameters plus the MG parameters which vary in different tests. The six ΛCDM parameters have standard priors and we fix the sum of neutrino masses to the minimal value [37].

Since the MG parameters are introduced as phenomenological triggers for new physics in the datasets, our strategy for dataset and parameter choices is to look for datasets that

are in tension with the well-measured CMB temperature power spectrum under the ΛCDM model and to investigate the simplest MG case that might relax that tension.

Since the leading tensions under ΛCDM involve H_0 and galaxy Weak Lensing (WL), we highlight these in the studies below. If MG parameters can relax these tensions, we proceed to add other cosmological datasets to see if they can provide a consistent solution. We also consider joint variation of MG parameters to see if together they can resolve tensions better than individually.

This procedure employs several datasets. We begin with the measurements of the high multipole CMB temperature power spectrum from the *Planck* satellite [41, 42] supplemented by the low multipole TEB data which mainly constrains the optical depth τ. We refer to this baseline dataset as CMBTT. To this we add the high multipole EE and TE *Planck* data which we call CMBpol. We further employ the *Planck* 2015 full-sky lensing potential power spectrum [43] in the multipole range $40 \leq \ell \leq 400$. At smaller angular scales CMB lensing is strongly influenced by the non-linear evolution of dark matter perturbations, we thus exclude multipoles above $\ell = 400$. We refer to this dataset as CMBlens. We indicate the dataset joining all *Planck* CMB datasets as CMBall = CMBTT+CMBpol+CMBlens .

The H_0 tension is realized by the dataset consisting of local measurements of the Hubble constant derived by the "Supernovae, H0, for the Equation of State of dark energy" (SH0ES) team [187] and their best estimation is $H_0 = 73.24 \pm 1.74$ (in units of $\mathrm{km\,s^{-1}\,Mpc^{-1}}$ here and throughout). We refer to this dataset as H0.

On the other hand the WL tension leverages on the measurements of the galaxy weak lensing shear correlation function as provided by the Canada-France-Hawaii Telescope Lensing Survey (CFHTLenS) [188, 189]. This dataset is referred to as WL. We applied ultra-conservative cuts, that make CFHTLenS data insensitive to the modelling of non-linear evolution. We call the combination of CMBall+H0+WL = CMBtension.

Finally we include: BAO and RSD measurements of BOSS DR12 [45], SDSS Main Galaxy

Sample [46] and 6dFGS [47]; the "Joint Light-curve Analysis" (JLA) Supernovae sample [190]. We call the combination of CMBtension + BAO + SN = All.

5.6 Results

We begin with the discussion of late times modifications to gravity, parametrized with μ_0 and γ_0, and review why the preference for non-GR values appears for the CMB temperature spectrum but disappears once CMB lensing reconstruction is included. This case has been previously considered in the literature but we correct for a problem in some of the previous implementations. We then consider the early times modifications to gravity, as parametrized by μ_∞ and γ_∞, which constitute the truly new aspect of this work. We show that μ_∞ in particular can relax the tension with H_0 and WL by changing all CMB theoretical predictions in a compatible manner due to its combined effect near recombination and on lensing. However in our implementation where the background expansion is unmodified with respect to ΛCDM, BAO data in particular do not favor such a resolution. Finally we consider combinations of early and late time MG parameters to test whether non-trivial degeneracies appear and find that none of these combinations help to further reduce tensions.

5.6.1 Late time modified gravity

We first consider the joint effects of μ_0 and γ_0 since their individual effects are quite similar resulting in a strong degeneracy between the two parameters shown in Fig. 5.8. Our constraints on late time MG parameters are weaker than some of the results in the literature, especially in the degenerate direction, due to our more realistic and consistent treatment of the transition from GR at early times to these MG parameters, as discussed in Appendix B.3.

When the CMBTT dataset is considered alone, the late time parameters can also broaden its constraints on H_0 and $\sigma_8^{\rm WL}\Omega_m^{0.5}$ as shown in Fig. 5.8. In fact a deviation from $\mu_0 = \gamma_0 = 1$

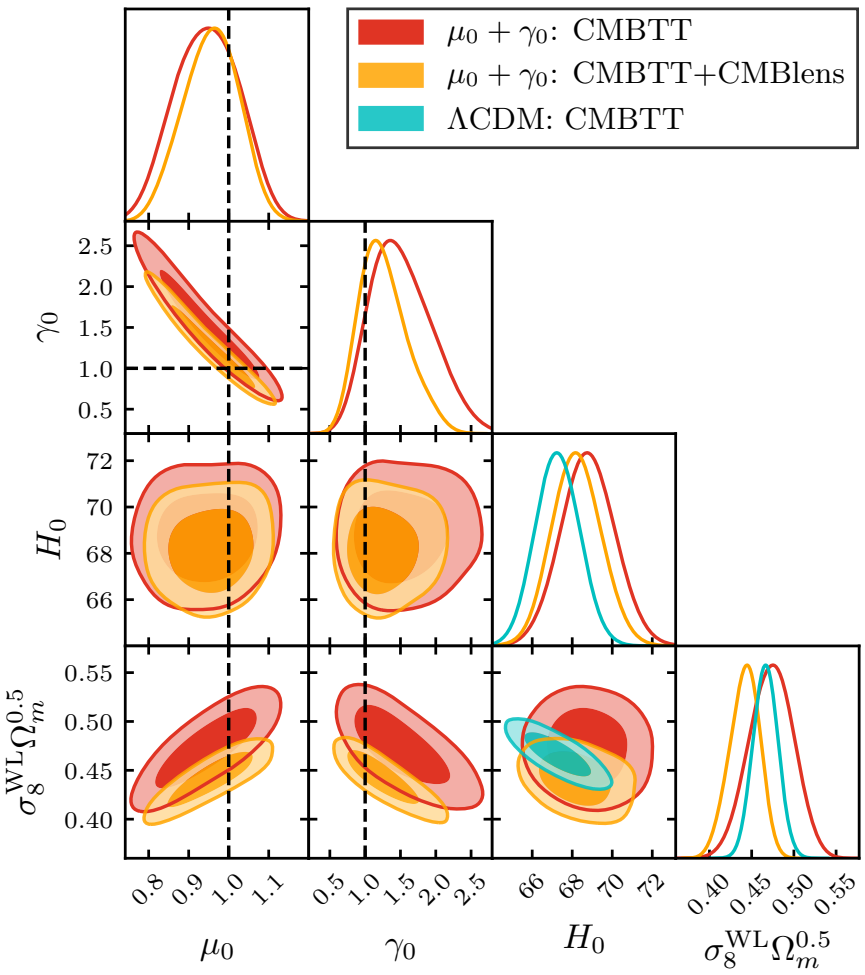

Figure 5.8: The marginalized joint posterior of the parameters of the late time MG model, μ_0+γ_0. ΛCDM results are also added for comparison. Different colors correspond to different combination of datasets, as shown in legend. The darker and lighter shades correspond respectively to the 68% C.L. and the 95% C.L. Dashed lines indicate the GR limit of the MG parameters.

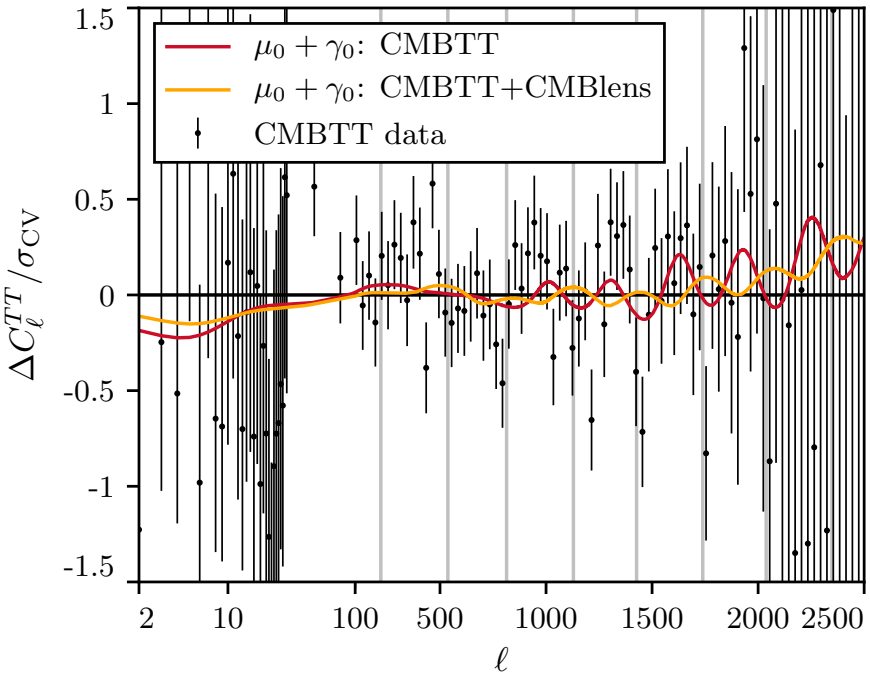

Figure 5.9: The *Planck* TT residuals for the best fit late time modified gravity model, relative to the best fit ΛCDM CMBTT model. The foreground parameters are fixed to the ΛCDM best fit values for compatibility with the foreground model removed from the data. Different colors correspond to different combination of datasets, as shown in legend. The residuals are normalized to $\sigma_{\rm CV}$, the cosmic variance per multipole of the best fit ΛCDM CMBTT model (see text). The vertical solid lines indicate the angular position of acoustic peaks of the unlensed spectrum in the ΛCDM model.

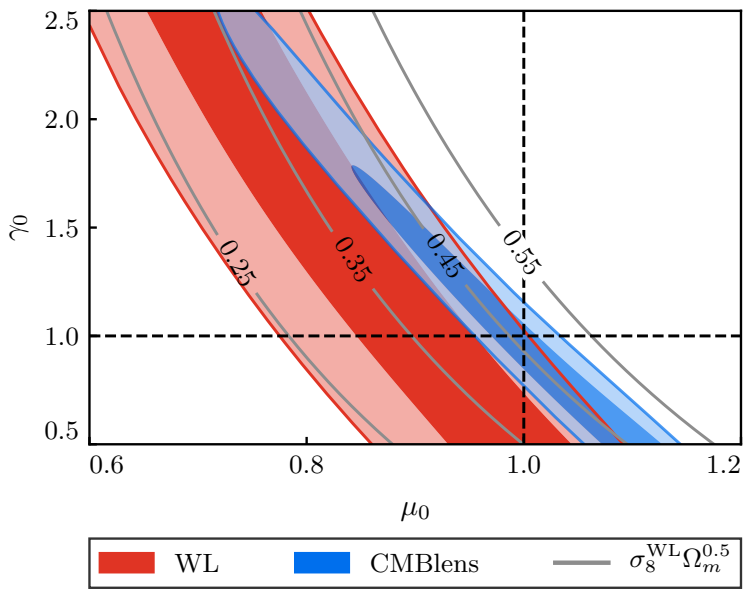

Figure 5.10: The WL-only and CMBlens-only constraints on μ_0 and γ_0 while keeping all other parameters fixed to their best fit ΛCDM values for CMBTT. The continuous lines show the iso-contours of $\sigma_8^{\rm WL}\Omega_m^{0.5}$. The darker and lighter shades correspond respectively to the 68% C.L. and the 95% C.L. Dashed lines indicate the GR limit of the MG parameters.

is preferred at the 95% C.L., as can be seen in Fig. 5.8.

These results are related to coherent features in the data residuals with respect to the ΛCDM best fit model to the CMBTT dataset (see Fig. 5.9). Here and below, we scale residuals to the cosmic variance per multipole

$$\sigma_{\rm CV}^{TT} = \sqrt{\frac{2}{2\ell+1}} C_\ell^{TT}\,, \tag{5.28}$$

$$\sigma_{\rm CV}^{TE} = \sqrt{\frac{1}{2\ell+1}\left[C_\ell^{TT}C_\ell^{EE}+(C_\ell^{TE})^2\right]}\,, \tag{5.29}$$

with C_ℓ^{TT}, C_ℓ^{EE} and C_ℓ^{TE} fixed to the best fit ΛCDM CMBTT model. The data exhibit residuals that are nearly in phase with the acoustic peaks at $\ell \gtrsim 1000$ which indicate smoother acoustic peaks in the data [191, 51, 192]. This smoothness is also what is responsible for changing the inferences for a higher H_0 at $\ell < 1000$ and a lower H_0 beyond, and conversely for $\sigma_8^{\rm WL}\Omega_m^{0.5}$ given that in ΛCDM, the acoustic peak positions fix $\Omega_c h^3$ approx-

imately. Furthermore the $\ell < 1000$ residuals are dominated by the low power glitch in the CMBTT data at $\ell \lesssim 30$, shown in Fig. 5.9, which explains their preference for a lower $\Omega_c h^2$ to enhance driving and a higher H_0. This preference was also seen in the WMAP dataset which was comparably limited by instrumental resolution [191].

It is well known that these oscillatory residuals can be better fit with a higher CMB lensing amplitude than ΛCDM implies [41] and this explains the preference for MG at about the same statistical significance. In Fig. 5.9, we can see that the best fit MG parameters better accommodate the oscillatory residuals while not decreasing the agreement of the model with data below $\ell \lesssim 1000$. Here and below, when showing the *Planck* CMB best fit MG models we fix foreground parameters to their best fit ΛCDM values for compatibility with the data points that have that model subtracted. On the other hand, all constraints on MG parameters have the standard foreground parameters marginalized over.

Because of these oscillatory residuals, MG allows for a lower $\Omega_c h^2$, which also fits better the low power glitch at $\ell \lesssim 30$, to be compatible with CMBTT and hence accommodates a higher H_0 and higher $\sigma_8^{\rm WL}\Omega_m^{0.5}$, where the latter reflects the fact that raising CMB lensing tends to raise WL as well.

However it is also well known that CMBlens data do not favor raising the lensing amplitude to explain the oscillatory residuals in CMBTT [41] and in fact no changes in the amplitude or shape of the lens power spectrum $C_\ell^{\phi\phi}$ can reconcile them [193, 194]. Consequently, once the CMBlens data are added the constraints on μ_0 and γ_0 become compatible with the GR values and the ability to raise H_0 is diminished (see Fig. 5.8). Likewise the ability to fit the oscillatory residuals in Fig. 5.9 also goes away.

Furthermore, the WL dataset also favor lowering not raising lensing and so would also counter the ability of MG to fit the CMBTT oscillatory residuals. We can see this more directly in Fig. 5.10 where we consider the constraints from the CMBlens and WL datasets alone but fix the ΛCDM parameters to their best fit CMBTT values for ΛCDM. Note that

the CMBlens and WL constrain nearly the same combination of μ_0 and γ_0 with WL favoring somewhat lower values and hence somewhat less lensing. The CMBlens data are fully consistent with the GR values whereas the WL data prefer lower values, reflecting the tension between the CMBTT and WL datasets. Therefore the tensions between CMBTT, CMBlens and WL data sets cannot be resolved by raising lensing with late time MG parameters alone. Notice also that contours of $\sigma_8^{\rm WL}\Omega_m^{0.5}$ track the degenerate direction of the WL constraints and justify its use as a proxy for the WL lensing observable.

5.6.2 Early time modified gravity

The oscillatory residuals in the CMBTT data vs. a high H_0 solution cannot be explained by introducing new physics through MG to change the smoothing of the peaks by gravitational lensing since the CMBlens dataset forbids it. This leaves the possibility that the early time MG can change the intrinsic shape of the peaks and resolve these tensions. Furthermore since the study of the early time parameters μ_∞ and γ_∞ is new to this work, we conduct a more thorough examination of their individual effects than in the previous section on late time parameters.

We start with μ_∞ alone and the CMBTT dataset in Fig. 5.11. Here μ_∞ is strongly correlated with θ_*. This is because μ_∞ leads to a phase shift in the acoustic peaks and its effect on the well-measured peak locations is partially degenerate with a change in the angular scale of the sound horizon (see Sec. 5.4.1). Since the CMBTT dataset measures multiple peaks, the degeneracy is not perfect and indeed the measurement of the peak locations provides the strongest constraint on μ_∞. Note also that within ΛCDM the best fit value of θ_* shifts between $\ell \lesssim 1000$ and the full dataset to lower values by $\sim 1\sigma$ [51]. In the μ_∞ model, this shift in peak locations can be accommodated by a change in both the angular scale and phase of the acoustic peaks.

A larger value for μ_∞ also allows a larger value of H_0. In GR with the ΛCDM H_0 =

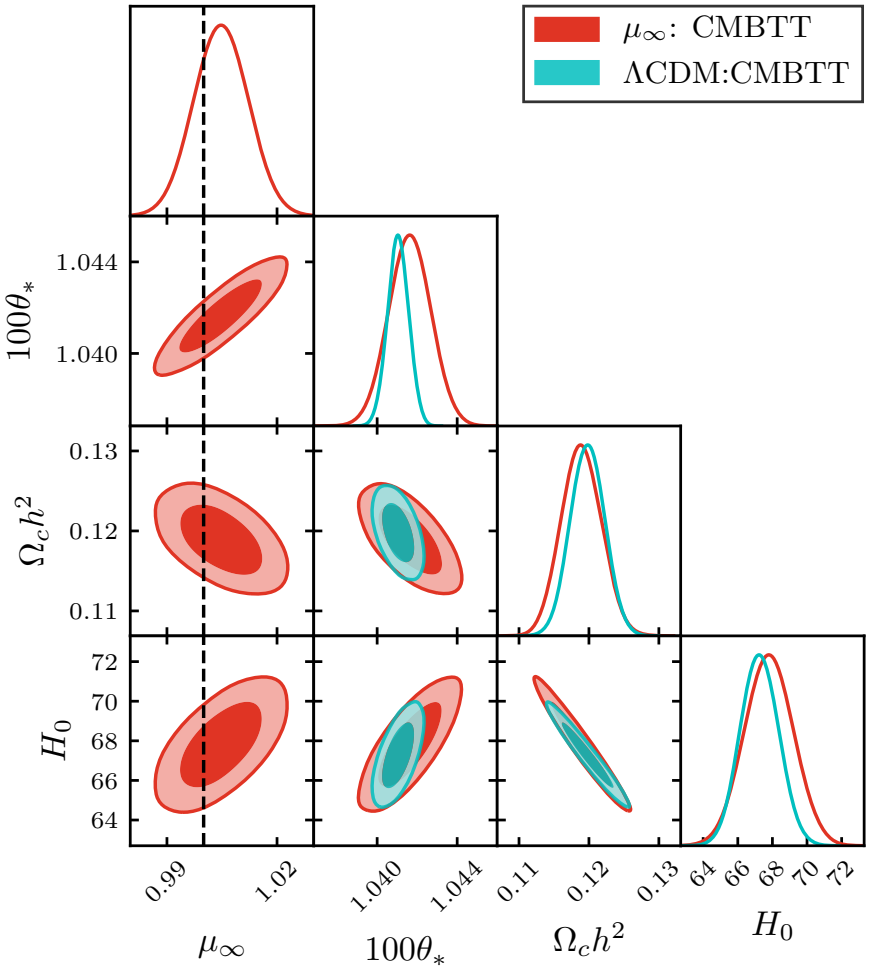

Figure 5.11: The CMBTT constraints on the cosmological parameters in the μ_∞ only model. Results of ΛCDM model are also added for comparison. The darker and lighter shades correspond respectively to the 68% C.L. and the 95% C.L. Dashed lines indicate the GR limit of the MG parameters.

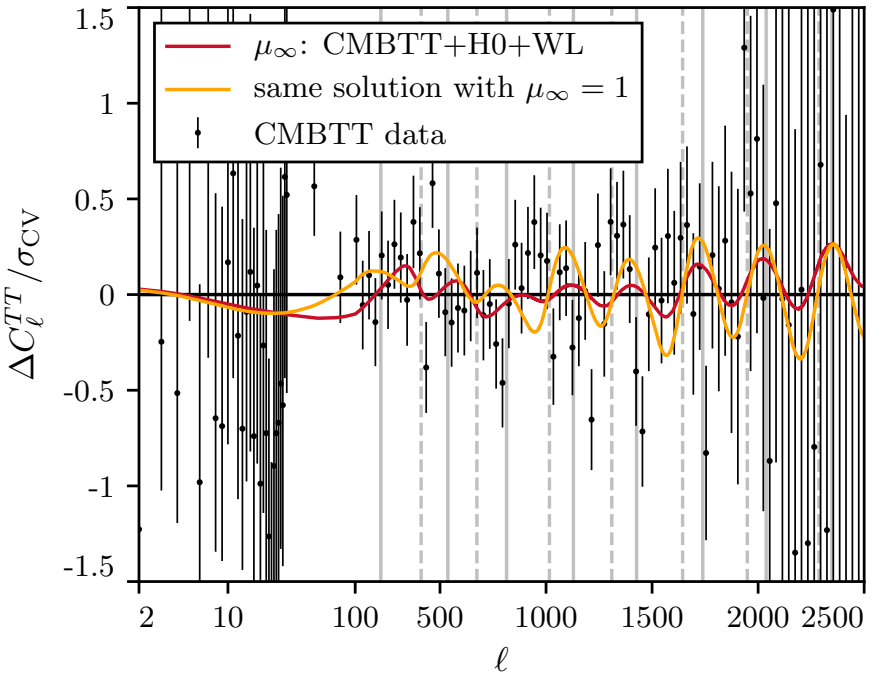

Figure 5.12: TT residuals relative to the best fit ΛCDM CMBTT model, similar to Fig. 5.9 but with the best fit μ_∞-only model to CMBTT+H0+WL datasets with $H_0 \approx 70$ (red line). A model with the same cosmological parameters but $\mu_\infty = 1$ (orange line) shows that μ_∞ compensates for the oscillatory fluctuations of the high H_0 model that are disfavored by the data.

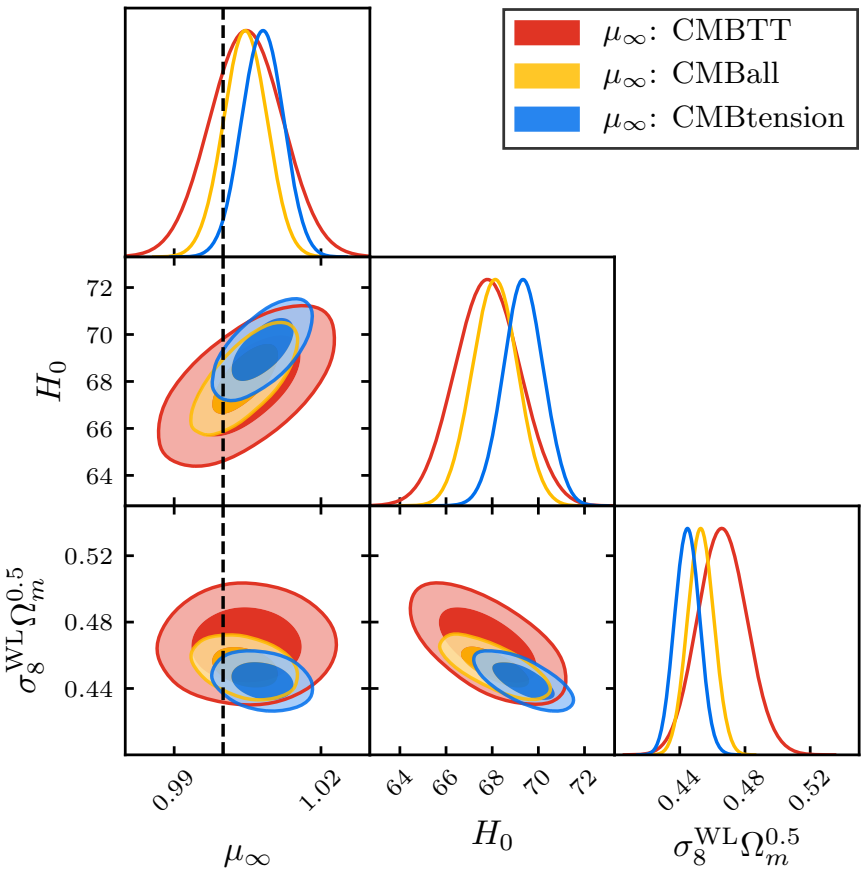

Figure 5.13: The marginalized joint posterior for the parameters in the μ_∞ only model. Different colors correspond to different combination of datasets, as shown in legend. The darker and lighter shades correspond respectively to the 68% C.L. and the 95% C.L. The dashed lines indicate the value of μ_∞ in GR limit.

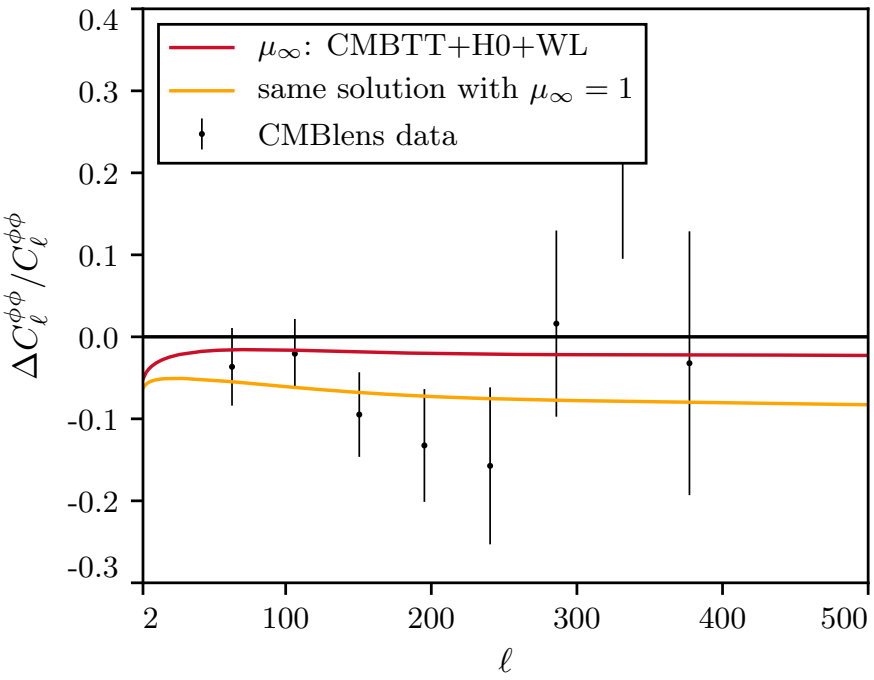

Figure 5.14: CMB lens power spectrum residuals relative of the μ_∞ only model to the best fit ΛCDM CMBTT model. The models are the same as in Fig. 5.12 as also shown in the legend. Again μ_∞ compensates the changes due to the larger H_0 value.

67.26 ± 0.99. Within the bounds on μ_∞ allowed by the phase shift, $H_0 = 67.80 \pm 1.27$. This comes about since μ_∞ allows another way of changing the amount of low to high ℓ TT power, especially around the first few acoustic peaks, and so is partially degenerate with radiation driving effects from $\Omega_c h^2$ and also another way of compensating the reduction in lensing due to a lower $\Omega_c h^2$. Notice that the the correlation of the latter with H_0 remains largely unchanged since the background expansion remains identical to ΛCDM and θ_s remains well constrained. This has implications for BAO and SN as we shall see, since raising H_0 requires the same reduction in Ω_m as in ΛCDM. Note that as in ΛCDM a higher H_0 solution also gives a lower $\sigma_8 \Omega_m^{0.5}$ which is favored by WL data.

We can see these effects in Fig. 5.12. Here we show how μ_∞ compensates for changes in the cosmological parameters of a high $H_0 = 69.9$ best fit solution to the CMBTT+H0+WL datasets. Notice that with the same cosmological parameters but reverting $\mu_\infty = 1$, the

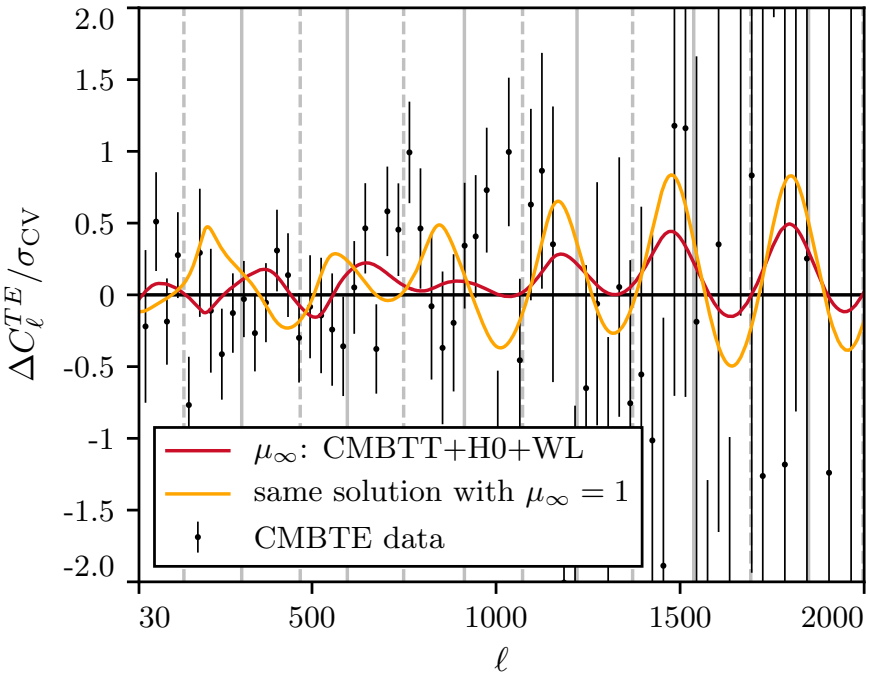

Figure 5.15: TE residuals relative to the best fit ΛCDM CMBTT model, similar to Fig. 5.12 but with TE spectrum. Again μ_∞ compensates the changes due to the larger H_0 value especially around the first minimum where the data also fluctuate low (leftmost vertical line).

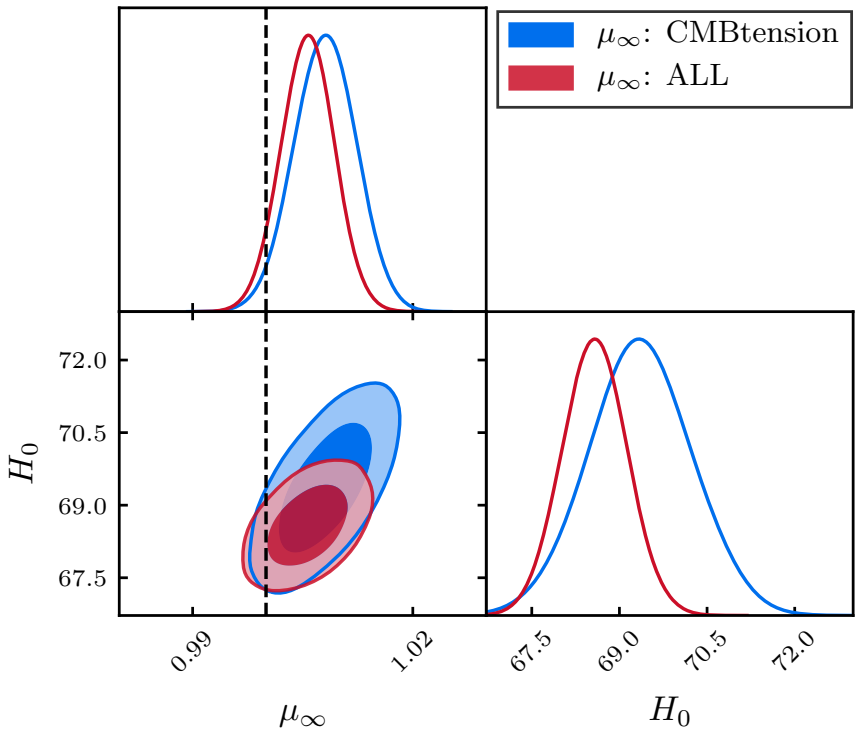

Figure 5.16: The marginalized joint posterior for μ_∞ and H_0 in the μ_∞ only model. Different colors correspond to different combination of datasets, as shown in legend. The darker and lighter shades correspond respectively to the 68% C.L. and the 95% C.L. The dashed lines indicate the value μ_∞ in GR limit.

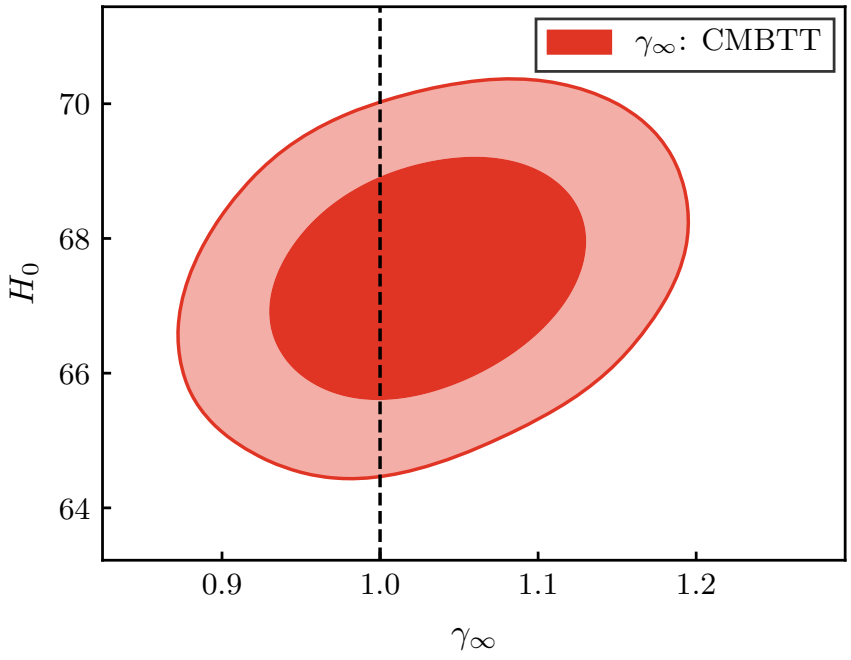

Figure 5.17: The marginalized joint posterior for γ_∞ and H_0 in the γ_∞ only model with the CMBTT dataset. The darker and lighter shades correspond respectively to the 68% C.L. and the 95% C.L. The dashed lines indicate the value γ_∞ in GR limit where nearly the same range in H_0 is allowed.

model exacerbates the oscillatory residuals in the data at $\ell \gtrsim 1000$, the well-known problem with raising H_0 under ΛCDM.

While this broadening and raising of H_0 values allowed by CMBTT with μ_∞ is small but significant in that it places $H_0 = 70$ well within the CMBTT 2σ bound, the main benefit of μ_∞ over the late time parameters is that CMBlens and CMBpol data somewhat favor rather than disfavor such a deviation from GR. In Fig. 5.13, we show the result of the CMBall combination. Notice that the errors on μ_∞ shrink but the central value remains the same. After adding H0 and WL datasets, we end at $H_0 = 69.35 \pm 0.80$. and a preference for $\mu_\infty > 1$ at the 98.2% C.L. This preference comes about since the effect of raising μ_∞ and lowering $\Omega_c h^2$ nearly compensate each other in their effect on the CMB lens power spectrum as shown in Fig. 5.14 for the same model as in Fig. 5.12. For the polarization, in ΛCDM a low H_0 value is preferred in large part due to the low TE datapoint around the first minimum ($\ell \sim 165$) [192]. This too is compensated with μ_∞ and together with changes at higher multipole in fact brings about a better fit than ΛCDM in Fig. 5.15.

On the other hand since in our parameterization the background expansion remains ΛCDM, the lower Ω_m implied by a higher H_0 causes tension with the BAO dataset. After adding BAO dataset, $H_0 = 68.57 \pm 0.50$, disfavoring high values, and the preference for $\mu_\infty > 1$ is reduced to 95.7% C.L. (see Fig. 5.16). In a physically motivated MG theory, we would typically expect both the background and the perturbations to be modified and so in principle this problem with BAO could be ameliorated by changing the expansion rate in a manner similar to adding extra relativistic degrees of freedom under GR.

Next, we discuss the results with γ_∞ as the only MG parameter. With the CMBTT dataset, similar to μ_∞, γ_∞ also causes a phase shift, so it is also constrained by the locations of acoustic peaks. However, γ_∞ only shows a very weak correlation with H_0 in Fig. 5.17 and cannot move H_0 much higher than in ΛCDM. Its effects at recombination share some similarity to μ_∞ in that raising it alters the power between low and high multipoles and

accommodates a lower $\Omega_c h^2$ and higher H_0. However raising γ_∞ also lowers the CMB lens power spectrum as shown in Fig. 5.5 and exacerbates the oscillatory residual problem at $\ell \gtrsim 1000$.

Finally, with both μ_∞ and γ_∞ as MG parameters, a strong correlation between μ_∞ and γ_∞ shows up when CMBTT data is considered. This also come from the phase shift effect. Since both μ_∞ and γ_∞ shift the phase in the same direction and μ_∞ to compensate each other, they show a negative correlation with a direction consistent with the amplitudes of their phase shifts discussed above. Because of this anti-correlation their joint ability to ameliorate H_0, CMBlens and WL tensions is not significantly greater than that of μ_∞ alone.

5.6.3 Combined early and late times MG

At last we consider combinations of MG parameters together to check whether non-trivial degeneracies appear.

When we use both μ_∞ and μ_0 as MG parameters, the H_0 tension can be further reduced when CMBTT data is considered. But for the same reasons that we discussed in Sec. 5.6.1, this resolution is also disfavored by CMBlens because of the enhancement of the lensing potential, see Fig. 5.18.

On the other hand, when we use both γ_∞ and γ_0 as the MG parameters, we find that there is no correlation between them, see Fig. 5.19. Both parameters affect the CMB temperature spectrum in independent ways and both parameters are then not favored by the data as we discussed in the previous sections.

5.7 Discussion

We study the impacts of MG on cosmological perturbation evolution and CMB power spectrum under a phenomenological parameterization of the Poisson equations (5.7, 5.8). We implement this parameterization into the Einstein-Boltzmann code CAMB.

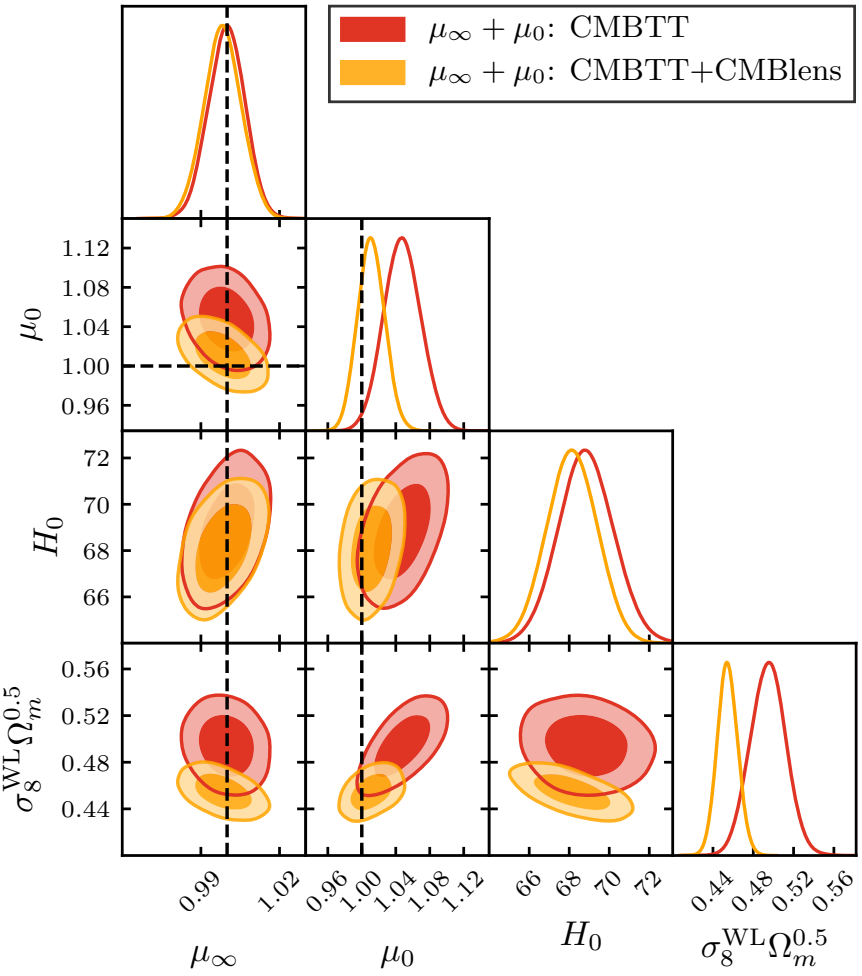

Figure 5.18: The marginalized joint posterior for the parameters in the $\mu_\infty + \mu_0$ only model. Different colors correspond to different combination of datasets, as shown in legend. The darker and lighter shades correspond respectively to the 68% C.L. and the 95% C.L. The dashed lines indicate the values of the MG parameters in the GR limit.

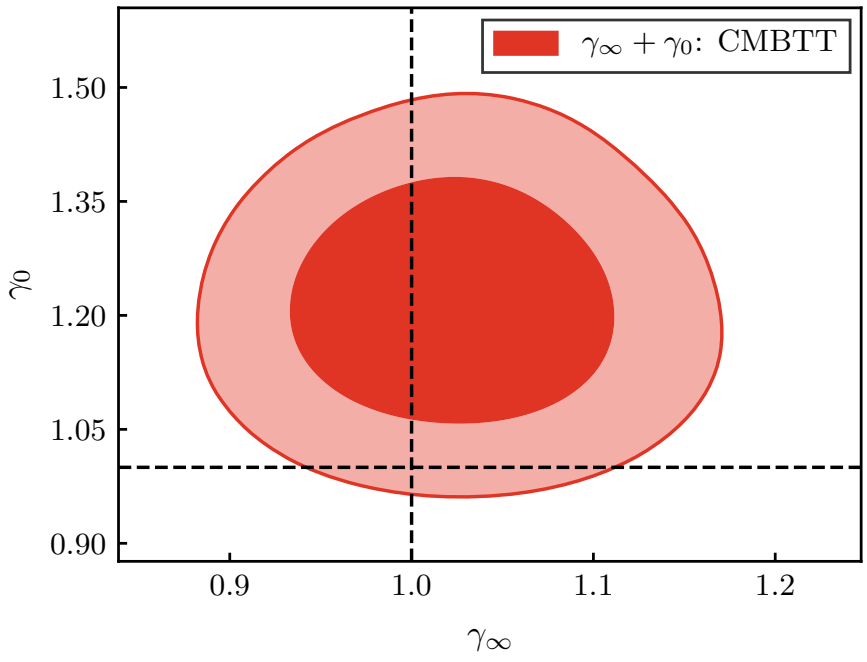

Figure 5.19: The marginalized joint posterior for γ_∞ and γ_0 in the $\gamma_\infty + \gamma_0$ model with the CMBTT dataset. The darker and lighter shades correspond respectively to the 68% C.L. and the 95% C.L. The dashed lines indicate the values of the MG parameters in the GR limit.

New aspects of this work include the treatment of initial conditions in the radiation dominated epoch and the effect of MG on the CMB and matter evolution prior to recombination. In particular, we illustrate the MG effects using step functions of time for the two MG perturbation parameters with an unmodified ΛCDM background to isolate their effects at early and late times.

This study is partially motivated by the existence of tensions between CMB and low redshift observables in ΛCDM. For the late time MG parameters μ_0 and γ_0, the non-GR values are favored by CMBTT data because the MG parameters raise the lensing potential and smooth the acoustic peaks while also raising the Hubble constant H_0. However, this preference disappears once CMBlens data is included because the lensing reconstruction does not favor such an enhancement. We conclude that late time modifications alone are unlikely to resolve tensions with ΛCDM.

Parameter tensions in ΛCDM rely heavily on the interpretation of acoustic observables in the CMB and BAO at recombination. By changing the evolution of gravitational potentials, MG parameters at early times can in principle be more effective. While changing γ_∞ can not help to reduce tensions, changing μ_∞ can relax tensions internal to the CMB datasets and between CMBTT and H_0 and weak lensing. This is achieved by changing CMB temperature, polarization and lensing predictions in a compatible manner due to its combined effect on the acoustic oscillations and on lensing and results in a preference for $\mu_\infty > 1$ at greater than 98% C.L. and $H_0 = 69.35 \pm 0.80$ when combined with Hubble constant and weak lensing datasets. BAO data however do not favor such a resolution since the background expansion remains unchanged compared to ΛCDM in our implementation and therefore requires a lower Ω_m for a higher H_0. Combinations with other MG parameters do not further help resolve tensions.

In a physically motivated modification of gravity, we would generally expect changes to both the background and the perturbations, leaving open the possibility that once combined

this tension with BAO can be ameliorated as well. Moreover, our simple parameterization of MG in the perturbations with a step function in time is itself only meant to be illustrative and not a prediction based on a fundamental theory. Instead this study serves as a guide to the construction of physically motivated models that might resolve tensions in ΛCDM. We leave such studies to a future work.

CHAPTER 6

CONCLUSION

As the Hubble tension has increased steadily with the increasing experimental precision, it has become one of the biggest mysteries in modern cosmology. This thesis provides some thoughts of the physical solutions for the Hubble tension including EDE-like models and early modified gravity, although we have not found the perfect solution so far.

I hope the examples presented in this thesis could at least give the reader some useful hints for the paths towards the correct solution (if Hubble tension is real). In the future, if an EDE-like background expansion history (which is not necessarily realized by a scalar field, could also by e.g. certain modified gravity theories) still looks promising resolve the Hubble tension, there are still some degrees of freedom to adjust in the perturbation level by introducing dark interaction or dark force. The upcoming CMB polarization measurements in the near future would provide more sensitive information for this problem.

APPENDIX A

THE EARLY DARK SECTOR, THE HUBBLE TENSION, AND THE SWAMPLAND

A.1 Equations of Motion

We consider cold dark matter interacting with the EDE scalar field ϕ. We model dark matter as a population of non-relativistic Dirac fermions. We consider a model with action given by,

$$S = \int d^4x\sqrt{-g}\left[\frac{1}{3M_{\rm pl}^2}R - \frac{1}{2}\partial^\mu\phi\partial_\mu\phi - i\bar{\psi}\not{D}\psi - V(\phi) - m_{\rm DM}(\phi)\bar{\psi}\psi + h.c.\right]. \tag{A.1}$$

where ψ is a Dirac fermion, which plays the role of cold dark matter. As such, we take the non-relativistic limit of ψ, in which case $\langle\bar{\psi}\psi\rangle \to n(t)$, where $n(t)$ is the number density, namely, the total number of particles and anti-particles, not to be confused with $\langle\bar{\psi}\gamma^0\psi\rangle$, which is the *difference* between the number of particles and antiparticles. In this limit, the dark matter component is described by a stress tensor,

$$T^{(\rm DM)\mu}{}_\nu = n_{\rm DM}m_{\rm DM}(\phi)u^\mu u_\nu \tag{A.2}$$

with $u^\mu = (-1, v^i)$. This comprises only a part of the stress tensor of the full interacting system, which is given by

$$T_{\mu\nu} = T_{\mu\nu}^{(\rm DM)} + T_{\mu\nu}^{(\phi)}, \tag{A.3}$$

where $T_{\mu\nu}^{(\phi)}$ is the ϕ contribution given by

$$T^{(\phi)\mu}{}_\nu = \partial^\mu\phi\partial_\nu\phi - \frac{1}{2}\delta^\mu{}_\nu\partial^\alpha\phi\partial_\alpha\phi - \delta^\mu{}_\nu V(\phi). \tag{A.4}$$

The combined stress tensor is covariantly conserved,

$$\nabla_\mu T^\mu{}_\nu = 0, \tag{A.5}$$

which follows from the contracted Bianchi identities of General Relativity. The equations of motion of the interacting system are dictated by the conservation equation Eq. (A.5) along with the equations of motion for the scalar field that follow from the variation of the action.

The equations of motion for the scalar field background and perturbations are given by the variation of the action expanded to linear and quadratic order in $\delta\phi$ respectively. At the background level, where quantities depend only on time, the variation with respect to the scalar field gives,

$$\ddot{\phi} + 2aH\dot{\phi} + a^2\frac{dV}{d\phi} + a^2 n\frac{dm_{\rm DM}}{d\phi} = 0, \tag{A.6}$$

where dot denotes a derivative with respect to conformal time τ, while H is defined with respect to time t. This can be expressed in terms of the dark matter energy density as,

$$\ddot{\phi} + 2aH\dot{\phi} + a^2\frac{dV}{d\phi} + a^2\frac{d\log m_{\rm DM}}{d\phi}\rho_{\rm DM} = 0. \tag{A.7}$$

The equation of motion for the dark matter density is given by

$$\dot{\rho}_{\rm DM} + 3aH\rho_{\rm DM} = \dot{\phi}\frac{d\log m_{\rm DM}}{d\phi}\rho_{\rm DM}. \tag{A.8}$$

We repeat this procedure for the perturbations, working in the synchronous gauge. The metric in synchronous gauge is given in general by

$$ds^2 = a^2(\tau)\left(-d\tau^2 + (\delta_{ij} + h_{ij})dx^i dx^j\right). \tag{A.9}$$

The perturbation h_{ij} may be decomposed into two scalar degrees of freedom, h and η, defined

by the decomposition,

$$h_{ij}(\vec{x},\tau) = \int d^3k e^{i\vec{k}\cdot\vec{x}} \left[\hat{k}_i\hat{k}_j h(\vec{k},\tau) + (\hat{k}_i\hat{k}_j - \frac{1}{3}\delta_{ij})\, 6\eta(\vec{k},\tau) \right] \tag{A.10}$$

where $\vec{k} = k\hat{k}$. See, e.g., [195], for more details.

The interaction of the scalar field with dark matter generates new terms in the quadratic action for perturbations, which are given by,

$$\delta S_2 = -\int d\tau d^3x\, a^4(\tau) \left[\frac{d^2 m_{\rm DM}}{d\phi^2}\delta\phi^2 n + \frac{dm_{\rm DM}}{d\phi}\delta\phi\delta n \right], \tag{A.11}$$

where δn is the perturbation to the dark matter number density. The resulting equation of motion is,

$$\ddot{\delta\phi} + 2aH\dot{\delta\phi} + \left(k^2 + a^2\frac{d^2V}{d\phi^2}\right)\delta\phi + \frac{1}{2}\dot{h}\dot{\phi} = -a^2\left[\frac{d\log m}{d\phi}\rho_{\rm DM}\delta_c + \frac{d^2\log m}{d\phi^2}\delta\phi\rho_{\rm DM}\right], \tag{A.12}$$

where we define the fractional dark matter density perturbation $\delta_c \equiv (\delta\rho_{\rm DM})/\rho_{\rm DM}$.

To derive the equations of motion for the dark matter component, we now explicitly evaluate Eq. A.5, and apply the scalar field equations of motion. From the $\nu = 0$ component, we find the equation of motion for δ_c, given by

$$\dot{\delta}_c + \theta + \frac{\dot{h}}{2} = \frac{d\log m}{d\phi}\dot{\delta\phi} + \frac{d^2\log m}{d\phi^2}\dot{\phi}\delta\phi, \tag{A.13}$$

while from the $\nu = i$ component we find the equation of motion for the velocity perturbations,

$$\dot{\theta} + aH\theta = +\frac{d\log m}{d\phi}k^2\delta\phi - \frac{d\log m}{d\phi}\dot{\phi}\theta. \tag{A.14}$$

where $\theta \equiv \partial_i v^i$.

A.2 Scalar-Mediated Force on Dark Matter

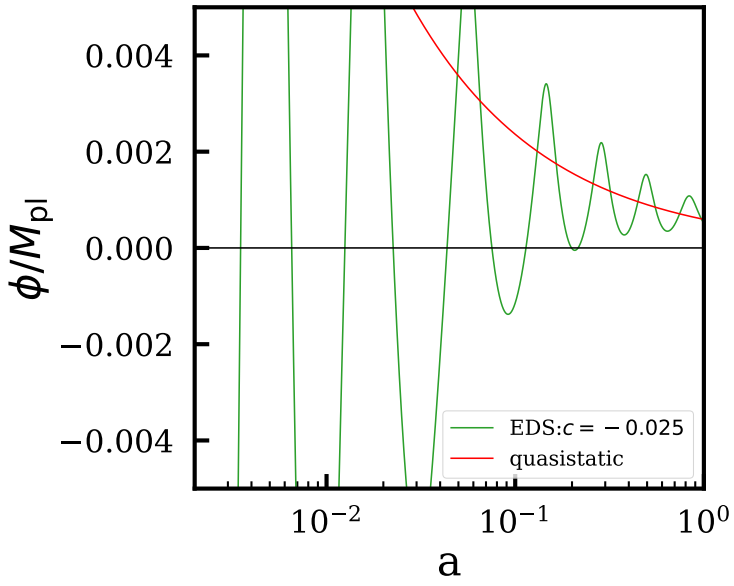

Figure A.1: Scalar field ϕ evolution for $c = -0.025$ with fixed H_0 and all other parameters (except θ_s) fixed to their values in Eqs. (4.17) and (4.18). The quasistatic estimation Eq. (A.24) is also shown for comparison.

To assess the combined gravitational and scalar mediated forces on the dark matter we start with the time-time and trace of the space-space pieces of the Einstein equation with the synchronous metric of Eq. (A.9)

$$\mathcal{H}\frac{\dot{h}}{2} = k^2\eta + \frac{1}{2M_{\rm pl}^2}a^2\delta\rho, \tag{A.15}$$

$$\frac{\ddot{h}}{2} + \mathcal{H}\dot{h} - k^2\eta = -\frac{3}{2M_{\rm pl}^2}a^2\delta P \tag{A.16}$$

and combine them to eliminate η:

$$\frac{\ddot{h}}{2} + \mathcal{H}\frac{\dot{h}}{2} = -\frac{1}{2M_{\rm pl}^2}a^2(\delta\rho + 3\delta P). \tag{A.17}$$

Taking the derivative of the dark matter continuity equation, Eq. (A.13), and plugging in $\ddot{h}$

from above and $\dot{\theta}$ from the Euler equation (A.14), we arrive at,

$$\ddot{\delta}_c - \mathcal{H}(\frac{\dot{h}}{2} + \theta_c) = \frac{1}{2M_{\rm pl}^2}a^2(\delta\rho + 3\delta P) - \frac{1}{M_{\rm pl}}ck^2\delta\phi + \frac{1}{M_{\rm pl}}c\dot{\phi}\theta_c + \frac{1}{M_{\rm pl}}c\ddot{\delta\phi}. \tag{A.18}$$

To gain physical intuition, we consider a quasistatic limit in which the last term in the above can be neglected. For small c the second last term is in higher order of c. Note that there is a non-zero offset value for $\delta\phi$ at late times. From the equation of motion

$$\ddot{\delta\phi} + 2aH\dot{\delta\phi} + (k^2 + a^2\frac{d^2V}{d\phi^2})\delta\phi + \frac{1}{2}\dot{h}\dot{\phi} = -a^2\frac{1}{M_{\rm pl}}c\delta\rho_{\rm DM}, \tag{A.19}$$

we can estimate $\delta\phi$ in the quasistatic limit as

$$\delta\phi^{(0)} \approx -a^2\frac{c\delta\rho_{DM}/M_{\rm pl}}{k^2 + a^2d^2V/d\phi^2}, \tag{A.20}$$

We then plug it into Eq. (A.18) and, assuming $\delta\rho + \delta P$ is dominated by dark matter, we have,

$$\ddot{\delta}_c + \mathcal{H}\dot{\delta}_c = 4\pi Ga^2\rho_c\delta_c(1 + \frac{2c^2k^2}{k^2 + a^2d^2V/d\phi^2}). \tag{A.21}$$

From this one may read off an effective gravitational constant,

$$G_{\rm eff} = G_N\left(1 + \frac{2c^2k^2}{k^2 + a^2d^2V/d\phi^2}\right), \tag{A.22}$$

which is independent of the sign of c.

Notice that the modification to $G_{\rm eff}$ appears on scales below the Compton wavelength of the scalar $k/a > d^2V/d\phi^2$ which itself depends on the dark matter density. The scalar field oscillates around the minimum of the effective potential which evolves quasistatically as

$$\frac{dV}{d\phi} = -\frac{c}{M_{\rm pl}}\rho_{\rm DM} \tag{A.23}$$

to be

$$\phi = -\mathrm{sgn}(c)\frac{2^{2/5}c^{1/5}f^{4/5}\rho_{\rm DM}^{1/5}}{3^{1/5}m^{2/5}M_{\rm pl}^{1/5}}. \tag{A.24}$$

At the minimum the scalar mass is

$$m_\phi = \left(\frac{d^2V}{d\phi^2}\right)^{1/2} = \frac{3^{1/10}5^{1/2}c^{2/5}m^{1/5}\rho_{\rm DM}^{2/5}}{2^{1/5}f^{2/5}M_{\rm pl}^{2/5}}. \tag{A.25}$$

In Fig. A.1 we show the late time evolution of the scalar field for model with $c = -0.025$ with fixed H_0 and all other parameters (except θ_s) fixed to their values in Eqs. (4.17) and (4.18). We see that the quasistatic estimation agrees well with the DC offset of the scalar field. The corresponding Compton wavelength at the minimum at $z = 0$ is $\sim 1\,\mathrm{Gpc}$ so that for scales relevant to large-scale structure, $G_{\rm eff} \approx G_N(1 + 2c^2)$. Notice also that the scaling of the range of the modified force is a fairly mild $\rho_{\rm DM}^{-2/5}$. Although EDS admits chameleon screening of the force in a high density environment, even in a virialized halo where the local density is ~ 200 times the background, the range remains large compared with both the scale of the halo and the large-scale structure relevant to S_8.

A.3 Implementation In CLASS

We implement the EDS model into the publicly available Boltzmann code CLASS [137, 138],[1] by modifying the publicly-available CLASS_EDE [2].[2]

We use the synchronous gauge functionality of CLASS to solve the Einstein equations, Eq. (21) of [195], given the energy density, pressure, and velocity of the matter content. From the stress tensor Eq. (A.4), the energy density and pressure of the scalar field are given

1. http://class-code.net
2. https://github.com/mwt5345/class_ede

by,

$$\begin{aligned} \rho_\phi &= \frac{1}{2a^2}\dot{\phi}^2 + V(\phi), \\ p_\phi &= \frac{1}{2a^2}\dot{\phi}^2 - V(\phi). \end{aligned} \tag{A.26}$$

The perturbations to the above, along with the scalar field velocity perturbation, are given by,

$$\begin{aligned} \delta\rho_\phi &= \frac{1}{a^2}\dot{\phi}\dot{\delta\phi} + V'(\phi)\delta\phi. \\ \delta p_\phi &= \frac{1}{a^2}\dot{\phi}\dot{\delta\phi} - V'(\phi)\delta\phi. \\ (\rho_\phi + p_\phi)v_\phi &= \frac{1}{a^2}k\dot{\phi}\delta\phi. \end{aligned} \tag{A.27}$$

We note that `CLASS` works in units wherein the energy density and pressure are rescaled by $1/3M_{\rm pl}^2$, i.e., the stress-energy tensor is rescaled as,

$$T_{\mu\nu}^{(\rm CLASS)} = \frac{1}{3M_{\rm pl}^2}T_{\mu\nu}. \tag{A.28}$$

The scalar field retains units of $M_{\rm pl}$. The above rescaling manifests in `CLASS` as a factor of (1/3) in the `CLASS` definition of ρ_ϕ, p_ϕ, etc. , relative to Eqs. (A.26) and (A.27).

The scalar field background equation of motion becomes,

$$\ddot{\phi} + 2aH\dot{\phi} + a^2\frac{dV}{d\phi} + 3a^2\frac{d\log m_{\rm DM}}{d\phi}\rho_{\rm DM}^{(\rm CLASS)} = 0 \tag{A.29}$$

where $\rho_{\rm DM}^{(\rm CLASS)}$ is in CLASS units. The perturbed Klein-Gordon equation becomes,

$$\begin{aligned} &\ddot{\delta\phi} + 2aH\dot{\delta\phi} + \left(k^2 + a^2\frac{d^2V}{d\phi^2}\right)\delta\phi + \frac{1}{2}\dot{h}\dot{\phi} = \\ &-3a^2\left[\frac{d\log m}{d\phi}\rho_{\rm DM}^{(\rm CLASS)}\delta + \frac{d^2\log m}{d\phi^2}\delta\phi\rho_{\rm DM}^{(\rm CLASS)}\right]. \end{aligned} \tag{A.30}$$

The covariant conservation of stress-energy may be expressed as

$$\nabla^{\mu}\left(T_{\mu\nu}^{(\mathrm{DM,CLASS})}+T_{\mu\nu}^{(\phi,\mathrm{CLASS})}\right)=0. \tag{A.31}$$

Propagating through the factors of 3 from the conversion to CLASS units, we find that the equations of motion of dark matter perturbations in CLASS units are unchanged from Eqs. (A.13) and (A.14).

The `CLASS_EDE` code [2] absorbs the cosmological constant Λ into the scalar field potential, as

$$V(\phi)=3M_{\mathrm{pl}}^{2}\Lambda+m^{2}f^{2}\left[1-\cos\frac{\phi}{f}\right]^{3} \tag{A.32}$$

where Λ is a constant. This rewriting utilizes the built-in functionality of CLASS to tune a parameter in $V(\phi)$ in order to satisfy the energy budget equation $\sum\Omega_i=1$ for arbitrary initial conditions for the scalar field. We impose slow-roll initial conditions on $\phi(t)$ and adiabatic initial conditions on $\delta\phi$, as discussed in [2]. Finally, in order to sample the EDE parameters f_{EDE} and $\log_{10}(z_c)$, we a shooting method to iteratively determine the corresponding model parameters f and m.

In this work we add to `CLASS_EDE` [2] a new cold (pressureless) dark matter component that is coupled to the EDE scalar as discussed above. We retain the `CLASS` cold dark matter component, with a fixed $\Omega_{\mathrm{cdm}}=10^{-5}$, in order to self-consistently define the synchronous gauge.

In order to simultaneously sample the present-day dark matter density and the scalar field initial conditions, we implement a shooting method to determine the initial dark matter density. We impose adiabatic initial conditions for the coupled dark matter component.

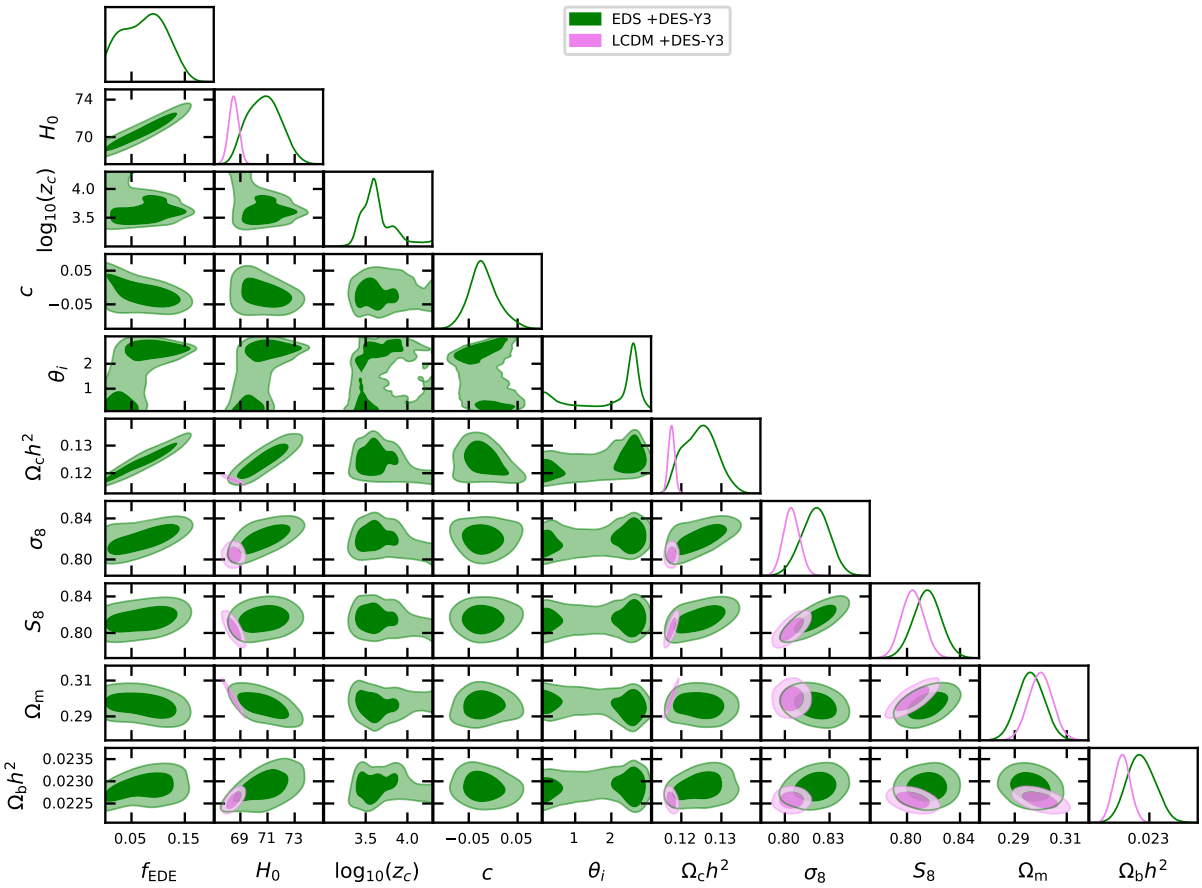

Figure A.2: Enlarged set of posterior distributions for the fit to the baseline data set (CMB, CMB lensing, BAO, SNIa, and SH0ES) supplemented with DES-Y3 data, approximated by a prior on S_8 for ΛCDM and EDS.

A.4 Additional Posterior Plots

The enlarged set of posterior distributions for the analysis with DES-Y3 data and with ACT data are given in Fig. A.2 and A.3, respectively.

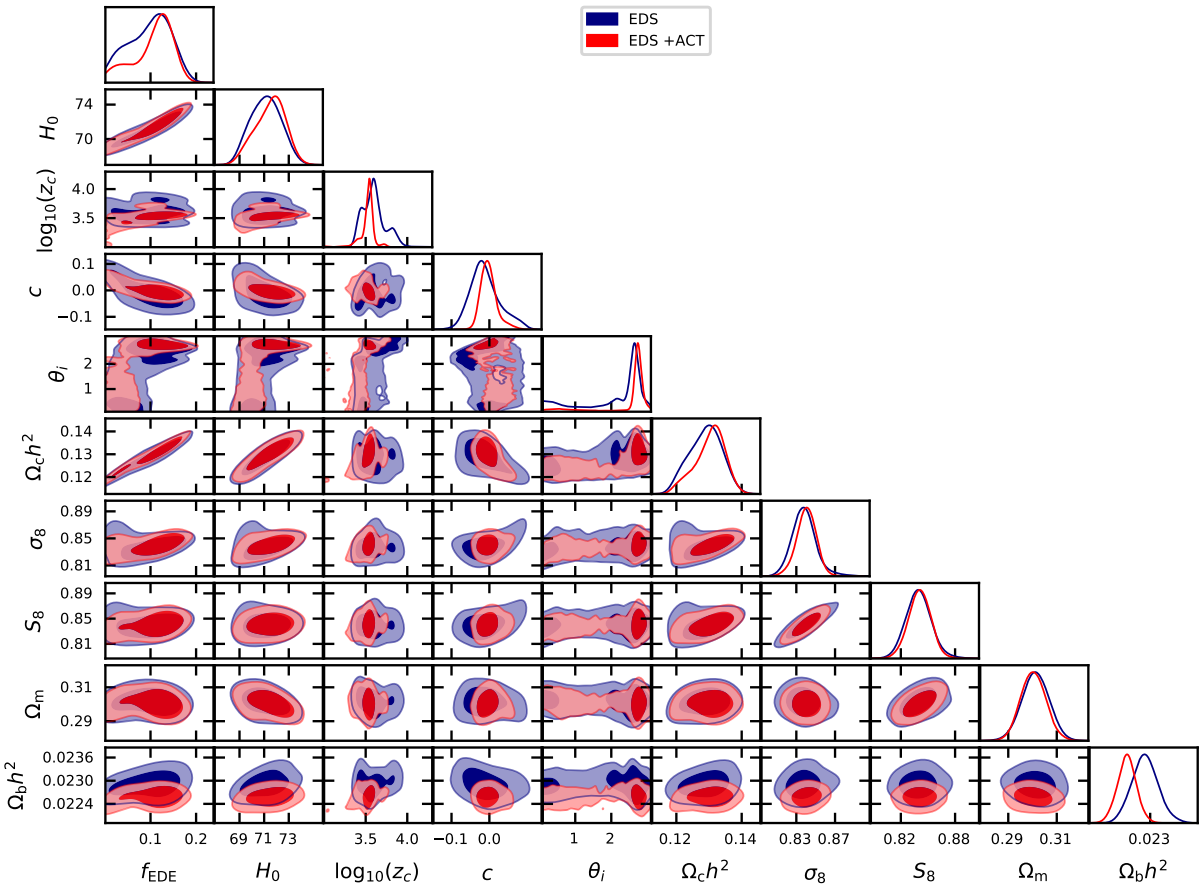

Figure A.3: Enlarged set of posterior distributions for the fit of the EDS to the baseline data set (Planck CMB, CMB lensing, BAO, SN, and SH0ES) with and without the addition of ACT data. Shaded grey and pink bands denote the SH0ES measurement and the DES-Y3 S_8 constraint, respectively.

APPENDIX B

PHENOMENOLOGY OF MODIFIED GRAVITY AT RECOMBINATION

B.1 Comoving Curvature Conservation

In order to take the initial comoving curvature perturbation $\mathcal{R}$ from inflation as initial conditions for the radiation dominated universe as usual, we need to show that it is conserved outside the horizon

$$\lim_{k/\mathcal{H}\to 0} \frac{\mathcal{R}'}{\mathcal{R}} = 0 \tag{B.1}$$

for any type of matter or modified gravity parameters μ and γ. In this Appendix we derive the conditions under which this is true.

Starting from the definition of the comoving curvature in terms of Newtonian gauge variables in a spatially flat universe

$$\mathcal{R} = -\Phi - \frac{\mathcal{H}}{k^2}\theta, \tag{B.2}$$

we use the modified gravity equations (5.7,5.8) to obtain

$$\mathcal{R} = \frac{4\pi G a^2 \mu}{k^2}\left[\gamma\Delta\rho + 3(\gamma-1)(\rho+P)\sigma\right] - \frac{\mathcal{H}}{k^2}\theta. \tag{B.3}$$

Taking the derivative of this equation and using the matter conservation equations (5.4), we

obtain

$$\mathcal{R}' = \mathcal{R}'_{\rm GR} + \frac{4\pi G a^2 \mu}{k^2 + 12\pi G a^2 \gamma\mu(\rho+P)} \times \left\{ C_1 \Delta\rho + C_2(\rho+p)\frac{\theta}{\mathcal{H}} + C_3(\rho+P)\sigma + C_4[(\rho+P)\sigma]' \right\} \tag{B.4}$$

where

$$\begin{aligned} C_1 &= 1 - \gamma + \gamma' + \gamma\frac{\mu'}{\mu}, \\ C_2 &= -\gamma - \frac{HH'}{4\pi G\mu(\rho+P)}, \\ C_3 &= 3(\gamma-1)\left(1+\frac{\mu'}{\mu}\right) + 3\gamma', \\ C_4 &= 3(\gamma-1), \end{aligned} \tag{B.5}$$

Under GR all of the C_i coefficients vanish leading to

$$\mathcal{R}'_{\rm GR} = -\frac{\delta P - (\mathcal{H}/k^2)P'\theta - (\rho+P)\sigma}{\rho+P}. \tag{B.6}$$

Note that the numerator of Eq. (B.6) is the total stress fluctuation in comoving gauge so that under GR, $\mathcal{R}$ is generally conserved if stress fluctuations are negligible, *i.e.* above the sound horizon.

Assuming $\mu, \gamma, \mu', \gamma' = \mathcal{O}(1)$ and the background only has small fluctuations from GR as well, the $C_i = \mathcal{O}(1)$ and the main difference in MG is that even without matter stress fluctuations the comoving curvature can evolve. However, the extra terms in $\mathcal{R}'/\mathcal{R}$ are still suppressed by $(k/\mathcal{H})^2$ above the horizon as long as there are no strong cancellations in the contributions to $\mathcal{R}$. Note that even if the MG parameters evolve on a time scale much more rapid than the expansion time, they just act as a superluminal sound speed with $\mathcal{R}'/\mathcal{R}$

suppressed by $(c_{\rm eff}k/\mathcal{H})^2$ with $c^2_{\rm eff} = \mathcal{O}(\mu'/\mu, \gamma'/\gamma)$. As $k/\mathcal{H} \to 0$, even these cases conserve comoving curvature. This generalizes the proof in Ref. [161] for arbitrary forms of matter and makes explicit the connection with the horizon scale.

B.2 Boltzmann Code

The calculations in this paper employ a modified version of the Einstein-Boltzmann solver CAMB. Unlike the treatment in the main text, CAMB uses synchronous gauge to represent perturbations. In this Appendix we detail our modifications to CAMB that mostly extend the MGCAMB implementation to early times and recombination.

B.2.1 Synchronous Gauge

The synchronous gauge of the cold dark matter, in the notation of Ref. [196], has two spatial metric potentials, the curvature η and the perturbation the trace of the spatial metric h. These are related to the Newtonian potentials by the gauge transformation

$$\begin{aligned} \Psi &= \mathcal{H}(\alpha' + \alpha), \\ \Phi &= \eta - \mathcal{H}\alpha\,, \end{aligned} \tag{B.7}$$

where $\alpha = \mathcal{H}(h' + 6\eta')/2k^2$. Hence, the modified Einstein equations in synchronous gauge are

$$\alpha' + \alpha = -\frac{4\pi G a^2 \mu}{k^2 \mathcal{H}}[\Delta\rho + 3(\rho + P)\sigma], \tag{B.8}$$

$$\eta - \gamma\mathcal{H}\alpha' - (\gamma + 1)\mathcal{H}\alpha = \frac{12\pi G a^2 \mu}{k^2}(\rho + P)\sigma. \tag{B.9}$$

The combination of these two equations gives the first equation we use to modify CAMB

$$\mathcal{H}\alpha = \eta + \frac{4\pi G a^2 \mu}{k^2}[\gamma\Delta\rho + 3(\gamma-1)(\rho+P)\sigma], \tag{B.10}$$

to replace the Einstein equation for h'. Constructed out of matter density fluctuations in synchronous gauge $\Delta\rho = \delta\rho + 3\mathcal{H}(\rho+P)\theta/k^2$ and retains the same form as when constructed out of Newtonian gauge fluctuations while σ is gauge invariant. From this point forward in this Appendix, all matter perturbation variables are in synchronous gauge. The synchronous matter fluctuations obey the usual conservation laws

$$\begin{aligned} \delta\rho' + 3(\delta\rho + \delta P) &= -(\rho+P)\left(\frac{\theta}{\mathcal{H}} + \frac{h'}{2}\right), \\ [(\rho+P)\theta]' + 4(\rho+P)\theta &= \frac{k^2}{\mathcal{H}}\Big[\delta P - (\rho+P)\sigma\Big]. \end{aligned} \tag{B.11}$$

These equations also apply to individual matter species in the absence of interactions. We refer the reader to e.g. Ref. [196] for the equations for baryons and photons separately in presence of Thomson scattering. Note that the joint photon-baryon system obeys Eq. (B.11) which is all we require below.

For the second equation, CAMB uses the time-space Einstein equation. Its modification can be derived from the derivative of Eq. (B.10) using Eq. (B.8,B.11)

$$\begin{aligned} \eta' \;=\; & \frac{4\pi G a^2 \mu}{k^2 + 12\pi G a^2 \gamma\mu(\rho+P)} \\ & \times\Bigg\{\left(1 - 3\frac{a^2 H H'}{k^2}\right)\gamma(\rho+P)\frac{\theta}{\mathcal{H}} - C_1\Delta\rho \\ & -C_2(\rho+P)\frac{k^2}{\mathcal{H}}\alpha - C_3(\rho+P)\sigma \\ & -C_4[(\rho+P)\sigma]'\Bigg\}, \end{aligned} \tag{B.12}$$

where the C_i coefficients are defined in eq. (B.5). Notice that in GR only the θ source remains

and that this source converts Eq. (B.10) to a direct relation between h' and $\delta\rho$ removing the velocity dependence in $\Delta\rho$.

Eq. (B.12) corrects an error in [176]. The correction term is proportional to $(\gamma - 1)\sigma$, so it affects the results when both $\gamma \neq 1$ and σ is important. At the late times the anisotropic stress σ is very small, so the impact of this correction is limited. However, at the early times the anisotropic stress is non-negligible, this correction has considerable influence. We also generalize the result for time-varying equations of state which is necessary for the treatment of massive neutrinos.

We also find some bugs in the publicly available Feb 2016 version of MGCAMB code. The bugs will affect the massive neutrino effects and the calculation of the derivatives of anisotropic stresses. Care should be used when employing MGCAMB in regimes where massive neutrinos or anisotropic stresses become important. These bugs are in the process of being fixed in the public version of the MGCAMB code [197]. On the other hand, in the regime where MGCAMB was mostly employed in literature, for modifications of gravity at late times, we find that such bugs have close to no effect on cosmological results.

B.2.2 Initial Conditions

Here we derive the initial conditions for cosmological perturbations in synchronous gauge when the perturbations in each k-mode are well outside the horizon. In this section we assume that μ and γ are constant near the initial conditions. We also assume that the background expansion is radiation dominated with an unmodified Friedmann equation.

Since CAMB solves equations in conformal time τ in this section we switch from $\log a$ to τ as the time variable. Under the background assumption, the relationship between the two at the initial epoch is

$$\tau = \frac{2}{\omega}\left(\sqrt{1 + \frac{\Omega_m}{\Omega_r}a} - 1\right), \tag{B.13}$$

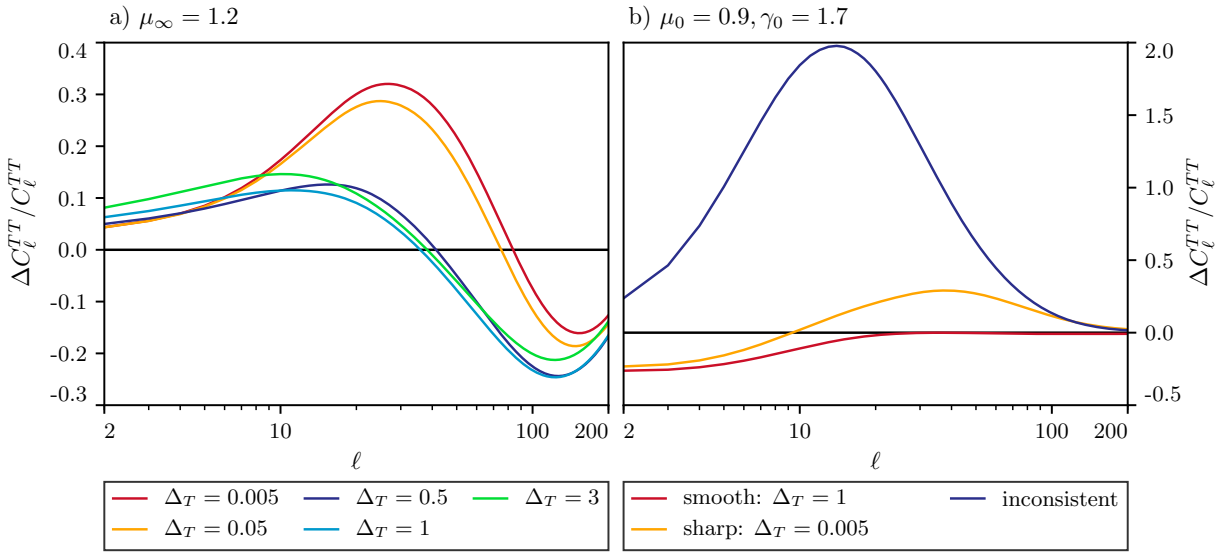

Figure B.1: The comparison of the unlensed large scale CMB temperature spectrum in several MG example models with different transition widths relative to the GR spectrum. Left: early time MG example models ($\mu_\infty = 1.2$). Right: late time MG example models along the degeneracy direction ($\mu_0 = 0.9$, $\gamma_0 = 1.7$). Here we also show the erroneously large effect predicted from the inconsistent implementation of an instantaneous transition employed in MGCAMB.

where

$$\omega \equiv \frac{H_0 \Omega_m}{\sqrt{\Omega_r}} \tag{B.14}$$

with $\rho_b + \rho_c = \Omega_m \rho_{\rm crit}/a^3$ as the sum of the baryon and cold dark matter densities and $\rho_\gamma + \rho_\nu = \Omega_r \rho_{\rm crit}/a^4$ in units of the present critical density $\rho_{\rm crit} = 3H_0^2/8\pi G$. Note that ω scales τ to its value around matter radiation equality so that both $k\tau \ll 1$ and $\omega\tau \ll 1$ at the initial conditions.

Using Eq. (B.11) individually for the separately conserved photon-baryon, neutrino, and cold dark matter fluids as well as the unmodified neutrino Boltzmann equation for its anisotropic stress

$$\dot{\sigma_\nu} = \frac{4}{15}\theta_\nu + \frac{2}{15}\dot{h} + \frac{4}{5}\dot{\eta}. \tag{B.15}$$

and the modified Einstein equations, we can now solve for the initial conditions in a series

expansion in $k\tau$ and $\omega\tau$. In general we keep the terms that are sufficient to determine the next to leading order correction in η and $\dot{h}$ following the CAMB conventions. Because $\dot{h}$ is derived from the modified equation (B.10) which involves θ we need to keep an extra $\omega\tau$ order in its initial condition relative to the GR result.

For adiabatic initial conditions

$$\delta_\gamma = \delta_\nu = \frac{4}{3}\delta_c = \frac{4}{3}\delta_b, \tag{B.16}$$

we obtain

$$\begin{aligned}
\frac{\eta}{\mathcal{R}} &= -1 + \frac{15 - 10\mu + 4\mu R_\nu}{12\mu(10\gamma + 5 + 4\mu R_\nu)}(k\tau)^2 + A_1(\omega k^2\tau^3), \\
\frac{\delta_\gamma}{\mathcal{R}} &= \frac{15 + 4\mu R_\nu}{3\mu(10\gamma + 5 + 4\mu R_\nu)}(k\tau)^2 + A_2(\omega k^2\tau^3), \\
\frac{\theta_\gamma}{\mathcal{R}} &= \frac{15 + 4\mu R_\nu}{36\mu(10\gamma + 5 + 4\mu R_\nu)}(k^4\tau^3) + A_3(\omega k^4\tau^4), \\
\frac{\theta_\nu}{\mathcal{R}} &= \frac{15 + 4(2 + R_\nu)\mu}{36\mu(10\gamma + 5 + 4\mu R_\nu)}(k^4\tau^3) + A_4(\omega k^4\tau^4), \\
\frac{\sigma_\nu}{\mathcal{R}} &= -\frac{2}{3(10\gamma + 5 + 4\mu R_\nu)}(k\tau)^2 + A_5(\omega k^2\tau^3)
\end{aligned} \tag{B.17}$$

with

$$\begin{aligned}
A_1 &= \frac{1}{4}A_2 + \frac{5}{4}A_5, \\
A_2 &= -\frac{30(\gamma + 1) + 4(13\gamma - 7)\mu R_\nu + \frac{32}{15}(\mu R_\nu)^2}{\mu(45\gamma + 15 + 8\mu R_\nu)(10\gamma + 5 + 4\mu R_\nu)}, \\
A_3 &= \frac{1}{16}A_2 - \frac{R_b(15 + 4\mu R_\nu)}{48\mu(1 - R_\nu)(10\gamma + 5 + 4\mu R_\nu)}, \\
A_4 &= \frac{1}{16}A_2 - \frac{1}{4}A_5, \\
A_5 &= \frac{5(\gamma + 1) - 8\mu R_\nu}{3(45\gamma + 15 + 8\mu R_\nu)(10\gamma + 5 + 4\mu R_\nu)},
\end{aligned} \tag{B.18}$$

where $R_b = \rho_b/\rho_m$ and $R_\nu = \rho_\nu/\rho_r$ given our assumption of an unmodified expansion

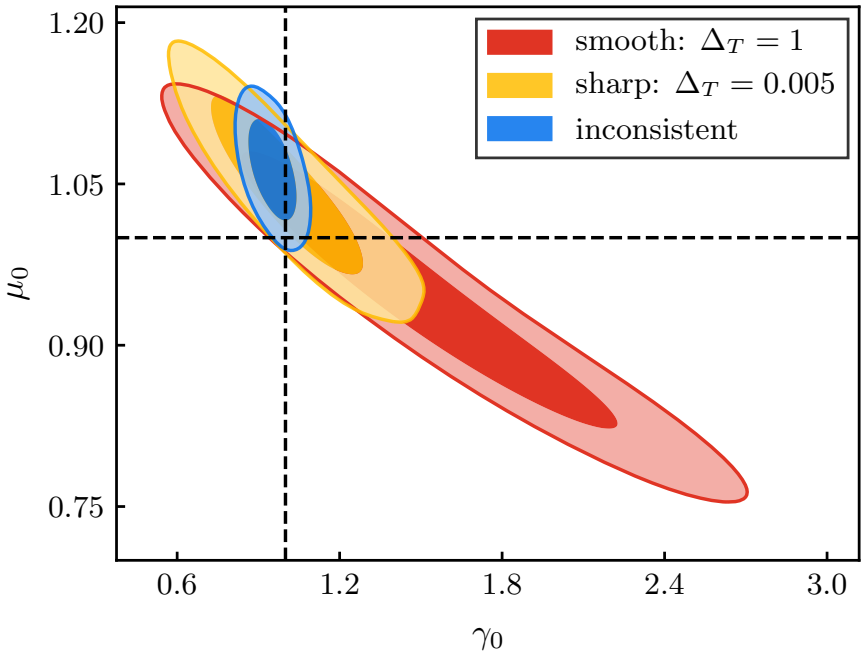

Figure B.2: The CMBTT constraints on late time MG parameters with different transition treatments from GR to MG. The darker and lighter shades correspond respectively to the 68% C.L. and the 95% C.L. The dashed lines indicate the values of MG parameters in GR limit. With a sharp transition the ISW effect shown in Fig. B.1 breaks the degeneracy between parameters leading to unrealistically strong constraints. The inconsistent instantaneous transition gives even stronger, but incorrect, constraints.

history. Together with $\dot{h} = -2\dot{\delta}_c$, these also define the initial conditions for α. Note that by definition $\theta_c = 0$ and by virtue of the tight coupling between photons and baryons, $\theta_b = \theta_\gamma$ and $\sigma_\gamma = 0$.

The initial comoving curvature $\mathcal{R}$ from inflation coincides with η since synchronous gauge and comoving gauge approximately coincide outside the horizon where the density perturbations are negligible. Note that we have kept an $\omega k^2 \tau^3$ correction to η for clarity and completeness even though this correction does not contribute dynamically at the desired order in either metric fluctuation and may be omitted from the code.

B.3 Impact of The Transition Width

In this appendix we comment on the impact of the transition width on the CMB temperature spectrum and hence all results involving the CMBTT dataset. For the analysis in the main text we use $\Delta_T = 1$ which we will now show leads to robust results.

In Fig. B.1, we show the result of varying this width. Around $\Delta_T = 1$, there is little impact from varying it by factors of a few up or down. When the transition width is much larger, $\Delta_T > 3$, the transition will start affecting the physics of recombination and the results become highly dependent on this parameter. When the width is very small the results are stable, but a sharp transition will introduce a relatively large effect on the CMB power spectrum through the ISW effect, see for example the lines with $\Delta_T = 0.05,\ 0.005$ in Fig. B.1. Since a transition that is much sharper than an efold would not be expected in a model where modifications evolve on the Hubble time, this effect would cause the CMBTT dataset to be unrealistically sensitive to the MG parameters.

Furthermore results in the literature often use MGCAMB which implements an instantaneous transition at the start of the MG epoch. If a MG parametrization is built to have deviations from GR right after the transition time, MGCAMB will return inconsistent and possibly incorrect results. The ISW effect depends on the time derivative of the Weyl potential and simply joining the GR and MG equations of motion at the transition neglects the part of its source which is the derivative of a step, *i.e.* a delta function source. In Fig. B.1b, we show the impact of this inconsistency on the CMB temperature power spectrum. Note that unlike in Fig. B.1a, the inconsistent instantaneous solution is not the limiting case of $\Delta_T \to 0$ but rather has a spuriously large ISW effect. To use MGCAMB consistently, one must ensure that the MG functions would go back to their GR value smoothly before the transition.

For example, in [23], the authors used MGCAMB to implement MG without demanding that the MG parameters smoothly relax to the GR values. This leads to overly tight con-

straints on the MG parameters. On the other hand, the parametrization used in [8] smoothly approaches the GR limit and by the time of the transition and leads to negligible deviations from GR so that the MGCAMB switching strategy produces consistent results.

In Fig. B.2, we show the impact on a μ_0-γ_0 MG model. Note that the inconsistent treatment provides much tighter constraints, especially on γ_0, than the limit of a sharp transition. Furthermore a consistently implemented sharp transition also provides tighter constraints than a smooth transition. For these reasons, we implement the smooth $\Delta_T = 1$ transition for the analysis in the main text.

REFERENCES

[1] Vivian Poulin, Tristan L. Smith, Daniel Grin, Tanvi Karwal, and Marc Kamionkowski. Cosmological implications of ultralight axionlike fields. *Phys. Rev.*, D98(8):083525, 2018.

[2] J. Colin Hill, Evan McDonough, Michael W. Toomey, and Stephon Alexander. Early dark energy does not restore cosmological concordance. *Phys. Rev. D*, 102(4):043507, 2020.

[3] Meng-Xiang Lin, Giampaolo Benevento, Wayne Hu, and Marco Raveri. Acoustic Dark Energy: Potential Conversion of the Hubble Tension. *Phys. Rev. D*, 100(6):063542, 2019.

[4] Meng-Xiang Lin, Wayne Hu, and Marco Raveri. Testing H_0 in Acoustic Dark Energy with Planck and ACT Polarization. *Phys. Rev. D*, 102:123523, 2020.

[5] Evan McDonough, Meng-Xiang Lin, J. Colin Hill, Wayne Hu, and Shengjia Zhou. The Early Dark Sector, the Hubble Tension, and the Swampland. 12 2021.

[6] Meng-Xiang Lin, Marco Raveri, and Wayne Hu. Phenomenology of Modified Gravity at Recombination. *Phys. Rev. D*, 99(4):043514, 2019.

[7] Adam G. Riess et al. A Comprehensive Measurement of the Local Value of the Hubble Constant with 1 km/s/Mpc Uncertainty from the Hubble Space Telescope and the SH0ES Team. 12 2021.

[8] N. Aghanim et al. Planck 2018 results. VI. Cosmological parameters. 2018.

[9] Marco Raveri. Reconstructing Gravity on Cosmological Scales. 2019.

[10] Giampaolo Benevento, Wayne Hu, and Marco Raveri. Can Late Dark Energy Transitions Raise the Hubble constant? *Phys. Rev. D*, 101(10):103517, 2020.

[11] Lloyd Knox and Marius Millea. Hubble constant hunterguide. *Phys. Rev. D*, 101(4):043533, 2020.

[12] Eleonora Di Valentino, Olga Mena, Supriya Pan, Luca Visinelli, Weiqiang Yang, Alessandro Melchiorri, David F. Mota, Adam G. Riess, and Joseph Silk. In the realm of the Hubble tension—a review of solutions. *Class. Quant. Grav.*, 38(15):153001, 2021.

[13] Vivian Poulin, Tristan L. Smith, Tanvi Karwal, and Marc Kamionkowski. Early Dark Energy Can Resolve The Hubble Tension. 2018.

[14] T. M. C. Abbott et al. Dark Energy Survey Year 3 Results: Cosmological Constraints from Galaxy Clustering and Weak Lensing. 5 2021.

[15] Adam G. Riess, Stefano Casertano, Wenlong Yuan, Lucas M. Macri, and Dan Scolnic. Large Magellanic Cloud Cepheid Standards Provide a 1% Foundation for the Determination of the Hubble Constant and Stronger Evidence for Physics Beyond LambdaCDM. 2019.

[16] Jose Luis Bernal, Licia Verde, and Adam G. Riess. The trouble with H_0. *JCAP*, 1610(10):019, 2016.

[17] Kevin Aylor, MacKenzie Joy, Lloyd Knox, Marius Millea, Srinivasan Raghunathan, and W. L. Kimmy Wu. Sounds Discordant: Classical Distance Ladder & ΛCDM - based Determinations of the Cosmological Sound Horizon. *Astrophys. J.*, 874(1):4, 2019.

[18] Gong-Bo Zhao et al. Dynamical dark energy in light of the latest observations. *Nat. Astron.*, 1(9):627–632, 2017.

[19] Giampaolo Benevento, Marco Raveri, Andrei Lazanu, Nicola Bartolo, Michele Liguori, Philippe Brax, and Patrick Valageas. K-mouflage imprints on cosmological observables and data constraints. *Journal of Cosmology and Astro-Particle Physics*, 2019(5):027, May 2019.

[20] Mark Wyman, Douglas H. Rudd, R. Ali Vanderveld, and Wayne Hu. Neutrinos Help Reconcile Planck Measurements with the Local Universe. *Phys. Rev. Lett.*, 112(5):051302, 2014.

[21] Cora Dvorkin, Mark Wyman, Douglas H. Rudd, and Wayne Hu. Neutrinos help reconcile Planck measurements with both the early and local Universe. *Phys. Rev.*, D90(8):083503, 2014.

[22] Boris Leistedt, Hiranya V. Peiris, and Licia Verde. No new cosmological concordance with massive sterile neutrinos. *Phys. Rev. Lett.*, 113:041301, 2014.

[23] P. A. R. Ade et al. Planck 2015 results. XIV. Dark energy and modified gravity. *Astron. Astrophys.*, 594:A14, 2016.

[24] Julien Lesgourgues, Gustavo Marques-Tavares, and Martin Schmaltz. Evidence for dark matter interactions in cosmological precision data? *JCAP*, 1602(02):037, 2016.

[25] M. Drewes et al. A White Paper on keV Sterile Neutrino Dark Matter. *JCAP*, 1701(01):025, 2017.

[26] Eleonora Di Valentino, Alessandro Melchiorri, and Joseph Silk. Reconciling Planck with the local value of H_0 in extended parameter space. *Phys. Lett.*, B761:242–246, 2016.

[27] Nicolas Canac, Grigor Aslanyan, Kevork N. Abazajian, Richard Easther, and Layne C. Price. Testing for New Physics: Neutrinos and the Primordial Power Spectrum. *JCAP*, 1609(09):022, 2016.

[28] Lu Feng, Jing-Fei Zhang, and Xin Zhang. A search for sterile neutrinos with the latest cosmological observations. *Eur. Phys. J.*, C77(6):418, 2017.

[29] Isabel M. Oldengott, Thomas Tram, Cornelius Rampf, and Yvonne Y. Y. Wong. Interacting neutrinos in cosmology: exact description and constraints. *JCAP*, 1711(11):027, 2017.

[30] Lachlan Lancaster, Francis-Yan Cyr-Racine, Lloyd Knox, and Zhen Pan. A tale of two modes: Neutrino free-streaming in the early universe. *JCAP*, 1707(07):033, 2017.

[31] Christina D. Kreisch, Francis-Yan Cyr-Racine, and Olivier Doré. The Neutrino Puzzle: Anomalies, Interactions, and Cosmological Tensions. 2019.

[32] Wayne Hu and Martin J. White. Acoustic signatures in the cosmic microwave background. *Astrophys. J.*, 471:30–51, 1996.

[33] Marco Raveri, Wayne Hu, Timothy Hoffman, and Lian-Tao Wang. Partially Acoustic Dark Matter Cosmology and Cosmological Constraints. *Phys. Rev.*, D96(10):103501, 2017.

[34] Prateek Agrawal, Francis-Yan Cyr-Racine, David Pinner, and Lisa Randall. Rock 'n' Roll Solutions to the Hubble Tension. 2019.

[35] C. Armendariz-Picon, Viatcheslav F. Mukhanov, and Paul J. Steinhardt. Essentials of k essence. *Phys. Rev.*, D63:103510, 2001.

[36] Wayne Hu. Structure formation with generalized dark matter. *Astrophys. J.*, 506:485–494, 1998.

[37] Andrew J. Long, Marco Raveri, Wayne Hu, and Scott Dodelson. Neutrino Mass Priors for Cosmology from Random Matrices. *Phys. Rev.*, D97(4):043510, 2018.

[38] Antony Lewis, Anthony Challinor, and Anthony Lasenby. Efficient computation of CMB anisotropies in closed FRW models. *Astrophys. J.*, 538:473–476, 2000.

[39] Antony Lewis and Sarah Bridle. Cosmological parameters from CMB and other data: A Monte Carlo approach. *Phys. Rev.*, D66:103511, 2002.

[40] Andrew Gelman and Donald B. Rubin. Inference from iterative simulation using multiple sequences. *Statist. Sci.*, 7(4):457–472, 11 1992.

[41] P. A. R. Ade et al. Planck 2015 results. XIII. Cosmological parameters. *Astron. Astrophys.*, 594:A13, 2016.

[42] N. Aghanim et al. Planck 2015 results. XI. CMB power spectra, likelihoods, and robustness of parameters. *Astron. Astrophys.*, 594:A11, 2016.

[43] P. A. R. Ade et al. Planck 2015 results. XV. Gravitational lensing. *Astron. Astrophys.*, 594:A15, 2016.

[44] D. M. Scolnic et al. The Complete Light-curve Sample of Spectroscopically Confirmed SNe Ia from Pan-STARRS1 and Cosmological Constraints from the Combined Pantheon Sample. *Astrophys. J.*, 859(2):101, 2018.

[45] Shadab Alam et al. The clustering of galaxies in the completed SDSS-III Baryon Oscillation Spectroscopic Survey: cosmological analysis of the DR12 galaxy sample. *Mon. Not. Roy. Astron. Soc.*, 470(3):2617–2652, 2017.

[46] Ashley J. Ross, Lado Samushia, Cullan Howlett, Will J. Percival, Angela Burden, and Marc Manera. The clustering of the SDSS DR7 main Galaxy sample – I. A 4 per cent distance measure at $z = 0.15$. *Mon. Not. Roy. Astron. Soc.*, 449(1):835–847, 2015.

[47] Florian Beutler, Chris Blake, Matthew Colless, D. Heath Jones, Lister Staveley-Smith, Lachlan Campbell, Quentin Parker, Will Saunders, and Fred Watson. The 6dF Galaxy Survey: Baryon Acoustic Oscillations and the Local Hubble Constant. *Mon. Not. Roy. Astron. Soc.*, 416:3017–3032, 2011.

[48] Georges Obied, Cora Dvorkin, Chen Heinrich, Wayne Hu, and Vinicius Miranda. Inflationary Features and Shifts in Cosmological Parameters from Planck 2015 Data. *Phys. Rev.*, D96(8):083526, 2017.

[49] Christopher Gordon and Wayne Hu. A Low CMB quadrupole from dark energy isocurvature perturbations. *Phys. Rev.*, D70:083003, 2004.

[50] Paul J. Steinhardt, Li-Min Wang, and Ivaylo Zlatev. Cosmological tracking solutions. *Phys. Rev.*, D59:123504, 1999.

[51] N. Aghanim et al. Planck intermediate results. LI. Features in the cosmic microwave background temperature power spectrum and shifts in cosmological parameters. *Astron. Astrophys.*, 607:A95, 2017.

[52] Stephon Alexander and Evan McDonough. Axion-Dilaton Destabilization and the Hubble Tension. 2019.

[53] Wendy L. Freedman et al. The Carnegie-Chicago Hubble Program. VIII. An Independent Determination of the Hubble Constant Based on the Tip of the Red Giant Branch. 2019.

[54] Wendy L. Freedman, Barry F. Madore, Taylor Hoyt, In Sung Jang, Rachael Beaton, Myung Gyoon Lee, Andrew Monson, Jill Neeley, and Jeffrey Rich. Calibration of the Tip of the Red Giant Branch (TRGB). 2020.

[55] Caroline D. Huang, Adam G. Riess, Wenlong Yuan, Lucas M. Macri, Nadia L. Zakamska, Stefano Casertano, Patricia A. Whitelock, Samantha L. Hoffmann, Alexei V. Filippenko, and Daniel Scolnic. Hubble Space Telescope Observations of Mira Variables in the Type Ia Supernova Host NGC 1559: An Alternative Candle to Measure the Hubble Constant. 8 2019.

[56] D. W. Pesce et al. The Megamaser Cosmology Project. XIII. Combined Hubble constant constraints. 2020.

[57] Kenneth C. Wong et al. H0LiCOW XIII. A 2.45.3σ tension between early and late-Universe probes. 7 2019.

[58] S. Birrer et al. TDCOSMO IV: Hierarchical time-delay cosmography – joint inference of the Hubble constant and galaxy density profiles. 7 2020.

[59] K. Aylor et al. A Comparison of Cosmological Parameters Determined from CMB Temperature Power Spectra from the South Pole Telescope and the Planck Satellite. *Astrophys. J.*, 850(1):101, 2017.

[60] Simone Aiola et al. The Atacama Cosmology Telescope: DR4 Maps and Cosmological Parameters. 7 2020.

[61] Steve K. Choi et al. The Atacama Cosmology Telescope: A Measurement of the Cosmic Microwave Background Power Spectra at 98 and 150 GHz. 7 2020.

[62] Minsu Park, Christina D. Kreisch, Jo Dunkley, Boryana Hadzhiyska, and Francis-Yan Cyr-Racine. ΛCDM or self-interacting neutrinos: How CMB data can tell the two models apart. *Phys. Rev. D*, 100(6):063524, 2019.

[63] Ryan E. Keeley, Shahab Joudaki, Manoj Kaplinghat, and David Kirkby. Implications of a transition in the dark energy equation of state for the H_0 and σ_8 tensions. *JCAP*, 12:035, 2019.

[64] Xiaolei Li and Arman Shafieloo. A Simple Phenomenological Emergent Dark Energy Model can Resolve the Hubble Tension. *Astrophys. J. Lett.*, 883(1):L3, 2019.

[65] Subhajit Ghosh, Rishi Khatri, and Tuhin S. Roy. Dark Neutrino interactions phase out the Hubble tension. 8 2019.

[66] Miaoxin Liu, Zhiqi Huang, Xiaolin Luo, Haitao Miao, Naveen K. Singh, and Lu Huang. Can Non-standard Recombination Resolve the Hubble Tension? *Sci. China Phys. Mech. Astron.*, 63(9):290405, 2020.

[67] Xiaolei Li and Arman Shafieloo. Evidence for Emergent Dark Energy. 1 2020.

[68] Wei-Ming Dai, Yin-Zhe Ma, and Hong-Jian He. Reconciling Hubble Constant Discrepancy from Holographic Dark Energy. 3 2020.

[69] Miguel Zumalacarregui. Gravity in the Era of Equality: Towards solutions to the Hubble problem without fine-tuned initial conditions. *Phys. Rev. D*, 102(2):023523, 2020.

[70] Guillermo Ballesteros, Alessio Notari, and Fabrizio Rompineve. The H_0 tension: ΔG_N vs. $\Delta N_{\rm eff}$. 4 2020.

[71] G. Alestas, L. Kazantzidis, and L. Perivolaropoulos. H_0 tension, phantom dark energy, and cosmological parameter degeneracies. *Phys. Rev. D*, 101(12):123516, 2020.

[72] Karsten Jedamzik and Levon Pogosian. Relieving the Hubble tension with primordial magnetic fields. 4 2020.

[73] Matteo Braglia, Mario Ballardini, William T. Emond, Fabio Finelli, A. Emir Gumrukcuoglu, Kazuya Koyama, and Daniela Paoletti. Larger value for H_0 by an evolving gravitational constant. *Phys. Rev. D*, 102(2):023529, 2020.

[74] Mark Gonzalez, Mark P. Hertzberg, and Fabrizio Rompineve. Ultralight Scalar Decay and the Hubble Tension. 6 2020.

[75] Eleonora Di Valentino, Eric V. Linder, and Alessandro Melchiorri. H_0 Ex Machina: Vacuum Metamorphosis and Beyond H_0. 6 2020.

[76] Tristan L. Smith, Vivian Poulin, and Mustafa A. Amin. Oscillating scalar fields and the Hubble tension: a resolution with novel signatures. *Phys. Rev. D*, 101(6):063523, 2020.

[77] Kim V. Berghaus and Tanvi Karwal. Thermal Friction as a Solution to the Hubble Tension. *Phys. Rev. D*, 101(8):083537, 2020.

[78] Florian Niedermann and Martin S. Sloth. New Early Dark Energy. 10 2019.

[79] Jeremy Sakstein and Mark Trodden. Early Dark Energy from Massive Neutrinos as a Natural Resolution of the Hubble Tension. *Phys. Rev. Lett.*, 124(16):161301, 2020.

[80] Gen Ye and Yun-Song Piao. Is the Hubble tension a hint of AdS phase around recombination? *Phys. Rev. D*, 101(8):083507, 2020.

[81] Matteo Braglia, William T. Emond, Fabio Finelli, A. Emir Gumrukcuoglu, and Kazuya Koyama. Unified framework for Early Dark Energy from α-attractors. 5 2020.

[82] Florian Niedermann and Martin S. Sloth. Resolving the Hubble Tension with New Early Dark Energy. 6 2020.

[83] Gen Ye and Yun-Song Piao. T_0 censorship of early dark energy and AdS. 8 2020.

[84] Mikhail M. Ivanov, Evan McDonough, J. Colin Hill, Marko Simonović, Michael W. Toomey, Stephon Alexander, and Matias Zaldarriaga. Constraining Early Dark Energy with Large-Scale Structure. 6 2020.

[85] Guido D'Amico, Leonardo Senatore, Pierre Zhang, and Henry Zheng. The Hubble Tension in Light of the Full-Shape Analysis of Large-Scale Structure Data. 6 2020.

[86] Florian Niedermann and Martin S. Sloth. New Early Dark Energy is compatible with current LSS data. 8 2020.

[87] N. Aghanim et al. Planck 2018 results. V. CMB power spectra and likelihoods. 7 2019.

[88] N. Aghanim et al. Planck 2018 results. VIII. Gravitational lensing. 7 2018.

[89] L. Verde, T. Treu, and A. G. Riess. Tensions between the Early and the Late Universe. In *Nature Astronomy 2019*, 2019.

[90] Hirosi Ooguri and Cumrun Vafa. On the Geometry of the String Landscape and the Swampland. *Nucl. Phys. B*, 766:21–33, 2007.

[91] Florent Baume and Eran Palti. Backreacted Axion Field Ranges in String Theory. *JHEP*, 08:043, 2016.

[92] Daniel Klaewer and Eran Palti. Super-Planckian Spatial Field Variations and Quantum Gravity. *JHEP*, 01:088, 2017.

[93] Ralph Blumenhagen, Irene Valenzuela, and Florian Wolf. The Swampland Conjecture and F-term Axion Monodromy Inflation. *JHEP*, 07:145, 2017.

[94] Marco Scalisi and Irene Valenzuela. Swampland distance conjecture, inflation and α-attractors. *JHEP*, 08:160, 2019.

[95] Adam G. Riess, Stefano Casertano, Wenlong Yuan, J. Bradley Bowers, Lucas Macri, Joel C. Zinn, and Dan Scolnic. Cosmic Distances Calibrated to 1% Precision with Gaia EDR3 Parallaxes and Hubble Space Telescope Photometry of 75 Milky Way Cepheids Confirm Tension with ΛCDM. *Astrophys. J. Lett.*, 908(1):L6, 2021.

[96] Ryan J. Cooke, Max Pettini, Kenneth M. Nollett, and Regina Jorgenson. The Primordial Deuterium Abundance of the Most Metal-poor Damped Lyman-α System. , 830(2):148, Oct 2016.

[97] Éric Aubourg et al. Cosmological implications of baryon acoustic oscillation measurements. *Phys. Rev. D*, 92(12):123516, 2015.

[98] Andrei Cuceu, James Farr, Pablo Lemos, and Andreu Font-Ribera. Baryon Acoustic Oscillations and the Hubble Constant: Past, Present and Future. *JCAP*, 10:044, 2019.

[99] Nils Schöneberg, Julien Lesgourgues, and Deanna C. Hooper. The BAO+BBN take on the Hubble tension. *JCAP*, 10:029, 2019.

[100] T. M. C. Abbott et al. Dark Energy Survey Year 1 Results: A Precise H0 Estimate from DES Y1, BAO, and D/H Data. *Mon. Not. Roy. Astron. Soc.*, 480(3):3879–3888, 2018.

[101] Oliver H. E. Philcox, Mikhail M. Ivanov, Marko Simonovic, and Matias Zaldarriaga. Combining Full-Shape and BAO Analyses of Galaxy Power Spectra: A 1.6% CMB-independent constraint on H0. 2020.

[102] Paul Shah, Pablo Lemos, and Ofer Lahav. A buyer's guide to the Hubble Constant. 9 2021.

[103] George Efstathiou. To H0 or not to H0? 3 2021.

[104] Karsten Jedamzik, Levon Pogosian, and Gong-Bo Zhao. Why reducing the cosmic sound horizon can not fully resolve the Hubble tension. 10 2020.

[105] Weikang Lin, Xingang Chen, and Katherine J. Mack. Early Universe Physics Insensitive and Uncalibrated Cosmic Standards: Constraints on Ωm and Implications for the Hubble Tension. *Astrophys. J.*, 920(2):159, 2021.

[106] Steven J. Clark, Kyriakos Vattis, JiJi Fan, and Savvas M. Koushiappas. The H_0 and S_8 tensions necessitate early and late time changes to ΛCDM. 10 2021.

[107] Itamar J. Allali, Mark P. Hertzberg, and Fabrizio Rompineve. Dark sector to restore cosmological concordance. *Phys. Rev. D*, 104(8):L081303, 2021.

[108] Tanvi Karwal, Marco Raveri, Bhuvnesh Jain, Justin Khoury, and Mark Trodden. Chameleon Early Dark Energy and the Hubble Tension. 6 2021.

[109] H. Hildebrandt et al. KiDS-450: Cosmological parameter constraints from tomographic weak gravitational lensing. *Mon. Not. Roy. Astron. Soc.*, 465:1454, 2017.

[110] H. Hildebrandt et al. KiDS+VIKING-450: Cosmic shear tomography with optical and infrared data. , 633:A69, January 2020.

[111] Chiaki Hikage et al. Cosmology from cosmic shear power spectra with Subaru Hyper Suprime-Cam first-year data. *Publ. Astron. Soc. Jap.*, 71(2):Publications of the Astronomical Society of Japan, Volume 71, Issue 2, April 2019, 43, https://doi.org/10.1093/pasj/psz010, 2019.

[112] Tristan L. Smith, Vivian Poulin, José Luis Bernal, Kimberly K. Boddy, Marc Kamionkowski, and Riccardo Murgia. Early dark energy is not excluded by current large-scale structure data. *Phys. Rev. D*, 103(12):123542, 2021.

[113] Marc Kamionkowski, Josef Pradler, and Devin G. E. Walker. Dark energy from the string axiverse. *Phys. Rev. Lett.*, 113(25):251302, 2014.

[114] David J. E. Marsh. Axion Cosmology. *Phys. Rept.*, 643:1–79, 2016.

[115] Tom Banks, Michael Dine, Patrick J. Fox, and Elie Gorbatov. On the possibility of large axion decay constants. *JCAP*, 0306:001, 2003.

[116] Tom Rudelius. On the Possibility of Large Axion Moduli Spaces. *JCAP*, 1504(04):049, 2015.

[117] John Stout. Instanton Expansions and Phase Transitions. 12 2020.

[118] Raphael Bousso and Joseph Polchinski. Quantization of four form fluxes and dynamical neutralization of the cosmological constant. *JHEP*, 06:006, 2000.

[119] Leonard Susskind. The Anthropic landscape of string theory. pages 247–266, 2 2003.

[120] Cumrun Vafa. The String landscape and the swampland. 9 2005.

[121] Eran Palti. The Swampland: Introduction and Review. *Fortsch. Phys.*, 67(6):1900037, 2019.

[122] T. Daniel Brennan, Federico Carta, and Cumrun Vafa. The String Landscape, the Swampland, and the Missing Corner. *PoS*, TASI2017:015, 2017.

[123] Marieke van Beest, José Calderón-Infante, Delaram Mirfendereski, and Irene Valenzuela. Lectures on the Swampland Program in String Compactifications. 2 2021.

[124] Prateek Agrawal, Georges Obied, and Cumrun Vafa. H_0 tension, swampland conjectures, and the epoch of fading dark matter. *Phys. Rev. D*, 103(4):043523, 2021.

[125] Luis A. Anchordoqui, Ignatios Antoniadis, Dieter Lüst, Jorge F. Soriano, and Tomasz R. Taylor. H_0 tension and the String Swampland. *Phys. Rev. D*, 101:083532, 2020.

[126] Dongok Kim, Younggeun Kim, Yannis K. Semertzidis, Yun Chang Shin, and Wen Yin. Cosmic axion force. *Phys. Rev. D*, 104(9):095010, 2021.

[127] Planck Collaboration. Planck 2018 results. V. CMB power spectra and likelihoods. *arXiv e-prints*, page arXiv:1907.12875, July 2019.

[128] Planck Collaboration. Planck 2018 results. VIII. Gravitational lensing. *arXiv e-prints*, page arXiv:1807.06210, July 2018.

[129] Florian Beutler, Chris Blake, Matthew Colless, D. Heath Jones, Lister Staveley-Smith, Lachlan Campbell, Quentin Parker, Will Saunders, and Fred Watson. The 6dF Galaxy Survey: baryon acoustic oscillations and the local Hubble constant. , 416(4):3017–3032, Oct 2011.

[130] Simone Aiola et al. The Atacama Cosmology Telescope: DR4 Maps and Cosmological Parameters. *JCAP*, 12:047, 2020.

[131] Steve K. Choi et al. The Atacama Cosmology Telescope: a measurement of the Cosmic Microwave Background power spectra at 98 and 150 GHz. *JCAP*, 12:045, 2020.

[132] J. Colin Hill et al. The Atacama Cosmology Telescope: Constraints on Pre-Recombination Early Dark Energy. 9 2021.

[133] Nemanja Kaloper. Dark Energy, H_0 and Weak Gravity Conjecture. *Int. J. Mod. Phys.*, D28(14):1944017, 2019.

[134] Shinji Tsujikawa. Quintessence: A Review. *Class. Quant. Grav.*, 30:214003, 2013.

[135] Vivian Poulin, Tristan L. Smith, and Alexa Bartlett. Dark Energy at early times and ACT: a larger Hubble constant without late-time priors. 9 2021.

[136] Fiona McCarthy, J. Colin Hill, and Mathew S. Madhavacheril. Baryonic feedback biases on fundamental physics from lensed CMB power spectra. 3 2021.

[137] Julien Lesgourgues. The Cosmic Linear Anisotropy Solving System (CLASS) I: Overview. *arXiv e-prints*, page arXiv:1104.2932, Apr 2011.

[138] Diego Blas, Julien Lesgourgues, and Thomas Tram. The Cosmic Linear Anisotropy Solving System (CLASS). Part II: Approximation schemes. , 2011(7):034, Jul 2011.

[139] Jesus Torrado and Anthony Lewis. Cobaya, Oct 2019.

[140] Antony Lewis. GetDist: a Python package for analysing Monte Carlo samples. *arXiv e-prints*, page arXiv:1910.13970, October 2019.

[141] Andrew Gelman and Donald B. Rubin. Inference from Iterative Simulation Using Multiple Sequences. *Statist. Sci.*, 7:457–472, 1992.

[142] M. Powell. The bobyqa algorithm for bound constrained optimization without derivatives. *Technical Report, Department of Applied Mathematics and Theoretical Physics*, 01 2009.

[143] Coralia Cartis, Jan Fiala, Benjamin Marteau, and Lindon Roberts. Improving the Flexibility and Robustness of Model-Based Derivative-Free Optimization Solvers. *arXiv e-prints*, page arXiv:1804.00154, March 2018.

[144] Coralia Cartis, Lindon Roberts, and Oliver Sheridan-Methven. Escaping local minima with derivative-free methods: a numerical investigation. *arXiv e-prints*, page arXiv:1812.11343, December 2018.

[145] Alessio Spurio Mancini, Davide Piras, Justin Alsing, Benjamin Joachimi, and Michael P. Hobson. *CosmoPower* : emulating cosmological power spectra for accelerated Bayesian inference from next-generation surveys. 6 2021.

[146] Adam Moss, Edmund Copeland, Steven Bamford, and Thomas Clarke. A model-independent reconstruction of dark energy to very high redshift. 9 2021.

[147] Georges Obied, Hirosi Ooguri, Lev Spodyneiko, and Cumrun Vafa. De Sitter Space and the Swampland. 6 2018.

[148] Marco Raveri, Wayne Hu, and Savdeep Sethi. Swampland Conjectures and Late-Time Cosmology. *Phys. Rev. D*, 99(8):083518, 2019.

[149] Lavinia Heisenberg, Matthias Bartelmann, Robert Brandenberger, and Alexandre Refregier. Dark Energy in the Swampland. *Phys. Rev. D*, 98(12):123502, 2018.

[150] Yashar Akrami, Renata Kallosh, Andrei Linde, and Valeri Vardanyan. The Landscape, the Swampland and the Era of Precision Cosmology. *Fortsch. Phys.*, 67(1-2):1800075, 2019.

[151] Hirotogu Akaike. *Information Theory and an Extension of the Maximum Likelihood Principle*, pages 199–213. Springer New York, New York, NY, 1973.

[152] Adam G. Riess et al. Observational evidence from supernovae for an accelerating universe and a cosmological constant. *Astron. J.*, 116:1009–1038, 1998.

[153] S. Perlmutter et al. Measurements of Omega and Lambda from 42 high redshift supernovae. *Astrophys. J.*, 517:565–586, 1999.

[154] Alessandra Silvestri and Mark Trodden. Approaches to Understanding Cosmic Acceleration. *Rept. Prog. Phys.*, 72:096901, 2009.

[155] Timothy Clifton, Pedro G. Ferreira, Antonio Padilla, and Constantinos Skordis. Modified Gravity and Cosmology. *Phys. Rept.*, 513:1–189, 2012.

[156] Austin Joyce, Bhuvnesh Jain, Justin Khoury, and Mark Trodden. Beyond the Cosmological Standard Model. *Phys. Rept.*, 568:1–98, 2015.

[157] Shahab Joudaki et al. KiDS-450: Testing extensions to the standard cosmological model. *Mon. Not. Roy. Astron. Soc.*, 471(2):1259–1279, 2017.

[158] Kevork N. Abazajian et al. CMB-S4 Science Book, First Edition. 2016.

[159] R. Laureijs et al. Euclid Definition Study Report. 2011.

[160] Paul A. Abell et al. LSST Science Book, Version 2.0. 2009.

[161] Gong-Bo Zhao, Levon Pogosian, Alessandra Silvestri, and Joel Zylberberg. Searching for modified growth patterns with tomographic surveys. *Phys. Rev.*, D79:083513, 2009.

[162] Gong-Bo Zhao, Levon Pogosian, Alessandra Silvestri, and Joel Zylberberg. Cosmological Tests of General Relativity with Future Tomographic Surveys. *Phys. Rev. Lett.*, 103:241301, 2009.

[163] Alireza Hojjati, Gong-Bo Zhao, Levon Pogosian, Alessandra Silvestri, Robert Crittenden, and Kazuya Koyama. Cosmological tests of General Relativity: a principal component analysis. *Phys. Rev.*, D85:043508, 2012.

[164] Shinsuke Asaba, Chiaki Hikage, Kazuya Koyama, Gong-Bo Zhao, Alireza Hojjati, and Levon Pogosian. Principal Component Analysis of Modified Gravity using Weak Lensing and Peculiar Velocity Measurements. *JCAP*, 1308:029, 2013.

[165] Robert Caldwell, Asantha Cooray, and Alessandro Melchiorri. Constraints on a New Post-General Relativity Cosmological Parameter. *Phys. Rev.*, D76:023507, 2007.

[166] Luca Amendola, Martin Kunz, and Domenico Sapone. Measuring the dark side (with weak lensing). *JCAP*, 0804:013, 2008.

[167] Wayne Hu and Ignacy Sawicki. A Parameterized Post-Friedmann Framework for Modified Gravity. *Phys. Rev.*, D76:104043, 2007.

[168] Edmund Bertschinger and Phillip Zukin. Distinguishing Modified Gravity from Dark Energy. *Phys. Rev.*, D78:024015, 2008.

[169] Levon Pogosian, Alessandra Silvestri, Kazuya Koyama, and Gong-Bo Zhao. How to optimally parametrize deviations from General Relativity in the evolution of cosmological perturbations? *Phys. Rev.*, D81:104023, 2010.

[170] Levon Pogosian and Alessandra Silvestri. What can cosmology tell us about gravity? Constraining Horndeski gravity with Σ and μ. *Phys. Rev.*, D94(10):104014, 2016.

[171] Alireza Hojjati, Aaron Plahn, Alex Zucca, Levon Pogosian, Philippe Brax, Anne-Christine Davis, and Gong-Bo Zhao. Searching for scalar gravitational interactions in current and future cosmological data. *Phys. Rev.*, D93(4):043531, 2016.

[172] Santiago Casas, Martin Kunz, Matteo Martinelli, and Valeria Pettorino. Linear and non-linear Modified Gravity forecasts with future surveys. *Phys. Dark Univ.*, 18:73–104, 2017.

[173] Simone Peirone, Kazuya Koyama, Levon Pogosian, Marco Raveri, and Alessandra Silvestri. Large-scale structure phenomenology of viable Horndeski theories. *Phys. Rev.*, D97(4):043519, 2018.

[174] Juan Espejo, Simone Peirone, Marco Raveri, Kazuya Koyama, Levon Pogosian, and Alessandra Silvestri. Phenomenology of Large Scale Structure in scalar-tensor theories: joint prior covariance of $w_{\rm DE}$, Σ and μ in Horndeski. 2018.

[175] A. Lewis, A. Challinor, and A. Lasenby. Efficient Computation of Cosmic Microwave Background Anisotropies in Closed Friedmann-Robertson-Walker Models. , 538:473–476, August 2000.

[176] Alireza Hojjati, Levon Pogosian, and Gong-Bo Zhao. Testing gravity with CAMB and CosmoMC. *JCAP*, 1108:005, 2011.

[177] Marco Raveri and Wayne Hu. Concordance and Discordance in Cosmology. 2018.

[178] Christiane S. Lorenz, Erminia Calabrese, and David Alonso. Distinguishing between Neutrinos and time-varying Dark Energy through Cosmic Time. *Phys. Rev.*, D96(4):043510, 2017.

[179] Mustapha Ishak. Testing General Relativity in Cosmology. 2018.

[180] Wayne Hu and Austin Joyce. Separate Universes beyond General Relativity. *Phys. Rev.*, D95(4):043529, 2017.

[181] W. Hu and N. Sugiyama. Anisotropies in the cosmic microwave background: an analytic approach. , 444:489–506, May 1995.

[182] Daniel Baumann, Daniel Green, Joel Meyers, and Benjamin Wallisch. Phases of New Physics in the CMB. *JCAP*, 1601:007, 2016.

[183] W. Hu and N. Sugiyama. Small-Scale Cosmological Perturbations: an Analytic Approach. , 471:542, November 1996.

[184] Wayne Hu and Daniel J. Eisenstein. Small scale perturbations in a general MDM cosmology. *Astrophys. J.*, 498:497, 1998.

[185] Lam Hui and Kyle P. Parfrey. The Evolution of Bias: Generalized. *Phys. Rev.*, D77:043527, 2008.

[186] Chi-Ting Chiang, Wayne Hu, Yin Li, and Marilena Loverde. Scale-dependent bias and bispectrum in neutrino separate universe simulations. *Phys. Rev.*, D97(12):123526, 2018.

[187] Adam G. Riess et al. A 2.4% Determination of the Local Value of the Hubble Constant. *Astrophys. J.*, 826(1):56, 2016.

[188] Catherine Heymans et al. CFHTLenS tomographic weak lensing cosmological parameter constraints: Mitigating the impact of intrinsic galaxy alignments. *Mon. Not. Roy. Astron. Soc.*, 432:2433, 2013.

[189] Shahab Joudaki et al. CFHTLenS revisited: assessing concordance with Planck including astrophysical systematics. *Mon. Not. Roy. Astron. Soc.*, 465(2):2033–2052, 2017.

[190] M. Betoule et al. Improved cosmological constraints from a joint analysis of the SDSS-II and SNLS supernova samples. *Astron. Astrophys.*, 568:A22, 2014.

[191] G. E. Addison, Y. Huang, D. J. Watts, C. L. Bennett, M. Halpern, G. Hinshaw, and J. L. Weiland. Quantifying Discordance in the 2015 Planck CMB Spectrum. , 818:132, February 2016.

[192] G. Obied, C. Dvorkin, C. Heinrich, W. Hu, and V. Miranda. Inflationary Features and Shifts in Cosmological Parameters from Planck 2015 Data. *ArXiv e-prints*, June 2017.

[193] Bin Hu and Marco Raveri. Can modified gravity models reconcile the tension between the CMB anisotropy and lensing maps in Planck-like observations? *Phys. Rev.*, D91(12):123515, 2015.

[194] Pavel Motloch and Wayne Hu. Tensions between direct measurements of the lens power spectrum from Planck data. *Phys. Rev.*, D97(10):103536, 2018.

[195] Chung-Pei Ma and Edmund Bertschinger. Cosmological perturbation theory in the synchronous and conformal Newtonian gauges. *Astrophys. J.*, 455:7–25, 1995.

[196] C.-P. Ma and E. Bertschinger. Cosmological Perturbation Theory in the Synchronous and Conformal Newtonian Gauges. , 455:7, December 1995.

[197] Personal communication with the MGCAMB authors.